Christoph BIRKL, BSc

Verification of Brown Adipose Tissue Using MRI

Master thesis

Institute of Medical Engineering
Graz University of Technology
Kronesgasse 5, A - 8010 Graz
Head: Univ.-Prof. Dipl.-Ing. Dr.techn. Rudolf Stollberger

Supervisor: Dipl.-Ing. Clemens Diwoky
Supervisor: Univ.-Prof. Dipl.-Ing. Dr.techn. Rudolf Stollberger

Evaluator: Univ.-Prof. Dipl.-Ing. Dr.techn. Rudolf Stollberger

Graz, January 2012

STATUTORY DECLARATION

I declare that I have authored this theseis independently, that I have not used other than the declared sources / resources, and that I have explicitly marked all material which has been quoted either literally or by content from the used sources.

....

date (signature)

Nachweis von braunem Fett mittels MR

Braunes und weißes Fett spielen eine wichtige Rolle im Metabolisums bei Menschen und bei Tieren. Die Menge an braunem Fett im Körper steht im Zusammenhang mit Erkrankungen wie Übergewicht und Typ 2 Diabetes. Das Ziel dieser Arbeit war es, die Einsetzbarkeit einer MR basierten Methode zur Trennung von braunem und weißem Fett zu überprüfen. Dazu wurde ein Arbeitsablauf entwickelt und eine Software für die Bildauswertung programmiert. Für die durchgeführten Experimente wurden Phantome, Menschen und Tiere verwendet. Zur Unterscheidung von braunem und weißem Fett wird zuerst eine Wasser-Fett Trennung durchgeführt und anschließend anhand der Fatfraction das Fett diferenziert. Die Wasser-Fett Trennung wurde mit einem Iterative Decomposition with Echo Asymmetry and Least squares estimation (IDEAL) Algorithmus realisiert. Das meiste braune Fett wurde bei jungen Mäusen im Nackenbereich gefunden. Diese Arbeit zeit dass eine MR basierte Methode verwendet werden kann um Fettgewebe zu trennen und liefert Ideen für Verbesserungsansätze dieser Methode.

Schlüsselwörter: Braunes Fett, Weißes Fett, IDEAL Algorithmus, Wasser Fett Trennung, MR Bildgebung

Verification of Brown Adipose Tissue using MRI

Brown and white adipose tissue plays a significant role in the human and rodent metabolism. The amount of active brown adipose tissue is linked with diseases like obesity or type 2 diabetes. The goal of this project was to evaluate the feasibility of a Magnetic Resonance Imaging (MRI) based method to separate brown and white adipose tissue. To reach this goal a work flow for the image acquisition and an evaluation software tool were developed. The experimental set-up included studies with phantoms, animal and human tissue. To separate the adipose tissue a fat fraction image is required. To calculate the fat fraction a separate water and fat image is calculated by using an Iterative Decomposition with Echo Asymmetry and Least squares estimation (IDEAL) algorithm. Comparing the results of different mice the largest BAT depot in the neck was detected in young mice. This project shows the great potential of the used method to separate adipose tissue and provide an idea for future approaches to improve the estimation results.

Key words: Brown Adipose Tissue, White Adipose Tissue, IDEAL algorithm, Water Fat Separation, MR Imaging

To everybody who has supported me during my studies.

Contents

Abbreviations

BAT - Brown Adipose Tissue
BMI - Body Mass Index
CSI - Chemical Shift Imaging
CT - Computed Tomography
EPI - Echo Planar Imaging
FoV - Field of View
FSE - Fast Spin Echo
GRE - Gradient Echo
GUI - Graphical User Interface
IDEAL - Iterative Decomposition with Echo Asymmetry and Least squares estimation
MR - Magnetic Resonance
MRI - Magnetic Resonance Imaging
NMR - Nuclear Magnetic Resonance
PD - Proton Density
PET-CT - Positron Emission Tomography and Computed Tomography
RF - Radio Frequency
ROI - Region Of Interest
SNR - Signal to Noise Ratio
STIR - Short TI inversion Recovery
TE - Echo Time
TI - Inversion Time
TR - Repetition Time
WAT - White Adipose Tissue

1. Introduction, Motivation and Background

This report addresses a project to improve the separation of brown adipose tissue (BAT) and white adipose tissue (WAT) by using Magnetic Resonance Imaging (MRI). The focus of this project is to combine an existing method with a new approach and develop a feasible evaluation tool. The essential method to separate BAT and WAT is based on an Iterative Decomposition with Echo Asymmetry and Least squares estimation (IDEAL) algorithm for water and fat separation. This algorithm was modified and combined with the calculation of the water- and fat fraction. To provide a more accurate BAT and WAT detection, a combination of the results from the IDEAl algorithm with images of different short TI inversion recovery (STIR) sequences was evaluated. Images of simple water-oil phantoms, mice and humans were evaluated using the IDEAL algorithm. This project should finally lead to a software tool which can be used by research groups as a new standard imaging method to evaluate adipose tissue.

Obesity is the result of the imbalance between energy intake and expenditure in the body. During evolution the importance of storing energy over long fasting periods is decreasing. Today the availability of cheep food and a reduced physical activity lead to a rising number of obese people. According to the obesity report of the World Health Organization more than 1,5 billion adults were overweighted and more than 300 million people were obese. [1]
The works of Cypess et al. [2], Cinti [3] and Van Marken Lichtenbelt et al. [4] showed the importance of the white and brown adipose tissue in the metabolism. The function of the white adipose tissue is to store energy compared to the brown adipose tissue which plays a significant role in the energy expenditure by generating heat in rodents and human infants. The amount and activation state of BAT differs between rodents and humans and depends on the age. Over a long time it was supposed that BAT plays only a role in human infants. The work of Cypess et al. [2] showed that also adult humans can possess active BAT. Cinti [3] showed in his work that the transdifferentiation between BAT and WAT could play a significant role in future therapy of obesity.
These facts lead to a significant interest in the field of adipose tissue research and recently to a rising interest in brown adipose tissue. To evaluate the amount of adipose tissue dif-

ferent imaging methods can be used. The current gold standard in human research is the Positron emission tomography and computed tomography (PET-CT). The disadvantage of PET-CT are high costs, the usage of x-rays and the limitation that only active BAT can be detected. Novel works of Hu et al. [5, 6] showed the potential of using MRI to detect BAT (active and inactive) and WAT in rodents and humans.

This reported approach is based on the different MR properties of brown and white adipose tissue. Brown adipose tissue has a stronger water signal compared to the white adipose tissue which lead to a different fat fraction for BAT and WAT. Using the fat fraction and spectral informations BAT and WAT can be separated by using MRI. [7]

To calculate the fat fraction separate water and fat images are needed. To acquire this water and fat images different water-fat separation methods can be used. [8, 9] Conventional fat saturation methods need a relatively homogeneous B_0 field to generate correct images. For this reason chemical shift based water-fat separation methods have seen a recent increase in use. This methods are also commonly known as Dixon water-fat separation methods.
In this project magnitude and phase images were acquired using a gradient echo sequence (GRE) at different echo times (TE). The optimal sequence settings were based on the work of Reeder et al. [10]. To calculate the water and fat images a Iterative Decomposition with Echo Asymmetry and Least squares estimation (IDEAL) algorithm described by Reeder et al. [11] was used. Over the last decade a lot of different IDEAL based algorithms were described mainly by Reeder et al. [11, 12, 13, 10] Using the results of the IDEAL algorithm the fat fraction can be calculated and used for the adipose tissue evaluation.
A fat fraction of more than 90% is typical for WAT compared with the wider range of BAT between $40 - 80\%$. Using this fat fraction images combined with the knowledge of the adipose tissue depots BAT and WAT can be separated. This project should summarize the state of the art of BAT-WAT separation by using MRI and point out the importance of the method described by Reeder et al. [11]. The first experimental step was to develop a work flow for the verification of this method with images acquired using simple water-oil phantoms, mice and test persons. The usage of phantoms, mice and human images should show the universal usability of the IDEAL algorithm to separate fat and water. The results of the algorithm by using different parameter settings were compared to optimize the settings. For the image evaluation a MATLAB software tool using a graphical user interface (GUI) was developed. Using this tool the result images can be directly displayed and colored with different colormaps for a better visualization of the tissue differences.
The next step was the modification of the existing method using a combination of IDEAL algorithm results with images acquired by using a STIR sequence at two different inversion

(a) Water image. (b) Fat image. (c) Fat fraction image.

Figure 1.1.: Calculated water, fat and fat fraction image. Experimental results of a 2 week old mouse.

times. This extended method should lead to better results in preclinical imaging. The challenge in preclinical imaging is to acquire images with a good SNR behaviour. This requires a good knowledge in the field of sequence optimization and a special equipment eg. coils for small animals. The usability of images acquired at 1,5 T was proven with images of a human knee.

This project showed that a BAT-WAT separation method based on MRI is a feasible method compared with PET-CT. The first experimental work with simple phantoms showed that a feasible water fat separation by using the IDEAL algorithm is possible. The preclinical experiments with different mice showed the feasibility to detect BAT depots in the body. The largest known BAT depot, located in the neck was detected with the used method and shown in figure 4.34. The results of the human experiments showed the usability of the algorithm at different B_0 field strengths. This first experimental work of this project showed positive results that can be used as motivation for further works.
A possible direction for the further research would be to verify the method using images of human infants as shown by Hu et al. [6]. Based on positive results at human infants the method could be extended to exam adult humans. A method based on MRI which could deliver unequivocal BAT-WAT separation results in adult humans would be a great improvement. This would make it a lot easier to design studies with a lager group of test persons to identify the presence of BAT in adult humans.

2. Theory and State of the Art

This chapter provides an introduction to the field of adipose tissue research and describes the difference between the brown and white adipose tissue and their functions in the body. Beside the biological fundamentals the technical state of the art in MRI based water-fat separation methods and different methods to detect BAT are described. This project is focused on the technical aspects of BAT-WAT separation.

2.1. Adipose Tissue

There are two different types of adipose tissue present in humans and mammals. This are the brown adipose tissue (BAT) and the white adipose tissue (WAT) which have different functions and properties. Both types of adipocytes develop out of mesenchymal or mesodermal stem cells via common preadipocytes. This common preadipocytes can differ into white and brown preadipocytes. Out of these preadipocytes the white and brown adipose tissue is formed. The WAT can be separated into subcutaneous and visceral white fat. The differentiation pathway is shown in figure 2.1. Not all stages of the differentiation process are completely defined right now. [14]

A new found aspect of the adipose tissue is the possibility of transdifferentiation between BAT and WAT, which is possible in both ways. BAT to WAT transdifferentiation is needed in the chase of a diet or lack of enegry. On the other hand, WAT to BAT transdifferentiation is needed in chase of a chronic cold exposure and decreasing body temperature. This transdifferentiation is from great interest because there is a strong relation between obesity and the amount of BAT. [3]

The adipocytes are linked together and form the adipose organ, the depot of the fat. The locations of these adipose organs differ in humans and mammals and depend on several parameters like the age. The fat distribution changes with the age also in the case of a steady body weight and BMI.

The genetics plays also a very important role in fat storage and distribution. The probability to develop obesity and type 2 diabetes is strongly linked with the genetics. [14] The different distribution, location and function of WAT and BAT in rodents 2.6 and humans 2.5 are described in the following chapters.

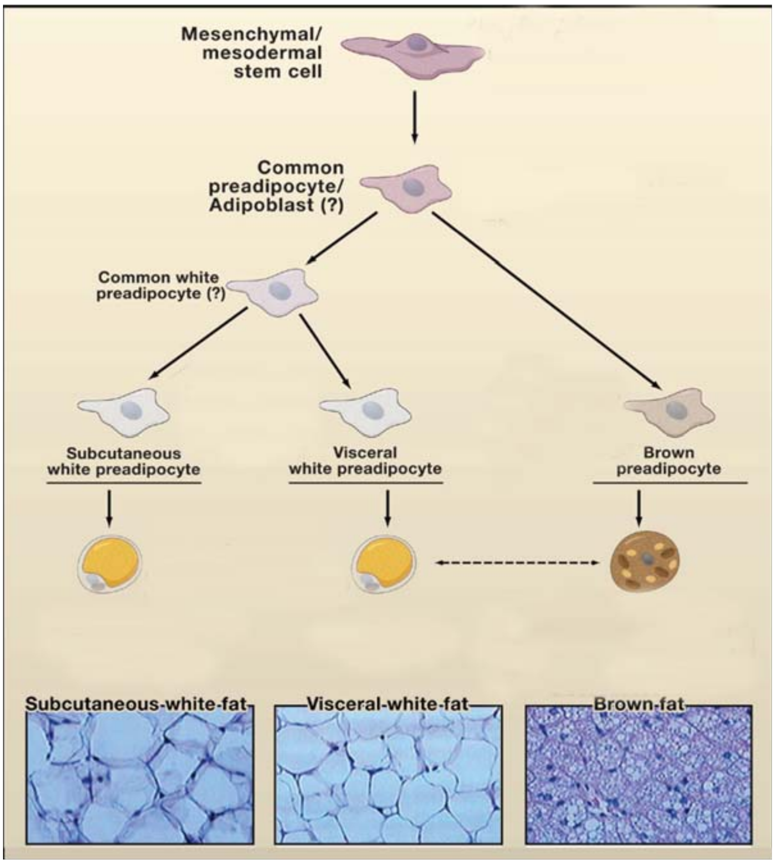

Figure 2.1.: Differentiation pathway of white and brown adipocytes. WAT and BAT arise from mesenchymal or mesodermal stem cells. Modified form [14].

2.1.1. What is White Adipose Tissue (WAT)?

The white adipose tissue is the energy storage tissue of the body. The most important property of the white adipocytes is the ability of accumulation and release of fatty acids. These fatty acids are stored in the cytoplasm as triglycerides. The white fat cell exists of a large single lipid droplet and a small amount of cytoplasm which is surrounded by a non-membranous electron-dense barrier. [3]

In figure 2.2 the morphological difference of the white and brown adipose tissue is shown. The large lipid droplets of the WAT can be clearly seen. About 20 - 25% of the human bodyweight is caused by the WAT. This tissue plays an important role in the whole metabolism of the body. In the case of a genetic mutation or a fat rich diet the white fat tissue expands in volume. This can lead in extreme situations to obesity which can lead to type 2 diabetes or cardiovascular diseases.

In the work of Henry et al. [15] endocrine functions of WAT are described as a important function beside energy storage. White adipose tissue produces different cytokines e.g. leptin or adiponectin. Leptin is important for the regulation of the body weight by suppressing the food intake and increasing the thermogenesis by acting in the brain. Adiponectin

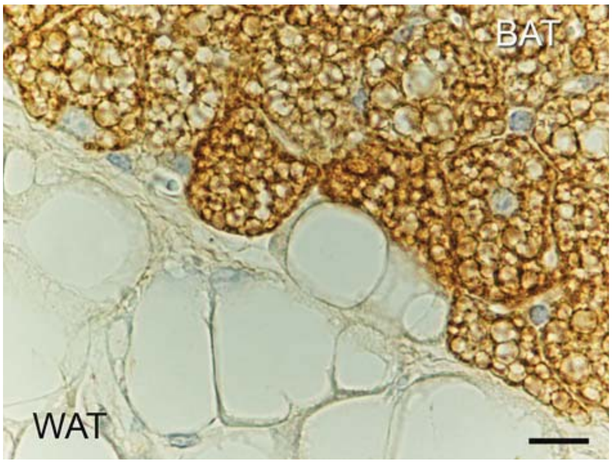

Figure 2.2.: Light microscopy image of the boarder tissue section between BAT and WAT of a mouse adipose organ. [3]

plays a role in protecting against insulin resistance, type 2 diabetes or atherosclerosis and promotes weight loss and the fatty acid oxidation. [15]

2.1.2. What is Brown Adipose Tissue (BAT)?

The brown adipose tissue plays a significant role in the thermogenic regulation process by producing heat in the body. The BAT can be found in an active- or inactive thermogenic state. [16]
This is very important in rodents and human infants because they do not have a possibility to shiver. BAT contains small droplets of fat and a high number of mitochondria. The mitochondria contain a high amount of laminar cristae which contain a tissue specific uncoupling protein (UCP1). The high amount of iron ions in the mitochondria and the rich vascularity are the reason for the brown color. So it is possible to differ BAT and WAT samples by the naked eye e.g. in samples from a cryosection. If the BAT is activated e.g. through cold exposure this UCP1 reduces the electrochemical gradient between the mitochondria and the surrounding compartment. This reduction lead to a rising fatty acid beta oxidation and as result to heat. The rising activity of BAT after cold exposure can be seen in figure 2.3. [2, 3, 17]

A lot of different research groups are focused on BAT and its role in the metabolism. New findings pointed out that there is a connection between BAT and obesity or diabetes type 2. The work of Van Marken Lichtenbelt et al. [4] showed a cold induced uptake of the BAT activity which was showed using PET-CT. Detailed analyses showed a negative correlation between the body mass index (BMI) and the BAT activity. The amount of BAT is also negatively correlated with the development of obesity and diabetes. [2, 3, 17]

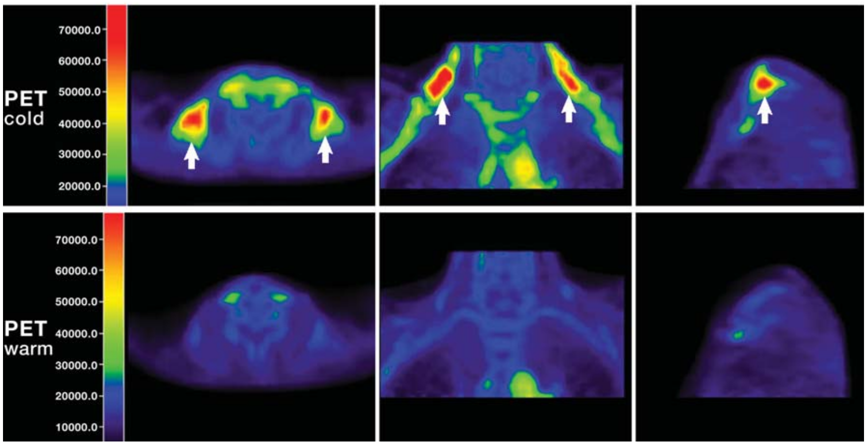

Figure 2.3.: PET-CT images of a healthy adult acquired after cold exposure (18°) and at room temperature. A significant rising BAT activity can be seen. Modified from [17]

2.2. Chemical Shift

The chemical environment of the protons lead to a different electronic shielding and to a different local magnetic field, as described in equation (2.2). This small differences are the reason for the different proton resonance frequencies and is called chemical shift. This chemical shift is proportional to the B_0 field and leads to a greater shift between the spectral peaks at higher field strengths. The chemical shift is measured in parts per million (ppm) to be independent of the B_0 field.
To calculate the resonance frequency of water protons equation (2.1) is used where γ is the gyromangnetic ratio ($\gamma = 42,5\,\frac{MHz}{T}$).

$$\omega_0 = \gamma B_0 \tag{2.1}$$

$$B_{nuc}(x) \propto B_{mac}(x) - \sigma B_0 \tag{2.2}$$

The chemical shift between water and the main fat peak is $\Delta\omega \approx -420\,Hz$ at 3 T and $\Delta\omega \approx -210\,Hz$ at 1,5 T. To calculate the chemical shift in ppm equation (2.3) is used and leads to $\rho_{ppm} = 3.5\,ppm$.

$$\rho_{ppm} = \frac{\Delta\omega}{\omega_0} \tag{2.3}$$

The resonance frequency of water and also the chemical shift between water and fat depend on the temperature of the imaged object (e.g. tissue or phantom). With decreasing temperature the chemical shift is increasing. [9]

2.3. Water and Fat Separation Methods

A lot of different methods based on MRI to separate or suppress water and fat are used in clinical diagnostics. An accurate water or fat suppression is needed to avoid false interpretation of structures in the images for different diagnostic issues.Usually a strong fat signal is unwanted because it can obscure underlying pathological structures such as edema, inflammations or tumors. [9] On the other side a strong water signal is unwanted when adipose tissue is in the focus of interest.
In this chapter the most important methods and specially the method used in this project are described. It is important to choose the right method and parameters for the given medical question. The following chapter is based on [9] and [8].

2.3.1. Chemically Selective Fat Suppression Pulses (FAT-SAT)

This is a relatively fast method to suppress unwanted signals from a special species e.g. fat. A RF impulse centred at the main frequency of the unwanted fat species is used to suppress the longitudinal magnetization. As RF pulse a sinc function is used which is equivalent to a rectangle in the fourier domain. The RF pulse is followed by a crusher gradient to spoil the transverse magnetization of the fat. After this fat saturation a standard imaging sequence can be used. The longitudinal magnetization of the fat has no time to recover and so there is no signal from the fat tissue. To get a good result, the B0 and B1 field should be homogeneous over the FoV. The main disadvantage of this method is the sensitivity to B0 field inhomogeneities. The B0 field inhomogeneity leads

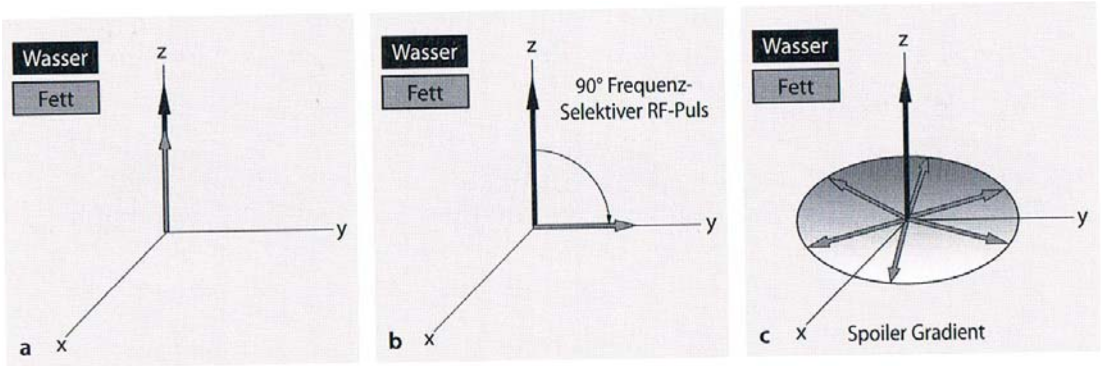

Figure 2.4.: (a,b) A 90° frequency selective RF pulse tips the magnetization of the fat into the transversal plane. (c) The dephasing of the fat spins is accelerated by the crusher (spoiler) gradient. [8]

to fat frequency shift and to a inaccurate fat suppressor. The worst case would be the suppression of the water signal instead of the fat signal. Also a relative accurate 90° pulse and coils with uniform RF field are required for this method. The FAT-SAT method works better at higher field strengths because the shift between the water and fat peak is greater.

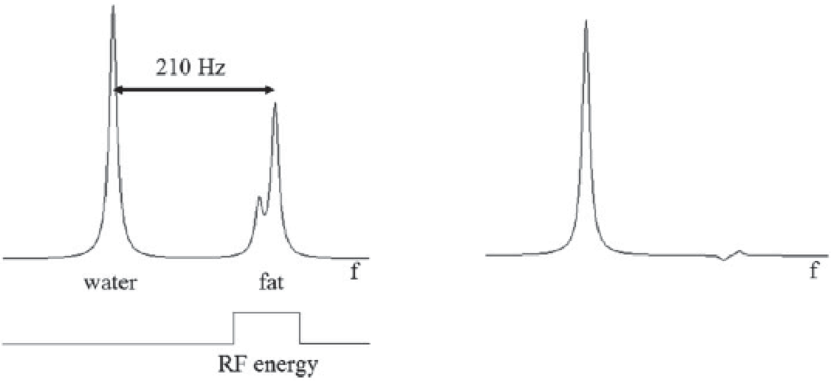

(a) Before fat-sat.

(b) After fat-sat.

Figure 2.5.: Schematic of the fat saturation method at 1,5 T using a rectangular fat-sat pulse. [9]

2.3.2. Spatial-Spectral Pulses

This method suppresses fat by a selective excitation of the water signal using a spatial spectral pulse. The concept of this method is to add a spectral dimension to the k-space. The pulse excites simultaneous a slice and a spectral band e.g. the water band.
To achieve this, α pulse with $5 - 10°$ are applied with a separation time between this pulses. This separation time T is selected in a way (see equation (2.4)) that the fat signal precesses 180° relative to the water signal.

$$T = \frac{1}{2\Delta f} \tag{2.4}$$

The second α pulse flips the fat back in the z-plane, excites the water signal and leads to a signal with no fat component (see figure 2.6). This method is commonly used in combination with EPI sequences and very effective. It is also possible to combine it with other sequences like SPGRE or FSE. A advantage is the insensitivity to B1 inhomogeneities. This method works best at higher field strengths and with shorter RF pulses. The disadvantages of this method are the sensitivity to B0 inhomogeneities and the long pulse time.
This fat suppression method is used at cartilage imaging where a uniform fat suppression and a high spatial resolution is needed.

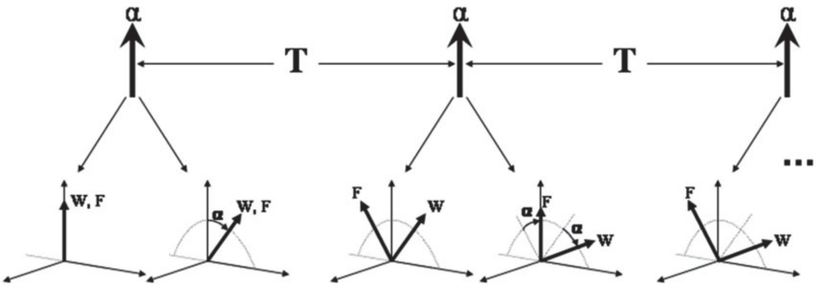

Figure 2.6.: Schematic of the spatial-spectral-pulses method. The α pulses are separated by a time T to create a phase shift of 180° between the water and the fat component. [9]

2.3.3. Short Inversion Time (TI) Inversion Recovery (STIR) Imaging

The STIR sequence is based on the conventional inversion recovery (IR) sequence and combined with a inversion time (TI). This inversion time is the pause between the 180° and the 90° pulse. The TI time is chosen in a way that the longitudinal magnetization fat signal (short T1 time) is zero at the time of the 90° pulse (see figure 2.7). The advantage of STIR is the insensitivity to B0 and B1 inhomogeneities and the good uniform fat suppression over a large FoV. The disadvantages are the low SNR efficiency and the suppression of other species with short T1 time. This fat suppression works only with PD and T2 weighted images. This method is widely used over all filed strengths and commonly combined with SE based sequences.

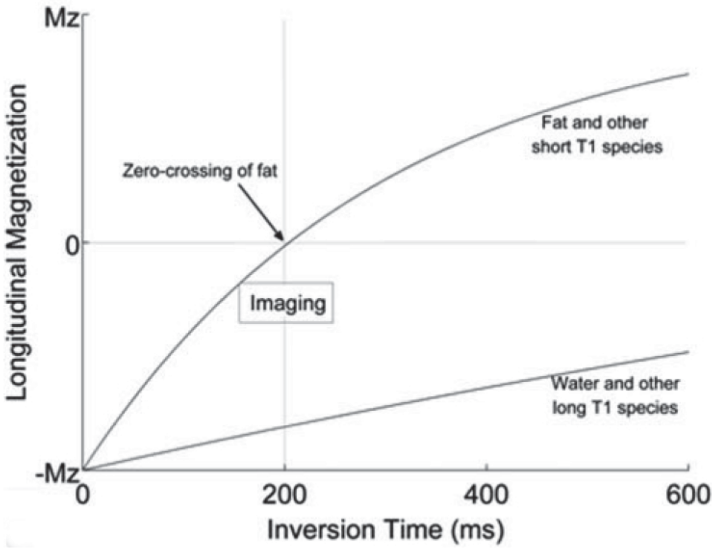

Figure 2.7.: Longitudinal magnetization of water and fat in relation to the inversion time (TI). The zero-crossing of fat is the optimal inversion time for the fat suppression. Modified form [9].

In combination with other inversion times this method can be used to suppress other tissues with specific T1 times.

2.3.4. Chemical Shift (DIXON) based Water-Fat Separation Methods

The chemical shift based water-fat separation methods are commonly known as DIXON based methods. The DIXON methods are based on the phase shift between the water and fat resonance frequency. The phase informations are calculated out of images, acquired at different echo times. The result of this methods are a separate water- and fat image. The first approach by Dixon [18] acquired a in-phase and a out-of phase image. The concept of the images at different echo times is shown in figure 2.8. At the in-phase image the signal from water and fat leads to a stronger signal than in the out-of-phase image (see figure 2.9). Using the in- and out-of-phase information a water only (equation (2.5)) and fat only (equation (2.6)) image can be calculated.

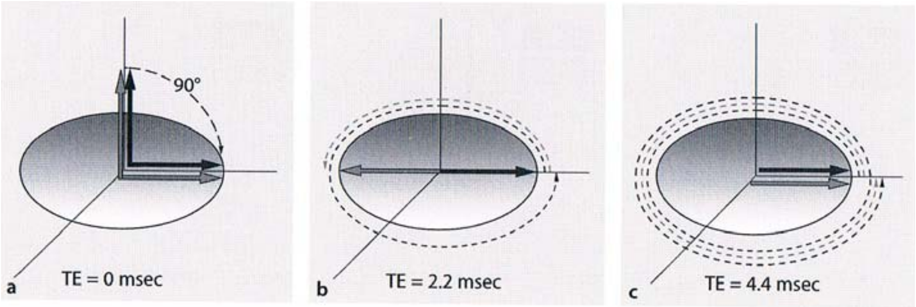

Figure 2.8.: Phase difference between fat (grey arrow) and water (black arrow) in relation to the echo time (TE) at 1,5 T. (a) At TE = 0 ms. (b) The out-of-phase at TE = 2,2 ms. (c) The in-phase at TE = 4,4 ms. [8]

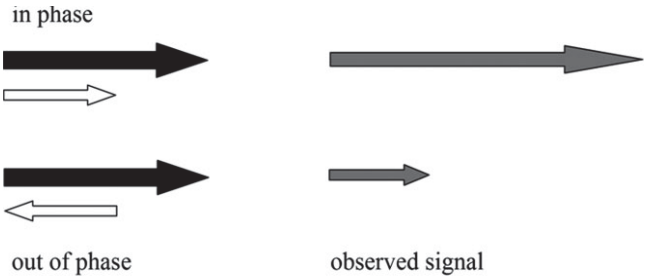

Figure 2.9.: In-phase ($S_{in} = W + F$) and out-of-phase ($S_{out} = W - F$) signal diagram. [10]

$$W = \frac{S_{in} + S_{out}}{2} \tag{2.5}$$

$$F = \frac{S_{in} - S_{out}}{2} \tag{2.6}$$

This so called two-point method has the disadvantage of a strong sensitivity to B0 inhomogeneities this leads to a water-fat swapping. The water-fat swapping occurs because a voxel with fat only and a voxel with off-resonant water provide the same signal.

Golver and Schneider developed the three-point method based on the DIXON two-point method. With the third image acquired at a different echo time a B0 field map image of the inhomogeneities can be calculated. Using this field map and a unwrapping algorithm the water-fat swapping can be eliminated. The echo times are chosen in a way that the phase shift of water and fat are at 0, $+\pi$ and $-\pi$.
The great advantage of the three-point method is the compensation of the B0 inhomogeneities and the robust water-fat separation also in areas of high susceptibility. This method is SNR-effective if the echo times are chosen correct. The disadvantage of the DIXON based methods is the long scan time. Every additional image provides more information but also leads to a longer scan time.

The DIXON method can be modified to a multipoint water-fat separation method. This method is called, iterative decomposition of water and fat with echo asymmetry and least squares estimation (IDEAL). This method can be use with arbitrary echo times but only leads to a maximum SNR with the correct set of TEs. Using three echoes the second echo should be at the quadrature phase between water and fat. The first echo is set to $-\frac{2\pi}{3}$ and the third echo to $+\frac{2\pi}{3}$ relative to the center echo. The right parameters for the IDEAL method are discussed in different papers over the last years. [11, 12, 10, 13]
With the IDEAL method it is possible to separate more than two species, if they have a different resonance peak frequency (e.g. water. fat and silikon). [11] It is also possible to model the fat with more than one frequency peak. [12] The IDEAL algorithm is compatible with different sequences like FSE, GRE, SSFP and different weighting (e.g. T_1, T_2 or PD). The optimal echo times and parameters to maximize the SNR differ for each sequence. In the medical practice this method is commonly used for regions where other fat suppression methods fail (e.g. in the neck).

In this project a three-point IDEAL algorithm based on [11] is used. The fat spectrum was modelled with the main frequency at -431 Hz according to the 3 T MRI system. For the image acquisitions different GRE sequences were used with optimized parameters. [10] Detailed informations about the algorithm and sequences are in chapter Methods.

2.4. BAT-WAT Separation Methods

To detect BAT or separate BAT and WAT different methods are used today. The most important methods are PET-CT, MRI and SVS. In this chapter the methods and there advantages or disadvantages are described.

2.4.1. BAT Detection using MRI

Hamilton et al. [7] summarized in his work the MR properties of BAT and WAT. Beside the spectral difference of BAT and WAT a different inversion recovery behavior in the water peak was measured. Using the results of a chemical shift based water-fat separation method (e.g. IDEAL) it is possible to quantify the fat tissue. For this quantification the fat fraction (equation (2.7)) must be calculated using the water and fat image. The main question of this thesis, the detection of BAT, is based on this calculated fat fraction. Using the described IDEAL algorithm it is possible to separate species with different spectral peaks. The problem of the separation of BAT and WAT is, that both tissues have the same spectral frequency peaks. The main difference between BAT and WAT is the amount of water. This can be clearly seen in the comparison of the spectrum (see figure 2.10). With the detailed spectral informations and a multyfrequent IDEAL algorithm it is possible to model the fat with multiple frequencies. Reeder et al. described a multiecho and multyfrequency IDEAL algorithm with different spectrum calibrations. [12] For this method a spectrum calibration is important to model the fat. The two described methods for this calibration are the precalibration using MR spectroscopy and the spectrum self calibration. For each additional modelled frequency peak an additional image is required. [12] The additional images and the higher computation time result in a longer examination time which is not always accepted.

$$fatfraction = \frac{fatimage}{fatimage + waterimage} \tag{2.7}$$

At higher filed strengths it is possible to determine BAT using chemical shift imaging (CSI) methods. Lunati et al. [16] and Sbarbati et al. [19] used a CSI method at a imager spectrometer with 4,7 T to generate a water-only and a fat-only image in their works. To determine BAT the above described fat fraction is calculated and evaluated. Proton NMR spectroscopy can be used to evaluate excised fat tissue. Using this method it is possible to determine the lipid composition of the adipose tissue in vivo. [20]

A great advantage of MRI based methods is that active- and inactive BAT can be detected because the method separates the tissues based on the morphological differences.

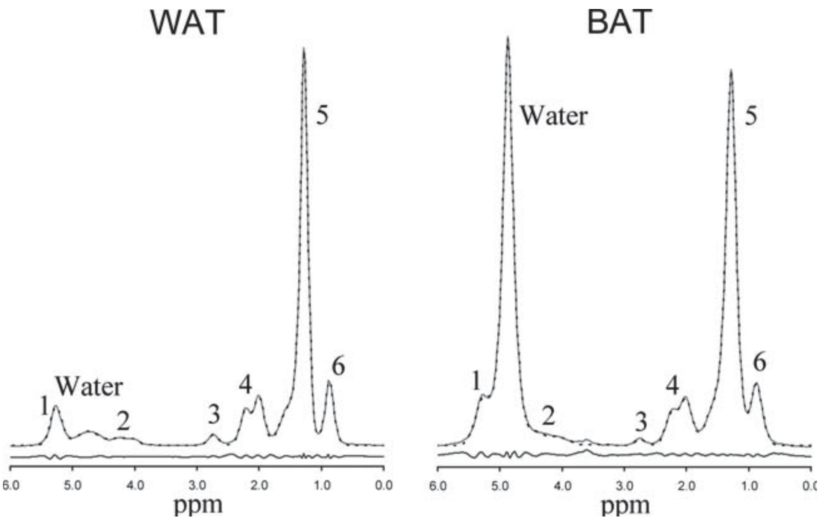

Figure 2.10.: Spectrum from a WAT and BAT sample. [9]

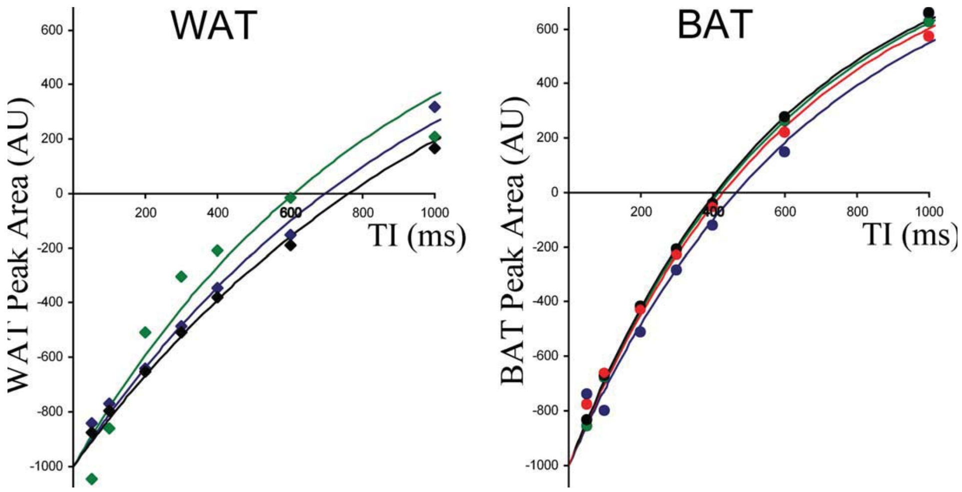

Figure 2.11.: Different inversion recovery behavior of the water peak between BAT and WAT. [7]

2.4.2. Positron Emission Tomography and Computed Tomography (PET-CT)

Positron-emission tomography and computed tomography is a standard method to image functional processes in the human body. This method is used to detect active BAT in the human body with 18F-fluorodeoxyglucose (18F-FDG) as tracer substance. This positron tracer is injected into the body an interacts after a short distance with electrons. This process is called annihilation. During the annihilition the positron and electron were destroyed and two gamma photons moving in opposite directions were created (see figure 2.12). The distance of the proton between the creation and the interaction depents on the positron energy an on the coincidence of hitting a electron. The maximum distance for 18F is about 2 mm. To detect the gamma photons a coincidence detector is used.

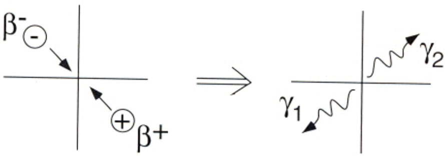

Figure 2.12.: Annihlition of a positron and an electron. [21]

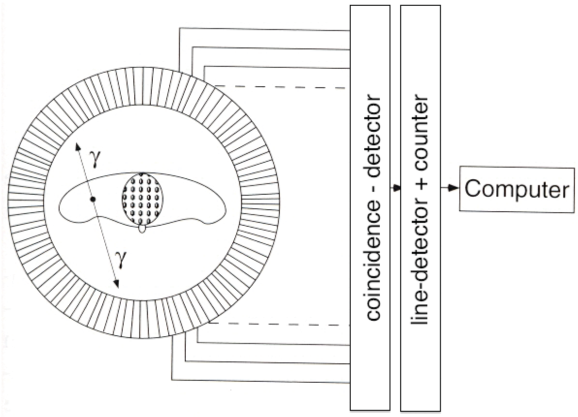

Figure 2.13.: Concept of an PET system. Modified from [21].

This detector counts only the gamma photons which reach the detector at the same time (including a time slot of 10-20 ns).
To detect BAT by using PET-CT the maximum uptake value of 18F-FDG is measured in areas where fat was detected by using CT. The uptake values are the activity per millimeter within a ROI divided by the injected dose per gram of body weight. [2]

2.5. Human Research

In different human studies [2, 4] BAT was detected by using 18F-flurodeoxyglucose positron-emission tomography and computed tomography (PET-CT). A huge disadvantage of this method is the use of x-ray's and nuclear tracers and the fact that only activated BAT is detectable. It is difficult to argue the need of a PET-CT study for a large group of human volunteers. A second disadvantage are the high costs and technical requirements for a PET-CT examination.
For a long time it was supposed that there is no BAT in adult human and that BAT does not affect the metabolism. In the study of Cypess et al. [2], 3640 PET-CT scans from 1972 patients were analysed to search for BAT depots in human adults. Functionally active BAT was found in 76 of 1013 women (7,5%) and 30 of 959 men (3,1%). The most important depot of BAT in adult humans is the cervical-supraclavicular depot in a distinct fascial plane in the ventral neck. Further more there is BAT superficial and lateral to the sternocleidomastoid muscles. All known BAT and WAT depots in infant and adult humans are shown in figure 2.14. The study of Lichtenbelt et al. [4] showed that there is a

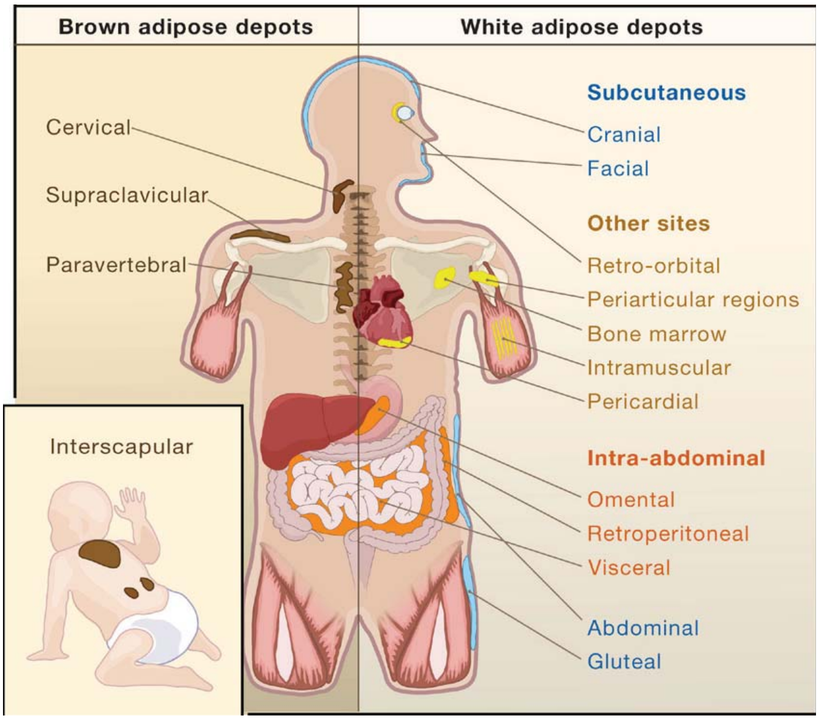

Figure 2.14.: Locations of the BAT and WAT depots in infant and adult humans. Modified from [14].

significant connection between a cold exposure and the activity of the BAT. In this context the activity of the BAT was significant lower in people with obesity. The amount of BAT is inversely correlated with the body-mass-index (BMI) and the percentage of body fat. [4]

The female:male ratio of active BAT in adult humans is 2:1 and also the mass of the BAT depots is greater in women. The amount of the detected BAT inversely correlates with the age, the outdoor temperature and the use of beta-blocker at the time of the scan. [2]

In a new study of Hu et al. [6] a 3 month old infant human was scanned with MRI and CT to separate BAT and WAT from the surrounding tissue. The patient 3 month female infant died after alveolar capillary dysplasia. The advantage of MRI or CT is that the separation is based on the cellular differences of the adipose tissue. In this new work a amount of about 17 ml supraclavicular BAT could be detected with both methods (MRI and CT). In figure 2.16 the BAT depot near the neck (marked with arrows) and the differences between the MRI and CT contrast are shown.

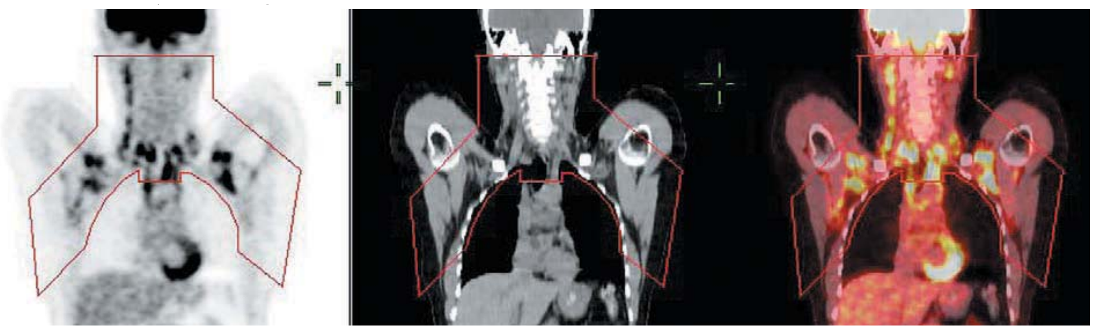

Figure 2.15.: Result of a PET-CT (PET- CT- and combined image) detecting BAT in the human body. [2]

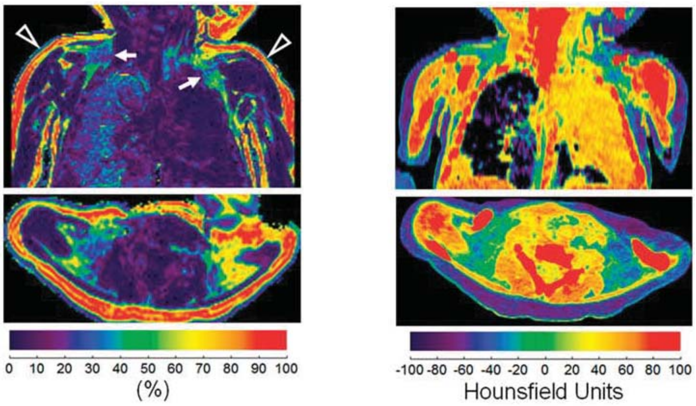

(a) MRI

(b) CT

Figure 2.16.: MRI fatfraction images and CT image of a 3 month old human infant. Modified form [6].

2.6. Preclinical Research

In rodents, BAT is present through the whole life and plays a role in the thermoregulation. The anterior interscapular BAT is the main depot in mice and rats. In figure 2.17 A, the locations of the adipose tissue is shown. The subcutaneous trunk depots consiste of BAT and WAT. Cinti S [3] showed in his study that a continuous cold exposure indicates a trasdifferentiation of WAT to BAT. The increase of BAT can be seen in 2.17 C. The mouse was kept at a constant temperature of 6°C over 10 days.

To evaluate the BAT in rodents, chemical shift imaging, single-voxel-spectroscopy (SVS) or MR imaging can be used.
Chemical shift imaging at 4.7 T, generate through different scans water and fat images and calculate fat maps. offset between water and fat at 4.7 T is about 700 Hz. A problem in animal studies is the possibility to image living objects. There is a significant difference in the fat fraction of BAT depots between living and dead rats. [16] To detect small depots of BAT in rats chemical shift imaging at 4.7 T is used. [19]

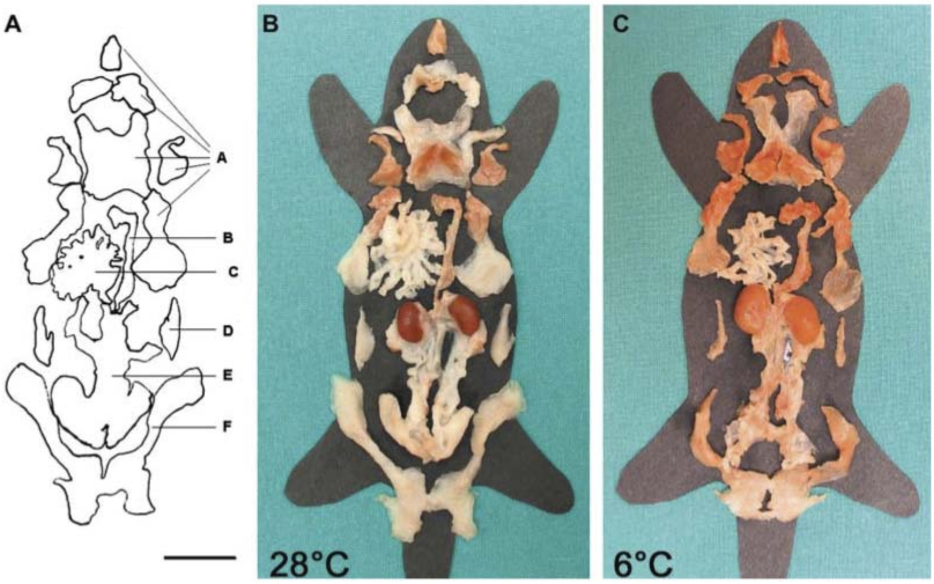

Figure 2.17.: Adipose tissue anatomy of a mouse after different temperature exposure over 10 days. (A and F) subcutaneous and visceral (B) mediastinal, (C) mesenteric, (D) retroperitoneal and (E) abdomino-pelvic depots. Bar = 1 cm. [3]

A relatively new approach to separate BAT and WAT in rodents is based on the calculation of the fat fraction using MRI images. A first approach to use this technique in mice was shown by Hu et al. [5] in 2010. In this study excised BAT and WAT samples and also whole mice were imaged. Fat and water images were calculated using an IDEAL algorithm. The fat fraction was used to separate white and brown adipose tissue.

3. Description of the Experimental Set-Up and Work Environment

3.1. Magnet Resonance Imaging

In this project a method based on MRI was used to separate water and fat. Using this water and fat images BAT and WAT was separated in a second step. Two different MR systems were used for the phantom, preclinical and human examinations. All preclinical and phantom experiments were measured with the 3 T MR system at the Department of Radiology, University Hospital LKH Graz. As second MR system a Siemens 1,5 T system located at the Sportsclinic Arlberg was used for human examinations.

3 T MR System

Table 3.1.: Magnetom Tim Trio system parameter

System Type	Siemens Magnetom Tim Trio whole-body MR
B_0 Fieldstrength	3 T
Bore	60 cm
Maximal Gradient Fieldstrength	38 mT/m

1.5 T MR System

Table 3.2.: Magnetom Essenza system parameter

System Type	Siemens Magnetom Essenza whole-body MR
B_0 Fieldstrength	1,5 T
Bore	70 cm
Maximal Gradient Fieldstrength	30 mT/m

(a) Tim Trio 3 T. (b) Essenza 1,5 T.

Figure 3.1.: The 3 T and 1,5 T Siemens MR systems used in this project.

Experimental Setup, Coils and Phantoms

A $1H$ Transmit / Receive Volume Coil with a inner diameter of 33 mm (see figure 3.2) was used for the phantom and preclinical (mice) experiments. For the preclinical experiments an animal holder for mice was used to position the mice in the coil. During the examination of the mice anaesthesia was performed in accordance to an local steering committee with $1,8\%$ Isofluorane in $1,5\,l/min\ O_2$.
For the phantom studies Falcon Tubes with a volume of 50 ml were used to crate a water-oil phantom. The water ($35\,ml$) was mixed with $17\,\mu l$ gadolinium to reduce the T1 time (and the TR time of the scan) and $15\,ml$ oil (Mazola). For this phantom experiments the same $1H$ Transmit / Receive Volume Coil was used. For the human experiments the standard MRI scan procedure and different coils e.g. knee was used.

Figure 3.2.: 1H Transmit / Receive Volumen Coil for mice and a Falcon Tube used for phantom and preclinical experiments.

3.1.1. Used Sequences

Generally different sequences (e.g. SSFP, FSE or GRE) can be used in combination with a Dixon or IDEAL algorithm. In this project only GRE sequences were used at both MRI systems. The problem with the spin echo sequences on a Siemens MRI system is, that the operator is not allowed to set the required echo times. So it is not possible to set the optimal parameters for the IDEAl algorithm. The only way to use spin echo based sequences on this system is to program a modified sequence by using IDEA. In this project a basic GRE sequence was modified for phantom, preclinical an human imaging. The same sequence was used for all three or more measurements with a different echo time at each sequence. As result we get magnitude and phase images at different echo times (TE). This images and the known chemical shift frequency between water and fat is used as input for the IDEAL algorithm.

To evaluate a second way to separate BAT and WAT two short TI inversion recovery sequences with different inversion times (TI) were used. Hamilton G et al. [7] described a different inversion recovery behaviour of the water component in BAT and WAT. A basic T1 weighted STIR sequence with TR = 2000 ms, TE = 12 ms and TI = 400 ms for BAT and TI = 700 ms for WAT was used. The amount of slices, FoV, slice thickness and the resolution parameters were aligned to the values of the measured GRE sequence.

Optimal Parameters

To get the best results from the algorithm it is important to calculate the optimal echo times and echo spacing time by using following equations. [10] A non optimal phase shift between water and fat reflects in a bad noise performance of the water-fat-decomposition. For a optimal setting the 2^{nd} echo should be acquired in quadrature. Common values for Δf are -420 Hz at 3 T and -210 Hz at 1,5 T. The offset at the Siemens 3 T MRI system located at the University Hospital LKH Graz is -431 Hz. For all calculations this value was used.

$$\Theta = 2\pi\Delta f t \tag{3.1}$$

$$\begin{aligned} 1^{st} echo &: -\pi/6 + \pi k \\ 2^{nd} echo &: \pi/2 + \pi k \\ 3^{rd} echo &: 7\pi/6 + \pi k \end{aligned} \tag{3.2}$$

Using equations (3.2) and (3.1) we can calculate the optimal echo time for the scan protocols. To calculate the echo spacing we can use the equation (3.3) from [11]. Where

N is the number of echos and f_{fw} is the chemical shift between fat and water in Hz. [9]

$$\Delta t = \frac{1}{N \Delta f_{fw}} \tag{3.3}$$

The calculated optimal echo times at 3 T with $\Delta f = -431\,Hz$ are,

$$TE_1 : 4,72\,ms$$
$$TE_2 : 5,54\,ms$$
$$TE_3 : 6,36\,ms.$$

3.2. Water-Fat Separation Algorithm

The Iterative Decomposition with Echo Asymmetry and Least squares estimation (IDEAL) algorithm is a chemical shift based water-fat separation method. The first approach was described by Dixon in 1984 [18], which is the reason why this methods are often called Dixon based water-fat separation methods.

The algorithm, used in this project is based on a water-fat separation algorithm published by Reeder et al. [11] This basic algorithm was modified and combined with optimal echo times for GRE sequences. [10]

3.2.1. Signal Model

The signal from a pixel with multiple species M in the acquired images is described by formula (3.4). The chemical shift Δf_j of each species is given in Hz. The magnitude and phase images are acquired at different echo times (TE) with $t_n(n = 1, ..., N)$.

$$s_n = \left(\sum_{j=1}^{M} \rho_j e^{i2\pi \Delta f_j t_n} \right) e^{i2\pi \psi t_n} \tag{3.4}$$

In the signal equation (3.4), ρ represents the unknown intensity of each species and ψ the local magnetic resonance offset in Hz. For a simple water-fat separation (M = 2) we need M+1 images to determine ρ. This leads to three different echo times (N = 3).

With a given initial guess of the field map ψ_0 the equation (3.4) can be written as

$$\hat{s}_n = s_n e^{-i2\pi \psi_0 t_n} = \sum_{j=1}^{M} \rho_j e^{i2\pi \Delta f_j t_n}. \tag{3.5}$$

The equation 3.5 can be split into real- (ρ_j^R) and imaginary part (ρ_j^I) as shown in equation 3.6.

$$\hat{s}_n = \hat{s}_n^R + i\hat{s}_n^I = \sum_{j=1}^{M}(\rho_j^R c_{jn} - \rho_j^I d_{jn}) + i\sum_{j=1}^{M}(\rho_j^R d_{jn} - \rho_j^I c_{jn}) \tag{3.6}$$

$$c_{jn} = cos(2\pi\Delta f_j t_n) \tag{3.7}$$

$$d_{jn} = sin(2\pi\Delta f_j t_n) \tag{3.8}$$

3.2.2. IDEAL Algorithm

To describe the Iterative Least-Squares Estimation Method we need the signal model from 3.2.1. The least squares estimation minimizes an error term to calculate the best possible estimation using the acquired data. The following steps describe the work flow of a water-fat separation using images of a single coil acquisition. The full set of equations describing the IDEAl algorithm are provided in the appendix A.1
In this section the equations are written in matrix form and provide the special case of a water separation using images acquired at three different echo times.

1. **Estimate the signal from each chemical species using equation (3.9).**

   The initial guess for the field map ψ_0 is zero. To calculate $\hat{\rho}$ the Moore-Penrose pseudoinverse is used.

   $$\hat{\rho} = (A^T A)^{-1} A^T \hat{S} \tag{3.9}$$

   The matrix A for two species (water and fat) is described by formula (3.10). The matrix for N different species is described in the appendix.

   $$A = \begin{bmatrix} c_{11} & -d_{11} & c_{21} & -d_{21} \\ c_{12} & -d_{12} & c_{22} & -d_{22} \\ c_{13} & -d_{13} & c_{23} & -d_{23} \\ d_{11} & c_{11} & d_{21} & c_{21} \\ d_{12} & c_{12} & d_{22} & c_{22} \\ d_{13} & c_{13} & d_{23} & c_{23} \end{bmatrix} \tag{3.10}$$

2. **Calculate the error to the field map $\Delta\psi$ using equation (3.11).**

$$y = \begin{bmatrix} \Delta\psi & \Delta\rho_1^R & \Delta\rho_1^I & \Delta\rho_2^R & \Delta\rho_2^I \end{bmatrix}^T$$

$$y = (B^T B)^{-1} B^T \hat{\hat{S}} \tag{3.11}$$

$$B = \begin{bmatrix} g_{11}^R & c_{11} & -d_{11} & c_{21} & -d_{21} \\ g_{12}^R & c_{12} & -d_{12} & c_{22} & -d_{22} \\ g_{13}^R & c_{13} & -d_{13} & c_{23} & -d_{23} \\ g_{11}^I & d_{11} & c_{11} & d_{21} & c_{21} \\ g_{12}^I & d_{12} & c_{12} & d_{22} & c_{22} \\ g_{13}^I & d_{13} & c_{13} & d_{23} & c_{23} \end{bmatrix} \tag{3.12}$$

For the calculation of the B matrix (3.12) equations (3.7), (3.8), (3.13) and (3.14) are used.

$$g_{jn}^R = 2\pi t_n \sum_{j=1}^{M} (-\hat{\rho}_j^R d_{jn} - \hat{\rho}_j^I c_{jn}) \tag{3.13}$$

$$g_{jn}^I = 2\pi t_n \sum_{j=1}^{M} (\hat{\rho}_j^R c_{jn} - \hat{\rho}_j^I d_{jn}) \tag{3.14}$$

3. **Recalculate the new field map by using equation (3.15) and the calculated field map error.**

$$\psi = \psi_0 + \Delta\psi \tag{3.15}$$

4. **Recalculate $\hat{s}_n$ using equations (3.5), (3.6) and the new estimate of the field map ψ.**

   This is the update step of the IDEAL algorithm.

5. **Repeat steps 2-4 until $\Delta\psi < 1\,Hz$ or the number of iterations is greater than 40.**

In case the algorithm does not converge within 40 iterations a break point is set and the last calculated value is used to calculate the final estimate of the field map.

6. **Filter the final field map ψ with a low pass filter.**

   The final field map estimate is filtered by using a Gaussian low pass filter. The MATLAB low pass filter function was used with a 3x3 filter kernel and $\sigma = 1$.

7. **Recalculate the final estimate of each species (e.g. water and fat) with equation (3.9).**

   Using the final calculated and filtered field map the final water and fat image can be calculated. All additional images (e.g. fat fraction or water fraction) are not a part of the IDEAL algorithm and calculated in a separate function.

The result of the IDEAL algorithm is the least-squares estimation of a water and a fat image. With this informations we can calculate further parameters e.g. the fat fraction or in- and out-of-phase images.
This algorithm can also used to separate more than two species e.g. water, fat and silicon as shown in the work of Reeder et al. [11]. The full set of equations for the used IDEAL algorithm is described in the Appendix.

Multifrequency Algorithm

The above described algorithm can be modified to a multifrequency algorithm as described by Yu et al. [12]. This approach uses more than one frequency peak f_p to model the fat. Each fat peak is now weighted with a relative amplitude α_p such that $\sum_{p=1}^{P} \alpha_p = 1$. The signal model for the multipoint approach is described in equation (3.16). The result of this algorithm is a water image and a separate fat image for each modelled fat frequency peak.

$$s(t) = (\rho_w + \rho_f \sum_{p=1}^{P} \alpha_p \cdot e^{i2\pi f_p t}) \cdot e^{i2\pi\psi t} \tag{3.16}$$

For the 6-point spectrum self-calibration algorithm as described in the work of Vu et al. [12] an additional conventional IDEAL algorithm is needed to create a fat mask image. This calculations and the additional images for a multifrequency approach lead to a significant higher acquisition time.

3.3. Workflow and MATLAB Water-Fat Separation Tool

For the evaluation of the MR images a MATLAB tool (BAT-WAT IDEAL) was programmed, using the IDEAL algorithm described in 3.2.2. This tool is using magnitude and phase images acquired at different echo times (TE) to calculate separate water- and fat images and am estimated B_0 field map. Using the water and fat image additional image e.g. water and fat fraction can be calculated in order to separate BAT and WAT. All calculated calculated images were described in section 3.3.2.

In this chapter the developed work flow to acquire images by using the 3 T MR system and the evaluation of the images by using the BAT-WAT IDEAL software tool is described. All functions of the BAT-WAT IDEAL software tool are described in section 3.3.2.

The main MATLAB code is provided in the Appendix A.2.

Workflow at the 3 T MR system

1. **Acquire magnitude and phase images**

   At the 3 T MR system pre calibrated scan protocols for three and six different echoes are saved in the directory $\backslash\backslash USER\backslash experimental\backslash PreClinical\backslash BAT\_WAT$. The TE times of these sequences should not be changed. All other parameters e.g. FoV or number of slices can be modified. Planing preclinical or human examinations it is important to keep the total scan in a usable range.

2. **Export the images to the DICOM server**

   The magnitude and phase images should be exported via the external DICOM server. This export procedure renames the images to the format used by the automatic image load routine of the programmed MATLAB script.

3. **Start the BAT-WAT IDEAL tool in MATLAB**

   Start the *IDEAL_chb.m* file and follow the steps as described in section 3.3.1 to chose the right input parameters.

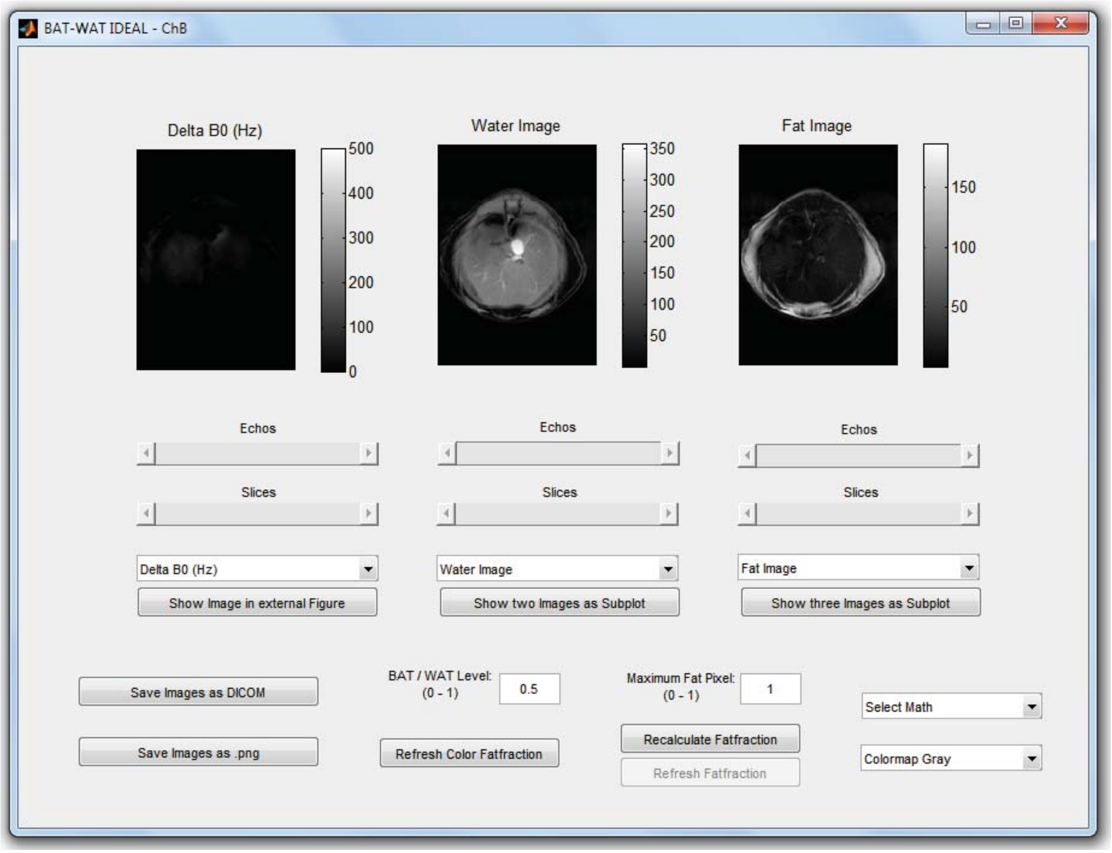

Delta B0 (Hz)

Water Image

Fat Image

BAT / WAT Level: (0 - 1) 0.5

Maximum Fat Pixel: (0 - 1) 1

Select Math

Colormap Gray

Figure 3.3.: Screenshot of the BAT-WAT-IDEAL GUI

3.3.1. Program Steps

After starting the MATLAB script following inputs are required to set the right parameters for the IDEAL algorithm and to load the images.

1. **Load standard deltaF=[0,-431] for 3 T or change it: s/c [s]**
   When deltaF is changed, it is possible to enter more than one fat frequency or enter the fat frequency for 1,5 T systems. If there is no input the fat spectrum is described with one fat peak at -431Hz.

2. **Load DICOMs auto/man? a/m [a]:**
   The automatic mode is working with the DICOM notation after the image export via the server. In the manual mode it is possible to select images with a random notation. In this mode every magnitude- and phase image is selected separately. It is possible to select images for more than three echoes but only with one slice.

3. **How many scans (Echoes) [3]:**
   Enter the number of echoes.

4. **MultiEcho/SingleEcho scans? m/s [s]:**
   Choose Multi- or Single Echo.

5. **How many slices [1]:**
   Enter the number of acquired slices.
6. **Select the first magnitude image:**
   Select the first magnitude in the automatic mode or select the images using manual mode.
7. **Load external TI=700 and TI=400 mask images? j/n [n]:** This function is disabled when there is more than one slice.

When all the images are successfully loaded the IDEAL algorithm starts with the first iteration to optimize the error of the B0 field map. The number of the current iteration and the maxDeltaB0 value are displayed for all iteration steps. After the last iteration the total calculation time is displayed. This process is repeated for each slice.
The final field map is filtered, using a Gaussian low pass and finally used to calculate the water- and the fat image. In the next step the GUI is started.

3.3.2. GUI Functions

To display the images and the results of the IDEAL algorithm an additional calculations a MATLAB GUI was programmed.
The results of the IDEAL algorithm (B_0 field map, water image and fat image) and additional image parameters were used as input parameters of the GUI function.
The images are displayed using the MATLAB *axes* function and a colorbar for to show the value range of the image. The windowing of the images can be set to different values using defined variables in the GUI file (*GUI_IDEAL.m*).

In this section the calculated images and the GUI functions are described.

Additional Calculated Images

- **Water fraction**
  Water fraction = Water image / (Water image + Fat image)
- **Fat fraction**
  Fat fraction = Fat image / (Water image + Fat image)
- **Color fat fraction**
  In the colored fat fraction all pixel with a fat fraction value above a cut off value e.g. 0,8 were colored with red and all pixel with a value between 0,4 and the cut off value were colored in green. This represents the WAT using red and the BAT using green. This colormap is combined with a amplitude image for the anatomical information.

- **in-phase image**
  in-phase image = Water image + Fat image

- **out-of-phase image**
  out-of-phase image = Water image - Fat image

- **Math result**
  The math result is the result of a simple mathematical image processing function e.g. image addition.

- **Mask Image 400** (optional)
  If a additional image acquired with an inversion time of 400 ms is loaded this mask image is visible.

- **Mask Image 700** (optional)
  If a additional image acquired with an inversion time of 700 ms is loaded this mask image is visible.

All above described images can be selected in each of the three drop down menus. The selected image is displayed above the drop down menu. If there are additional images, acquired with an STIR sequence at two different TI times (400 ms and 700 ms) the additional mask images are visible.

Show external Figure and Subplots

With the button *Show Image in external Figure* the current image from the first axis is shown in an external figure. To compare images it is possible to generate subplots in an external figure. Using the button *Show two Images as Subplot* a subplot with the current images for the first and the second axis is generated. The button *Show three Images as Subplot* generates a subplot with all current images displayed at the axes.
This external figures or subplots can be saved or modified using the standard MATLAB functions.

Colormap and Refresh Color Fatfraction

The standard colormap for the images is *gray*. The colormap can be changed to *jet* o *hot* using the colormap drop down menu. To display the the differences in the fat fraction a other colormap than *gray* is more efficient.
The separation of BAT and WAT using MRI is based on the calculated fatfraction. For BAT the fatfraction is in the range of 40-80% and for WAT higher than 80%. [5]
Because of the wide BAT range it is possible to set the cutoff between BAT and WAT for the Color Fat fraction image. In this colored fat fraction BAT is displayed as green

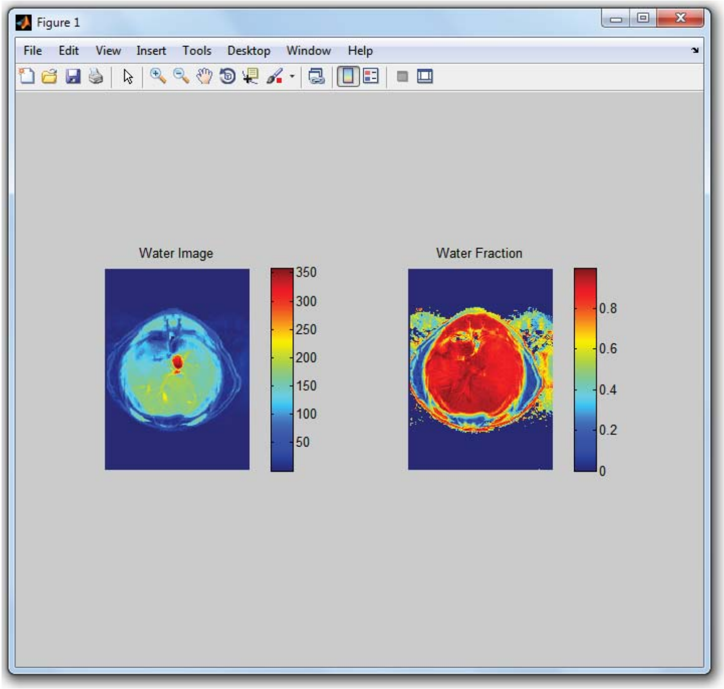

Figure 3.4.: Screenshot of an external subplot figure, using the colormap jet.

and WAT as red. Using the Button *Refresh Color Fatfraction* the the Colro Fat fraction is updated with the new cut off value.

Recalculate Fatfraction

If there are artefacts in the image and the maximum fat pixel value is less than one, tha fatfraction can be recalculated using a new maximum fat value. This value should be in the range of 0-1. With the button *Recalculate Fatfraction* the fatfraction is recalculated with the entered value. To restore the original fat fraction image the button *Refresh fatfraction* can be used.

Math Operations

The *Select Math* drop down menu allows the user to use simple mathematical operations (addition, subtraction, multiplication and division). As images for the mathematical operation the current images form axes 1 and axes 2 are used. The result (e.g. Image1 + Image2) is displayed in axes 3.

Export Images

The calculated images can be exported as DICOM or PNG images. Using the DICOM export function all images except the Color Fatfraction are saved as DICOM images in the selected folder. With the PNG export function all images are displayed in a figure with a colorbar and title and saved as PNG images. This export function is using the selected color map, so it is possible to export images with different colormaps to compare. Additional it is possible to show a image in a external image as described above and export this image to a different file type (e.g. as .fig).

4. Measurements, Observations and Results

The results of the experimental work of this project are grouped in phantom, preclinical and human results. Different images of the realized experiments and the additional test images are not provided in this report because this would exceed the amount of pages. All printed images are displayed using the standard colormap (gray). For all phantom and preclinical scans a 1H Transmit / Receive Volume Coil was used at the 3 T MR system.

4.1. Results of the Phantom Experiments

To show the feasibility of the IDEAL algorithm to separate water and fat experiments with images acquired of simple water-oil phantoms (Falcon Tubes) were realized.

Water-Oil Phantom

Resulting images of a simple water-fat separation using three different echoes and a water-oil phantom. The water was mixed with Gadolinium to reduce the T1 time as described in section 3.1.

Table 4.1.: Significant sequence parameters for a phantom scan.

Slices	1
Orientation	Transversal
Phase enc. dir.	R >>L
Phase oversampling	100%
FoV read	40 mm
FoV phase	71,9 %
Slice thickness	2,0 mm
TR	1 ms
TE	5,54 ms |6,36 ms |4,72 ms
Averages	32
Flip angle	11 deg
Base resolution	192

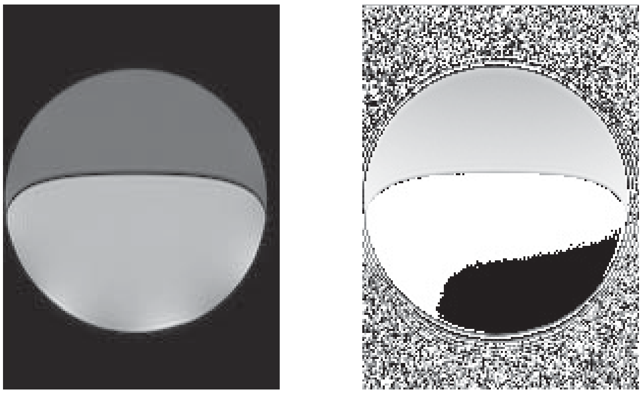

(a) Magnitude image. (b) Phase image.

Figure 4.1.: Magnitude (a) and phase image (b) of a simple water-oil phantom acquired at quadrature phase conditions.

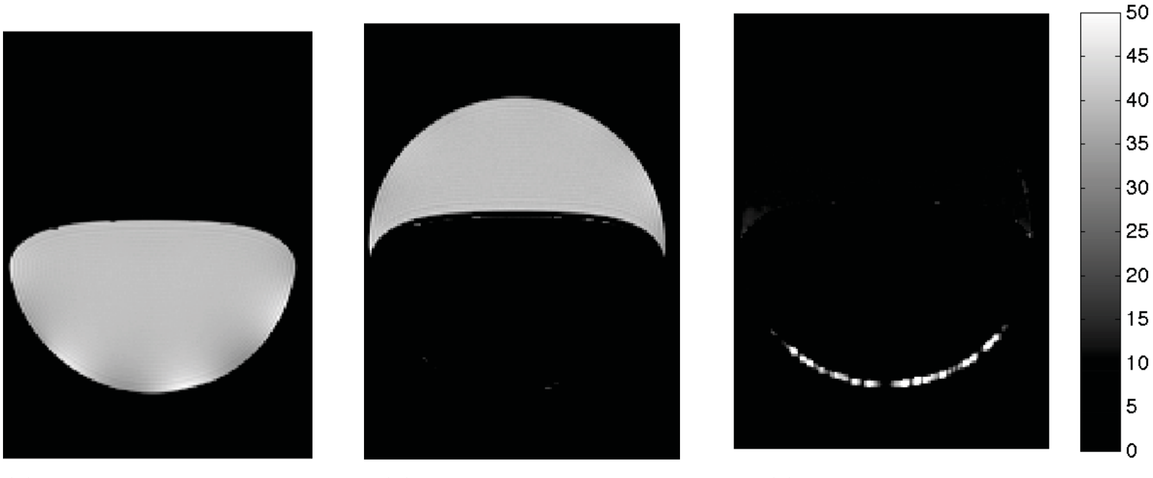

(a) Calculated water image. (b) Calculated fat image. (c) Estimated field map image.

Figure 4.2.: Water (a), fat (b) and field map image (c) of a simple water-oil phantom.

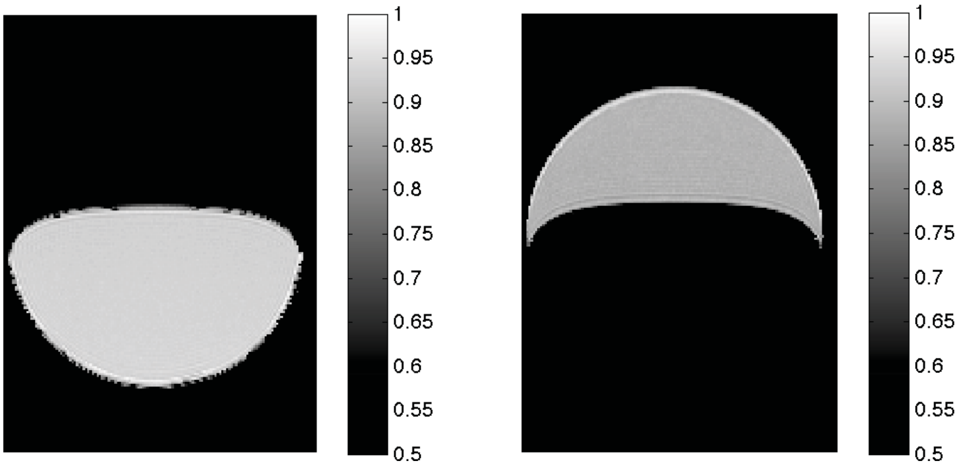

(a) Claculated water fraction.

(b) Calculated fat fraction.

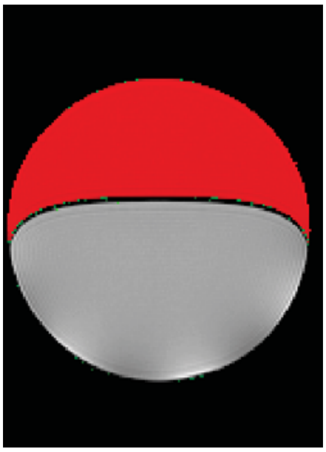

(c) Calculated color fat fraction for BAT (green) and WAT (red).

Figure 4.3.: Water fraction (a), fat fraction (b) and colored fat fraction (c) of a simple water-oil phantom.

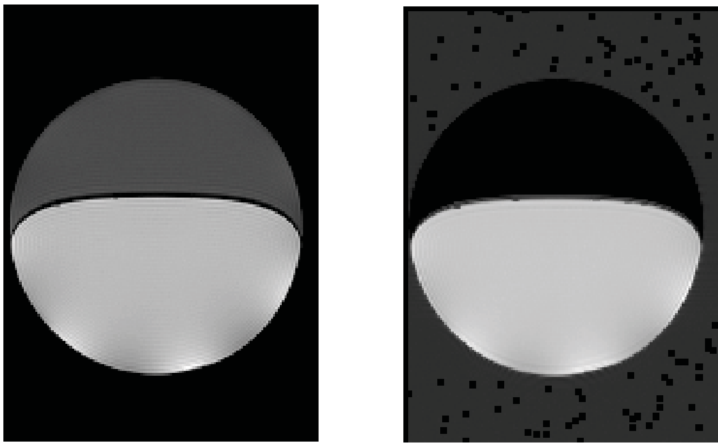

(a) Calculated in-phase image.

(b) Calculated out-of-phase image.

Figure 4.4.: Calculated in-phase (a) and out-of-phase image (b) of a simple water-oil phantom.

Comparison of Multipoint against Three Point Dixon

Comparison of the results of the multipoint fat model. The described IDEAL algorithm is extended to four fat frequencies.

Table 4.2.: Significant sequence parameters for a phantom scan with six echoes.

Slices	3
Orientatio	Transversal
Phase enc. dir.	R >>L
Phase oversampling	100%
FoV read	40 mm
FoV phase	71,9 %
Slice thickness	2,0 mm
TR	45 ms
TE	5,54 ms |5,94 ms |5,14 ms |6,36 ms |4,72 ms |5,74 ms
Averages	16
Flip angle	11 deg
Matrix	192

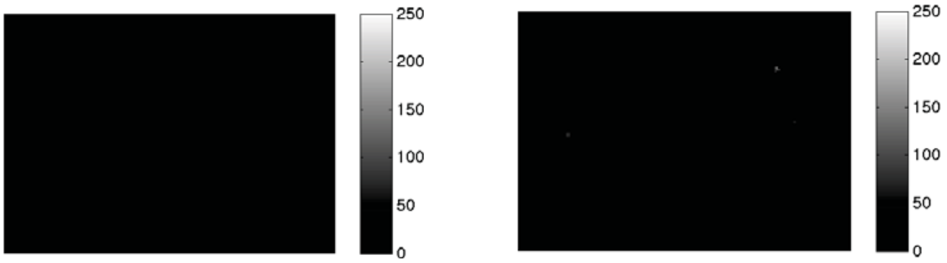

(a) $\Delta f = 0$ |-431 Hz (b) $\Delta f = 0$ |-431 |-329 Hz

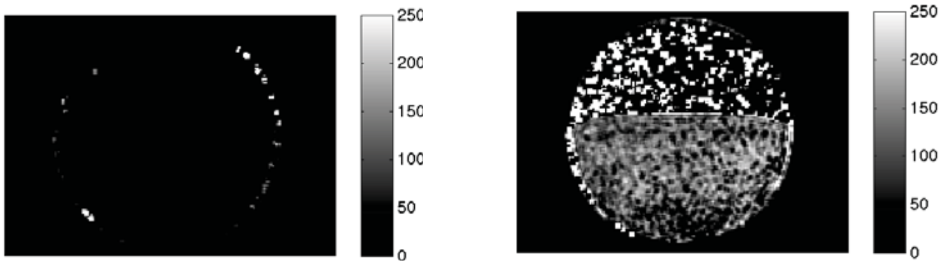

(c) $\Delta f = 0$ |-431 |-329 |-483 Hz (d) $\Delta f = 0$ |-431 |-329 |-483 |-245 Hz

Figure 4.5.: Estimated field map of a simple water-oil phantom using multipoint Dixon water-fat separation. Using one (a), two (b), three (c) and four (d) fat frequencies.

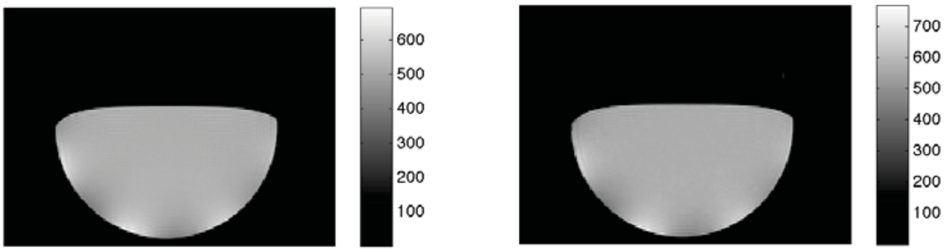

(a) $\Delta f = 0$ |-431 Hz

(b) $\Delta f = 0$ |-431 |-329 Hz

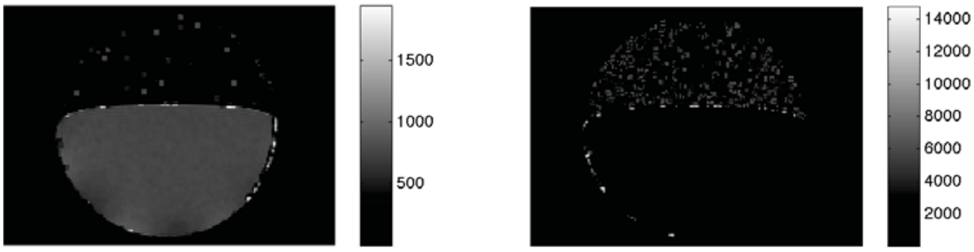

(c) $\Delta f = 0$ |-431 |-329 |-483 Hz

(d) $\Delta f = 0$ |-431 |-329 |-483 |-245 Hz

Figure 4.6.: Calculated water image of a simple water-oil phantom using multipoint Dixon water-fat separation. Using one (a), two (b), three (c) and four (d) fat frequencies.

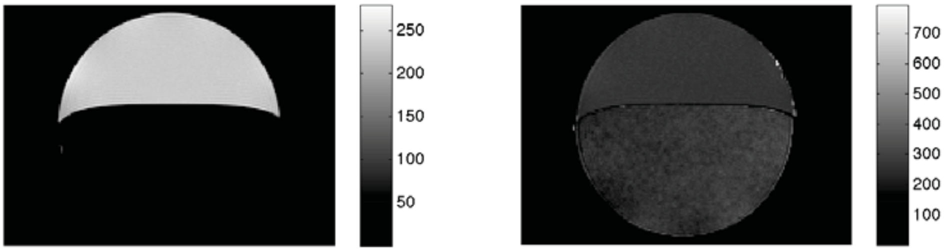

(a) $\Delta f = 0$ |-431 Hz

(b) $\Delta f = 0$ |-431 |-329 Hz

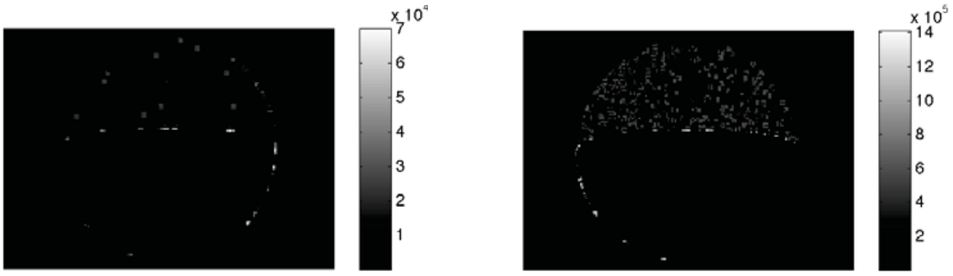

(c) $\Delta f = 0$ |-431 |-329 |-483 Hz

(d) $\Delta f = 0$ |-431 |-329 |-483 |-245 Hz

Figure 4.7.: Calculated fat image of a simple water-oil phantom using multipoint Dixon water-fat separation. Using one (a), two (b), three (c) and four (d) fat frequencies.

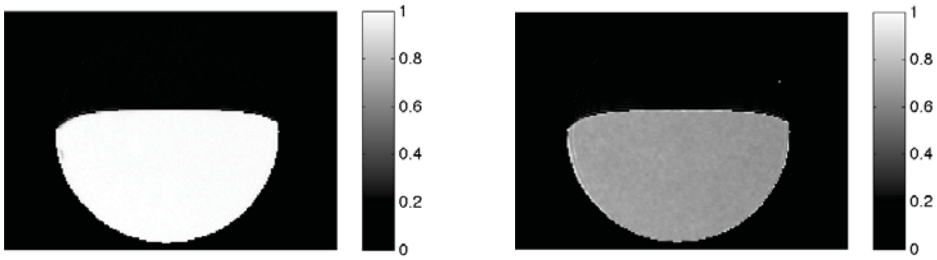

(a) $\Delta f = 0$ |-431 Hz (b) $\Delta f = 0$ |-431 |-329 Hz

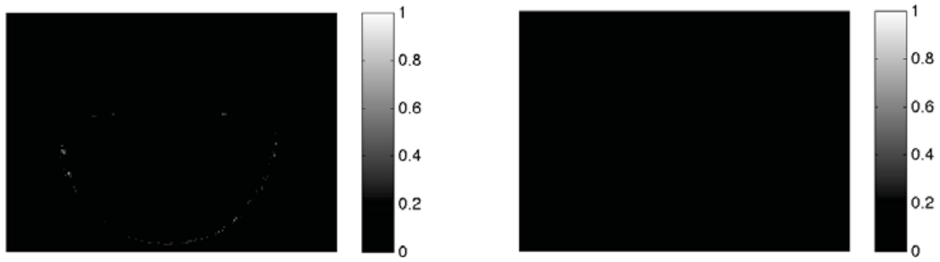

(c) $\Delta f = 0$ |-431 |-329 |-483 Hz (d) $\Delta f = 0$ |-431 |-329 |-483 |-245 Hz

Figure 4.8.: Calculated water fraction of a simple water-oil phantom using multipoint Dixon water-fat separation. Using one (a), two (b), three (c) and four (d) fat frequencies.

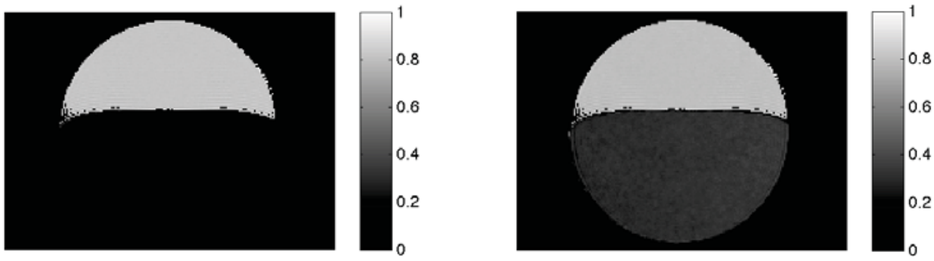

(a) $\Delta f = 0$ |-431 Hz (b) $\Delta f = 0$ |-431 |-329 Hz

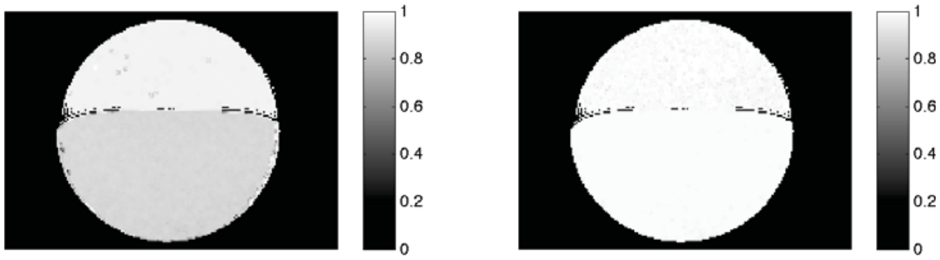

(c) $\Delta f = 0$ |-431 |-329 |-483 Hz (d) $\Delta f = 0$ |-431 |-329 |-483 |-245 Hz

Figure 4.9.: Calculated fat fraction of a simple water-oil phantom using multipoint Dixon water-fat separation. Using one (a), two (b), three (c) and four (d) fat frequencies.

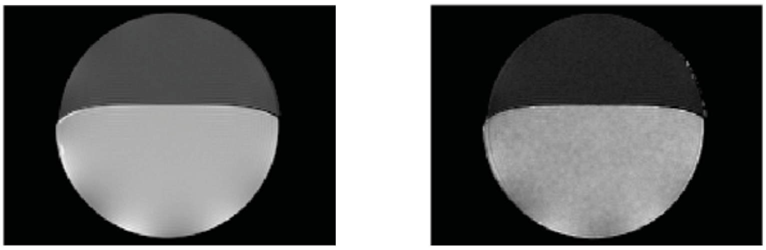

(a) $\Delta f = 0$ |-431 Hz

(b) $\Delta f = 0$ |-431 |-329 Hz

(c) $\Delta f = 0$ |-431 |-329 |-483 Hz

(d) $\Delta f = 0$ |-431 |-329 |-483 |-245 Hz

Figure 4.10.: Calculated in-phase images of a simple water-oil phantom using multipoint Dixon water-fat separation. Using one (a), two (b), three (c) and four (d) fat frequencies.

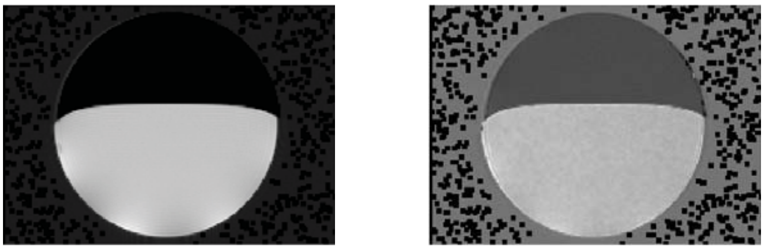

(a) $\Delta f = 0$ |-431 Hz

(b) $\Delta f = 0$ |-431 |-329 Hz

(c) $\Delta f = 0$ |-431 |-329 |-483 Hz

(d) $\Delta f = 0$ |-431 |-329 |-483 |-245 Hz

Figure 4.11.: Calculated out-of-phase image of a simple water-oil phantom using multipoint Dixon water-fat separation. Using one (a), two (b), three (c) and four (d) fat frequencies.

Spectral Measurements

Additional to the acquired magnitude and phase images of the water-oil phantoms a Single-Voxel-Spectroscopy was performed to measure the spectrum of a pixel containing water and oil.

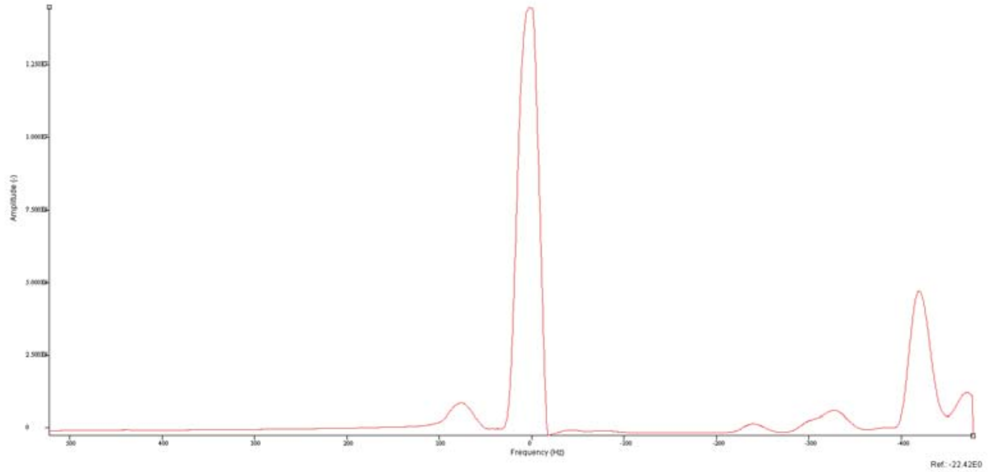

Figure 4.12.: Spectrum of a pixel containing water and fat, measured in a simple water-fat-phantom.

4.2. Results of the Human Experiments

4.2.1. Sagittal Human Knee acquired at 3 T

Results of a human knee scanned at three different echo times and with three sagittal slices. Scanned at 3 T with a standard knee coil.

Table 4.3.: Significant sequence parameters for a human scan at 3 T.

Slices	3, Distance factor 10%
Phase enc. dir.	A >>P
FoV read	200 mm
Slice thickness	2,0 mm
TR	42 ms
TE	5,5 ms |6,4 ms |4,7 ms
Averages	16
Flip angle	11 deg
Base resolution	320

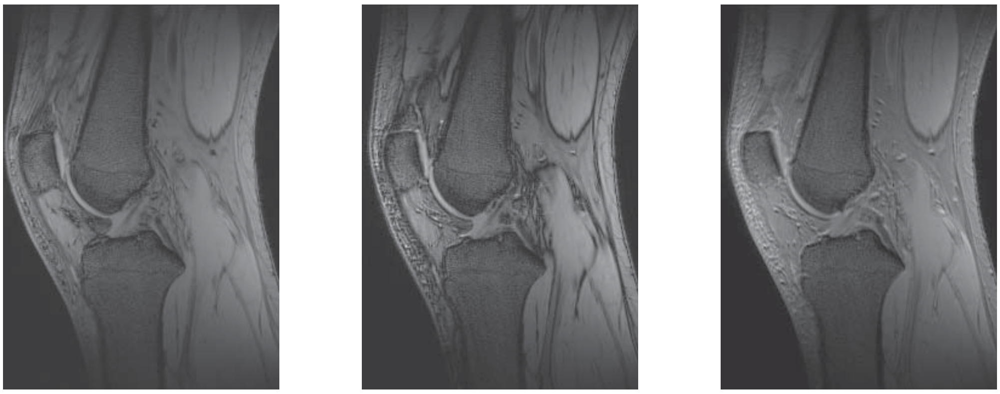

(a) Quadrature phase.

(b) Quadrature phase +120°.

(c) Quadrature phase −120°.

Figure 4.13.: Magnitude images of a sagttial human knee acquired at 3 T. Image of the first echo (a), the second echo (b) and the third echo (c).

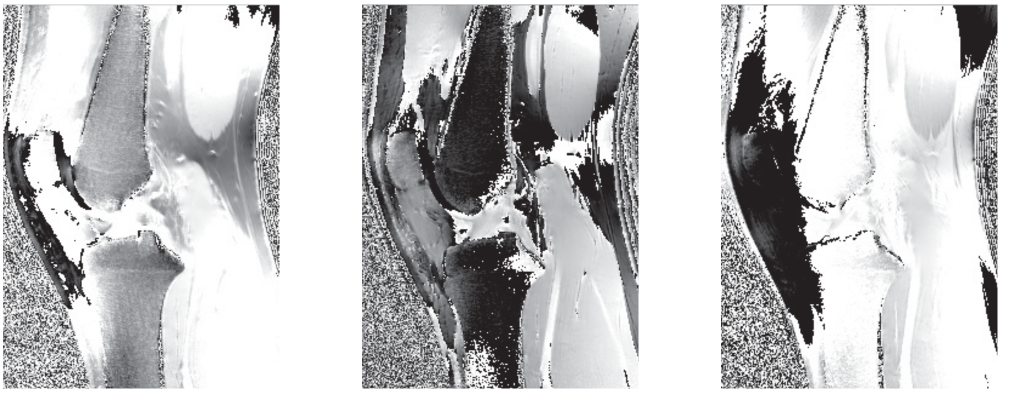

(a) Quadrature phase.
(b) Quadrature phase +120°.
(c) Quadrature phase −120°.

Figure 4.14.: Phase images of a sagttial human knee acquired at 3 T. Image of the first echo (a), the second echo (b) and the third echo (c).

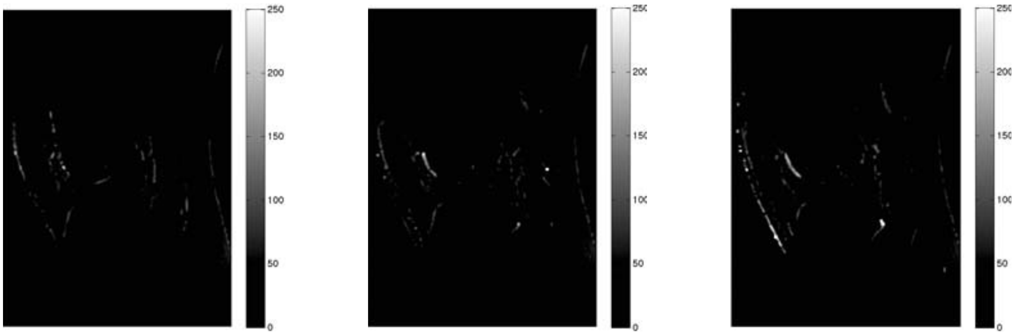

(a) First slice.
(b) Second slice.
(c) Third slice.

Figure 4.15.: Estimated field map images of a sagittal human knee acquired at 3 T with three slices. Image of the first slice (a), the second slice (b) and the third slice (c).

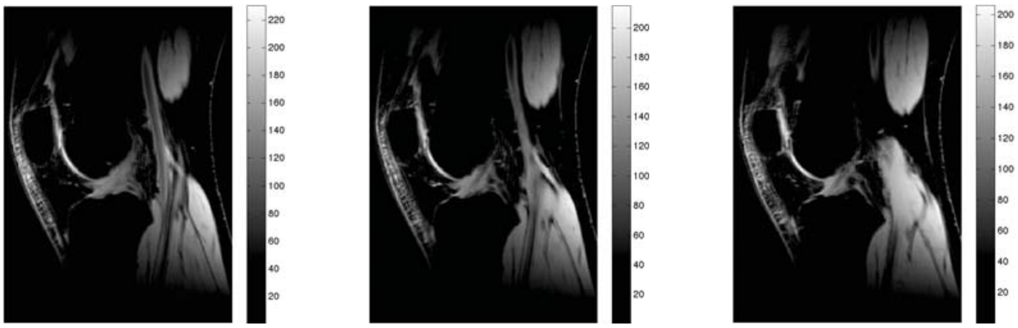

(a) First slice.
(b) Second slice.
(c) Third slice.

Figure 4.16.: Calculated water images of a sagittal human knee acquired at 3 T with three slices. Image of the first slice (a), the second slice (b) and the third slice (c).

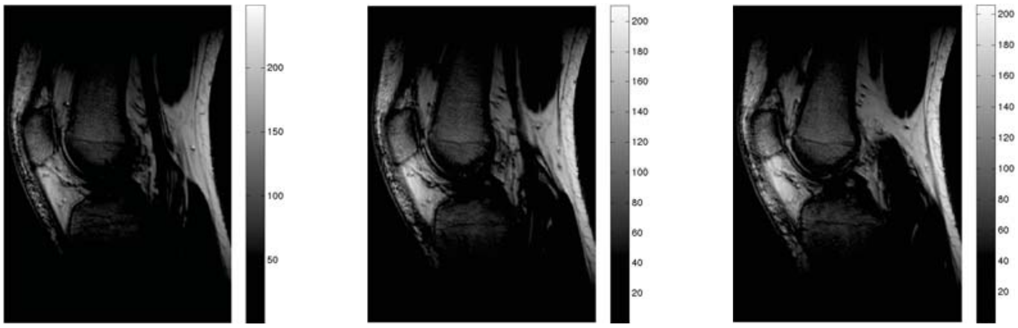

(a) First slice. (b) Second slice. (c) Third slice.

Figure 4.17.: Calculated fat images of a sagittal human knee acquired at 3 T with three slices. Image of the first slice (a), the second slice (b) and the third slice (c).

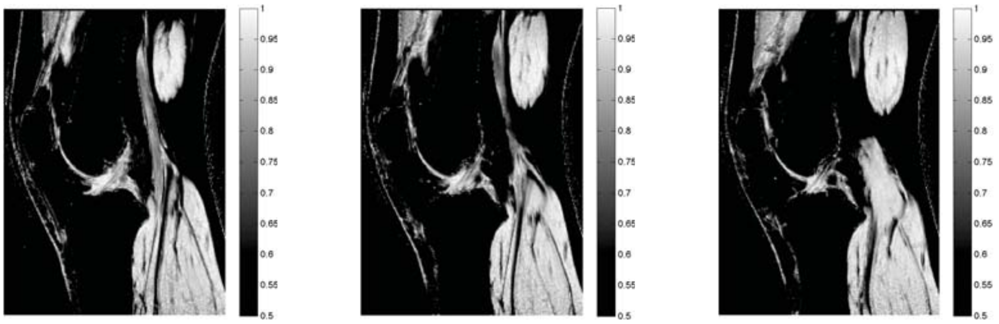

(a) First slice. (b) Second slice. (c) Third slice.

Figure 4.18.: Calculated water fraction images of a sagittal human knee acquired at 3 T with three slices. Image of the first slice (a), the second slice (b) and the third slice (c).

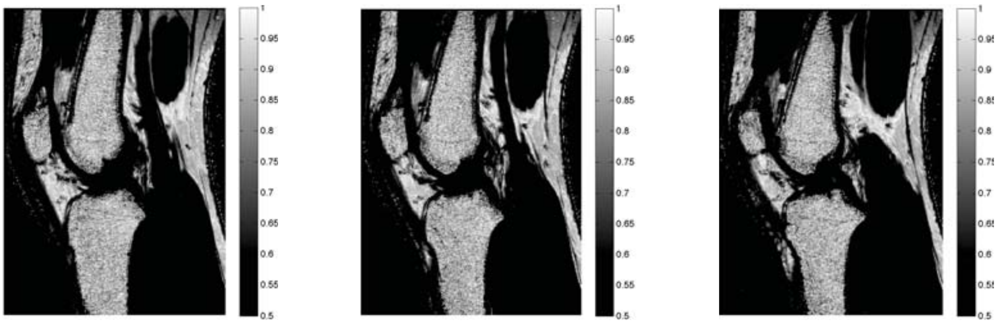

(a) First slice. (b) Second slice. (c) Third slice.

Figure 4.19.: Calculated fat fraction images of a sagittal human knee acquired at 3 T with three slices. Image of the first slice (a), the second slice (b) and the third slice (c).

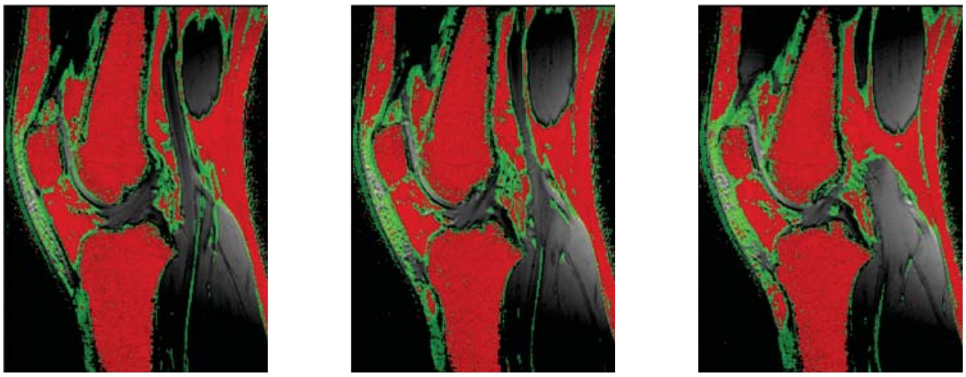

(a) First slice. (b) Second slice. (c) Third slice.

Figure 4.20.: Calculated color fat fraction images of a sagittal human knee acquired at 3 T with 3 slices. WAT is colored red and apparent BAT (partial-volume artifacts) is colored green. Image of the first slice (a), the second slice (b) and the third slice (c).

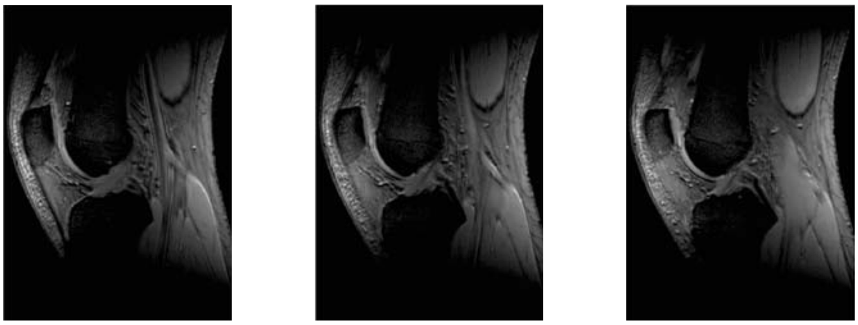

(a) First slice. (b) Second slice. (c) Third slice.

Figure 4.21.: Calculated in-phase images of a sagittal human knee acquired at 3 T with three slices. Image of the first slice (a), the second slice (b) and the third slice (c).

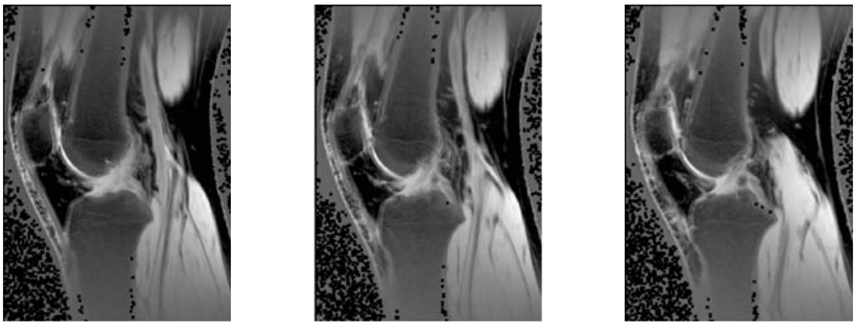

(a) First slice. (b) Second slice. (c) Third slice.

Figure 4.22.: Calculated out-of-phase images of a sagittal human knee acquired at 3 T with three slices. Image of the first slice (a), the second slice (b) and the third slice (c).

4.2.2. Axial Human Abdomen acquired at 3 T

Results of an axial human abdomen with one slice acquired at 3 T. To a existing study protocol this additional IDEAL sequence was added.

Table 4.4.: Significant sequence parameters for a human abdomen scan at 3 T.

Slices	1
FoV read	500 mm
Slice thickness	10,0 mm
TR	15 ms
TE	5,5 ms |6,4 ms |4,7 ms
Averages	4
Flip angle	11 deg
Base resolution	256

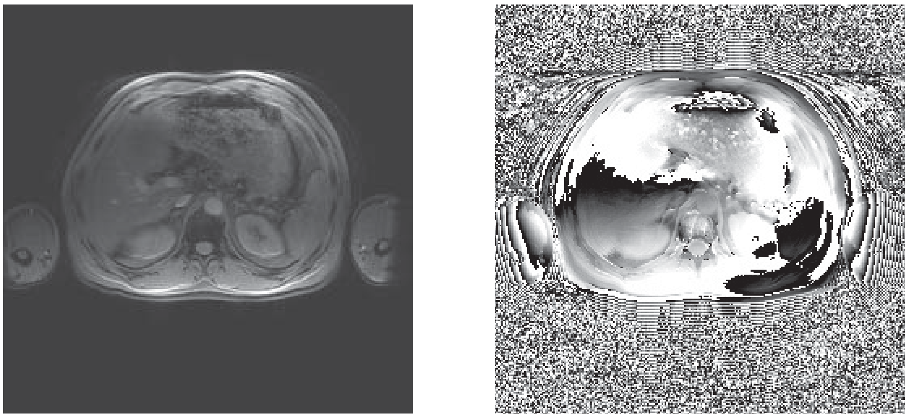

(a) Magnitude image.

(b) Phase image.

Figure 4.23.: Magnitude (a) and phase image (b) of a human abdomen with one slice at the first echo (TE=5,5 ms).

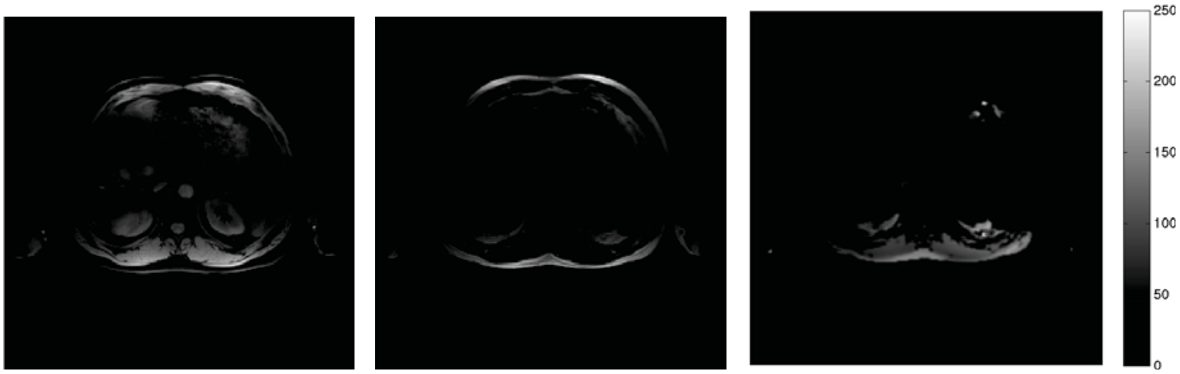

(a) Calculated water image. (b) Calculated fat image. (c) Field map image.

Figure 4.24.: Calculated water (a), fat (b) and field map image (c) of a human abdomen with one slice.

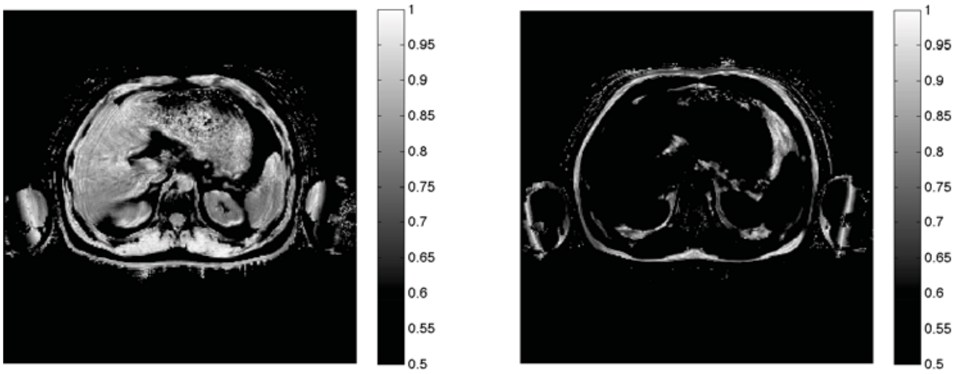

(a) Calculated water fraction. (b) Calculated fat fracion.

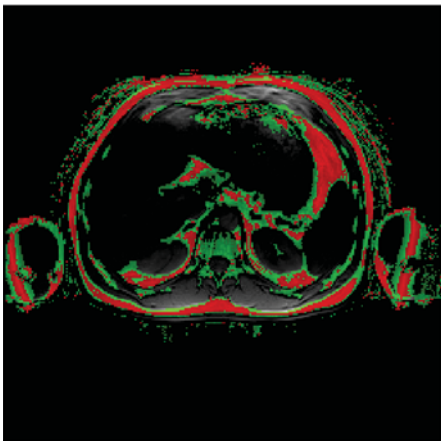

(c) Color fat fraction for BAT (green) and WAT (red).

Figure 4.25.: Calculated water fraction (a), fat fraction (b) and colored fat fraction (c) of a human abdomen acquired at 3 T. The apparent BAT in image (c) is caused by partial-volume artifacts.

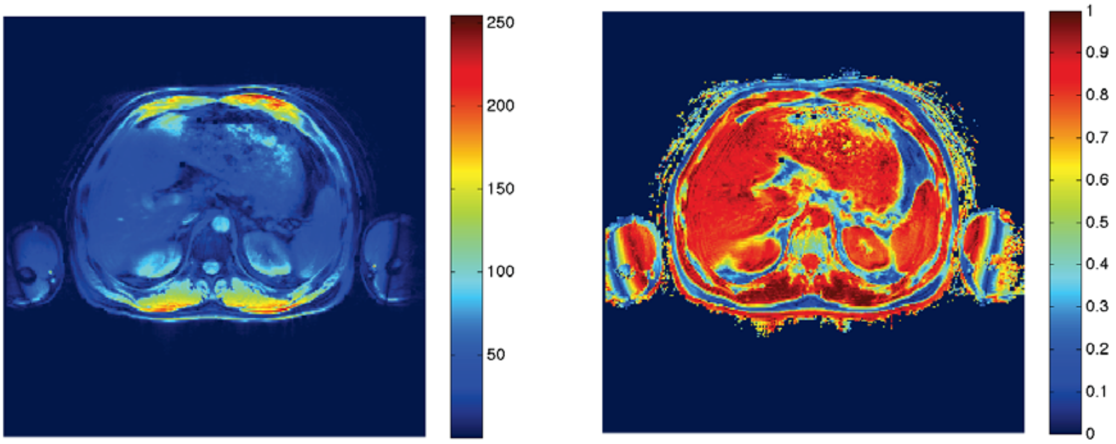

(a) Calculated water image.

(b) Calculated water fraction.

Figure 4.26.: Calculated water image (a) and water fraction (b) of a human abdomen acquired at 3 T and colored using the colormap jet.

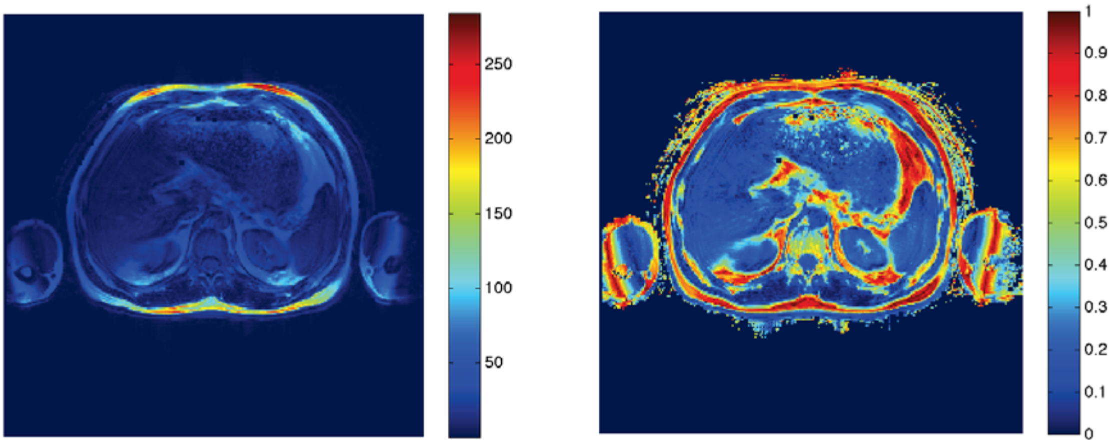

(a) Calculated fat image.

(b) Calculated fat fraction.

Figure 4.27.: Calculated fat image (a) and fat fraction (b) of a human abdomen acquired at 3 T and colored using the colormap jet.

4.2.3. Sagittal Human Knee acquired at 1,5 T

Images of a sagittal human knee acquired at 1,5 T to show the feasibility of the IDEAL algorithm at different B0 fields.

Table 4.5.: Significant sequence parameters for a human scan at 1,5T.

Slices	2, Distance factor 10%
Phase enc. dir.	A >>P
FoV read	137 mm
Slice thickness	2,0 mm
TR	50 ms
TE	10,7 ms |9,13 ms |12,3 ms
Averages	16
Flip angle	11 deg
Base resolution	192

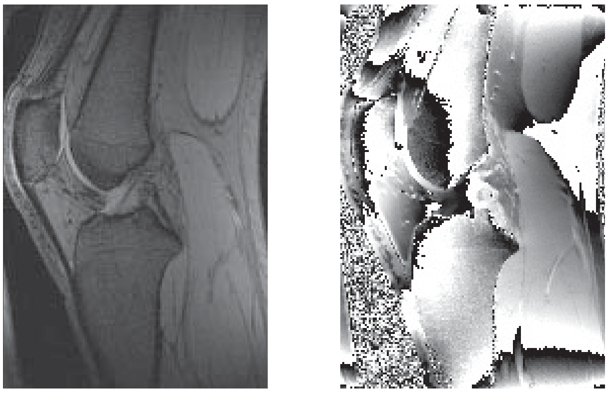

(a) Magnitude image.

(b) Phase image.

Figure 4.28.: Magnitude (a) and phase image (b) of a human knee acquired at 1,5 T with the first echo at TE=10,7 ms.

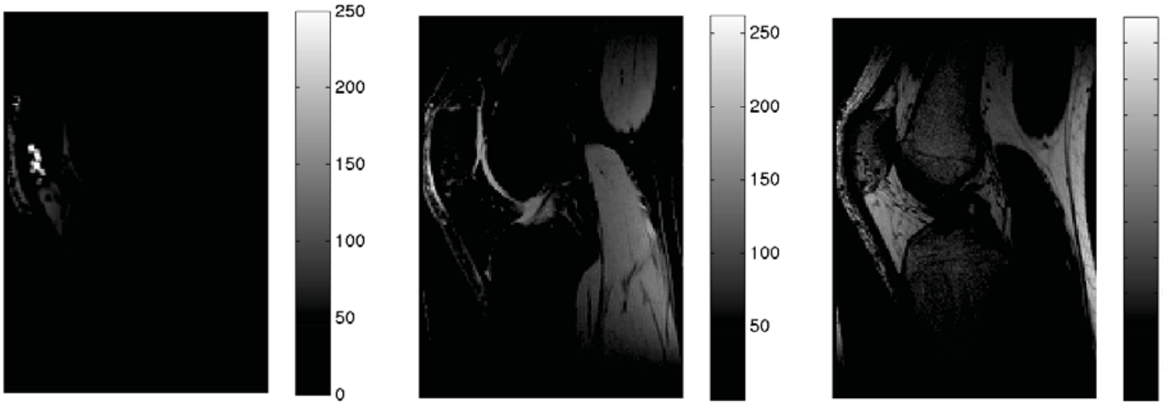

(a) Field map image.

(b) Calculated water image.

(c) Calculated fat image.

Figure 4.29.: Field map (a), water (b) and fat image (c) of a human knee acquired at 1,5 T.

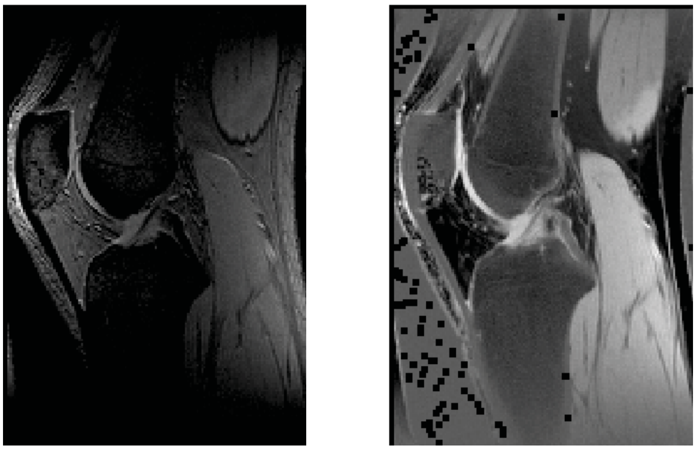

(a) Calculated in-phase image.

(b) Calculated out-of-phase image.

Figure 4.30.: Calculated in-phase (a) and out-of-phase image (b) of a human knee acquired at 1,5 T.

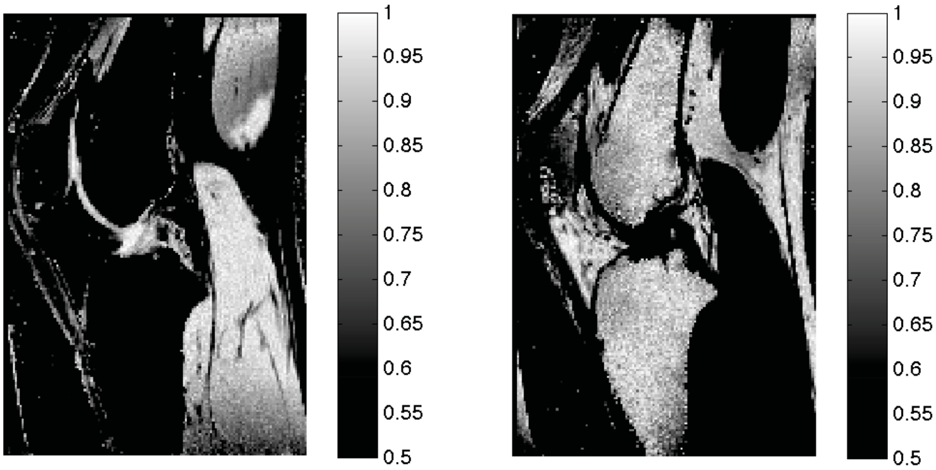

(a) Calculated water fraction.

(b) Calculated fat fracion.

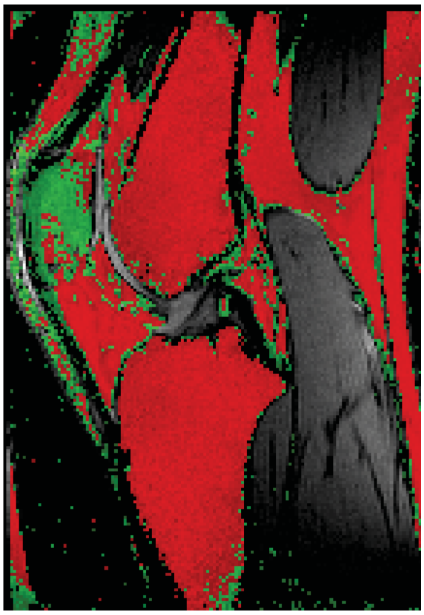

(c) Color fat fraction for BAT (green) and WAT (red).

Figure 4.31.: Calculated water fraction (a), fat fraction (b) and colored fat fraction (c) of a human knee acquired at 1,5 T. The apparent BAT in image (c) is caused by partial-volume artifacts.

4.3. Results of the Preclinical Experiments

The preclinical experiments with different mice were used to evaluate the BAT-WAT separation by using MRI and to evaluate the modified method. For a better differentiation of the tissue the water and fat fraction images were colored with different colormaps.

4.3.1. 2 Week old Mouse

For this first preclinical experiments a 2 week old mouse was scanned using a GRE sequence with one slice. By using a STIR sequence two additional images with different inversion times were acquired for the modified separation approach.

Table 4.6.: Significant GRE sequence parameters for a mouse scan.

Slices	1
Phase enc. dir.	A >>P
FoV read	40 mm
FoV phase	71,9%
Slice thickness	2,0 mm
TR	15 ms
TE	5,54 ms |6,36 ms |4,72 ms
Averages	16
Flip angle	11 deg
Base resolution	192

Table 4.7.: Significant STIR sequence parameters

Slices	1
Phase enc. dir.	A >>P
FoV read	40 mm
FoV phase	71,9%
Slice thickness	2,0 mm
TR	2000 ms
TE	13 ms
Averages	1
TI	400 ms |700 ms
Flip angle	180 deg
Base resolution	192

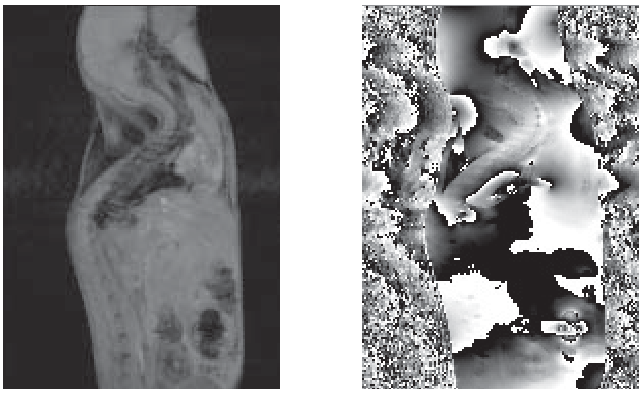

(a) Magnitude image.

(b) Phase image.

Figure 4.32.: Magnitude (a) and phase image (b) of a 2 week old mouse acquired at 3 T with the first echo at TE=5,5 ms.

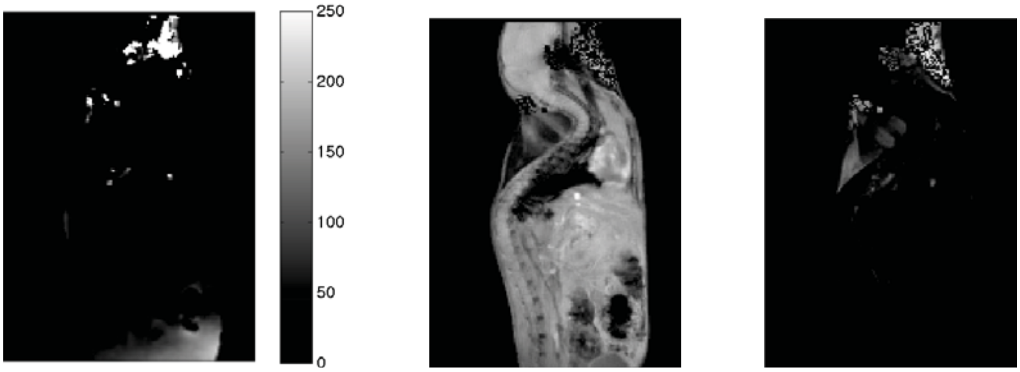

(a) Field map image.

(b) Calculated water image.

(c) Calculated fat image.

Figure 4.33.: Field map (a), water (b) and fat image (c) of a 2 week old mouse.

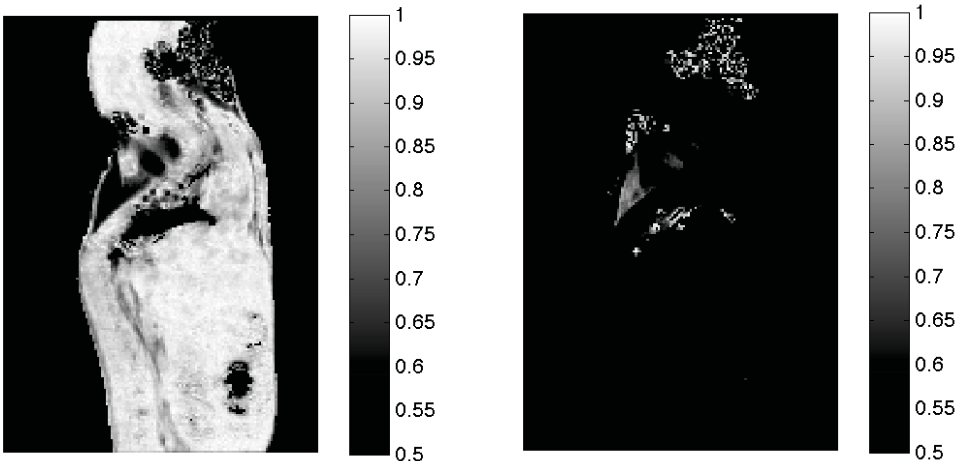

(a) Calculated water fraction.

(b) Calculated fat fracion.

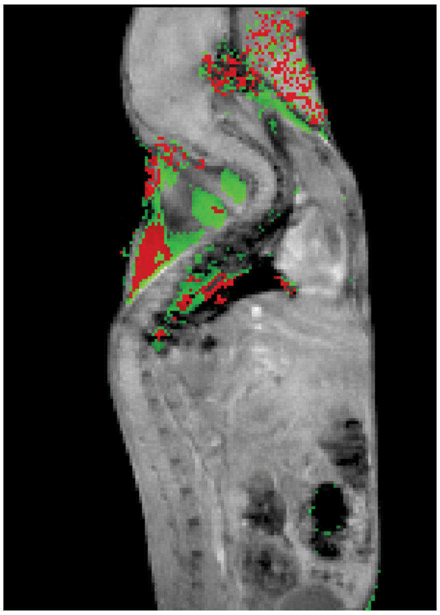

(c) Color fat fraction of BAT (green) and WAT (red).

Figure 4.34.: Calculated water fraction (a), fat fraction (b) and colored fat fraction (c) of 2 week old mouse. Some partial-volume artifacts occurred in the throat region.

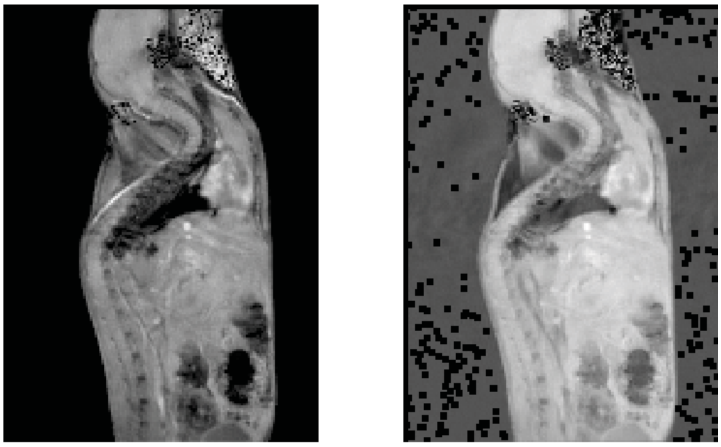
(a) In-phase image. (b) Out-of-phase image.

Figure 4.35.: In-phase (a) and out-of-phase image (b) of a 2 week old mouse.

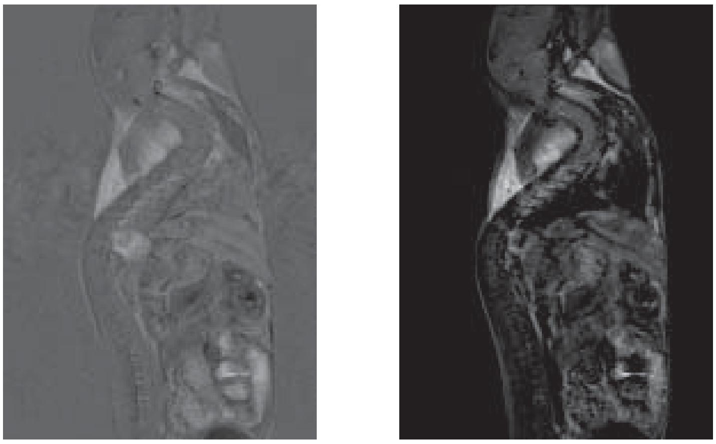
(a) TI=400 ms (BAT). (b) TI=700 ms (WAT).

Figure 4.36.: Images at two different inversion times (TI) of a 2 week old mouse.

Comparison of different colormaps

Different colormaps can be used to enhance the difference of BAT and WAT in the calculated images. In this section the impact of different colormaps is demonstrated.

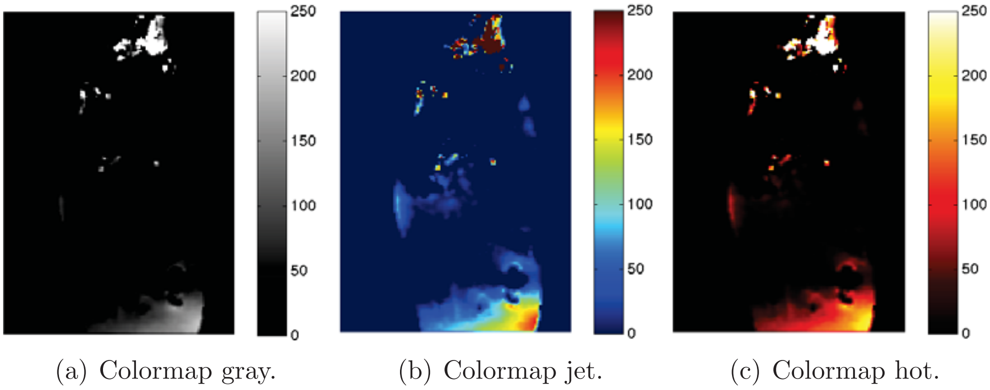

(a) Colormap gray. (b) Colormap jet. (c) Colormap hot.

Figure 4.37.: Calculated filed map image of a 2 week old mouse displayed with different colormaps. Using colormap gray (a), jet (b) and hot (c).

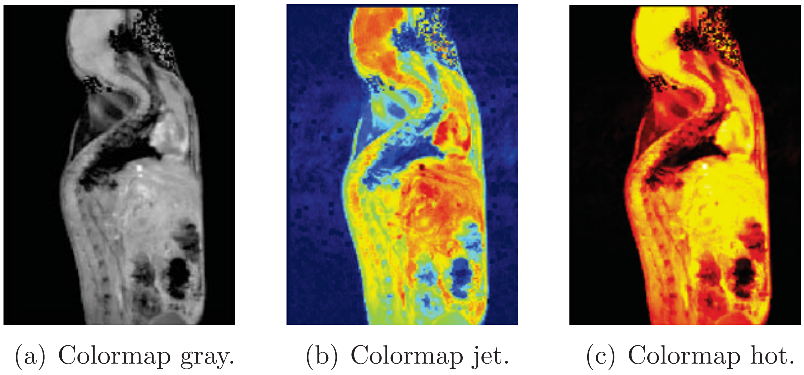

(a) Colormap gray. (b) Colormap jet. (c) Colormap hot.

Figure 4.38.: Calculated water image of a 2 week old mouse using three different colormaps. Using colormap gray (a), jet (b) and hot (c).

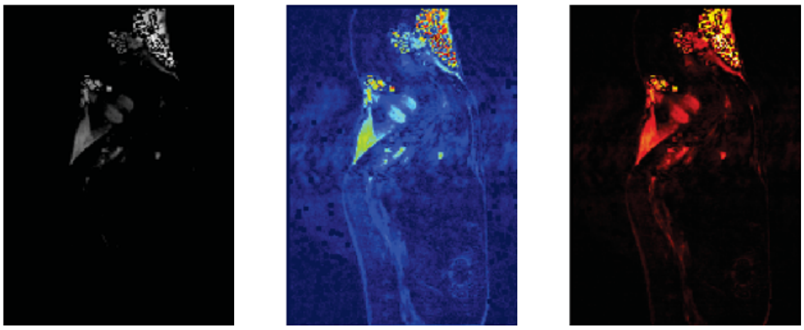

(a) Colormap gray. (b) Colormap jet. (c) Colormap hot.

Figure 4.39.: Calculated fat image of a 2 week old mouse using three different colormaps. Using colormap gray (a), jet (b) and hot (c).

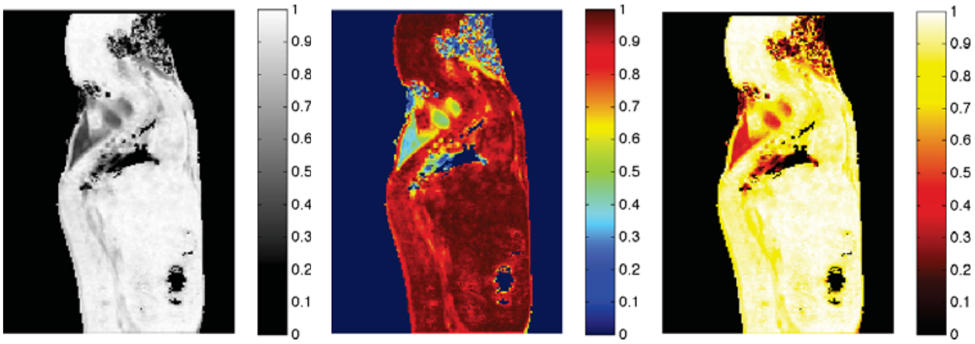

(a) Colormap gray. (b) Colormap jet. (c) Colormap hot.

Figure 4.40.: Calculated water fraction of a 2 week old mouse using three different colormaps. Using colormap gray (a), jet (b) and hot (c).

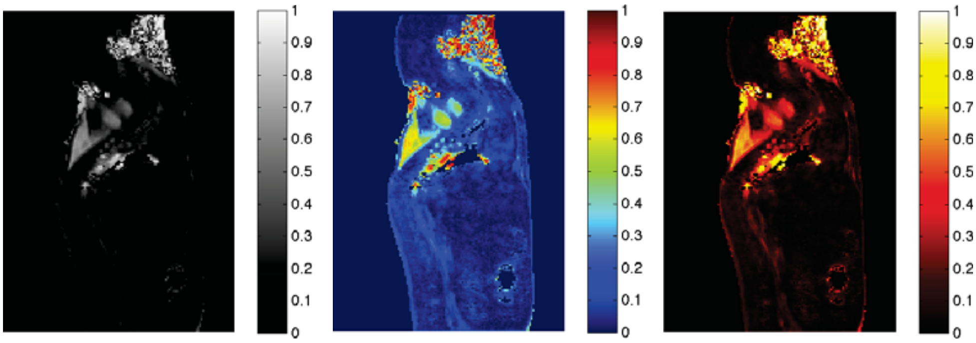

(a) Colormap gray. (b) Colormap jet. (c) Colormap hot.

Figure 4.41.: Calculated fat fraction of a 2 week old mouse displayed with different colormaps. Using colormap gray (a), jet (b) and hot (c).

4.3.2. 36 Week old Mouse with Different Echoes

In this experiment the impact of the echo spacing and the number of echoes is evaluated. For all test cases the fat was modelled with one fat peak at -431 Hz. The results of a standard three point method were compared with images acquired using three asymmetric and six symmetric echoes.

Table 4.8.: Significant GRE sequence parameters for a mouse scan with 6 echoes.

Slices	1
Phase enc. dir.	A >>P
Phase oversampling	0%
FoV read	40 mm
FoV phase	71,9%
Slice thickness	2,0 mm
TR	15 ms
TE	5,54 ms |5,94 ms |5,14 ms |6,36 ms |4,72 ms |5,74 ms
Averages	16
Flip angle	11 deg
Base resolution	192

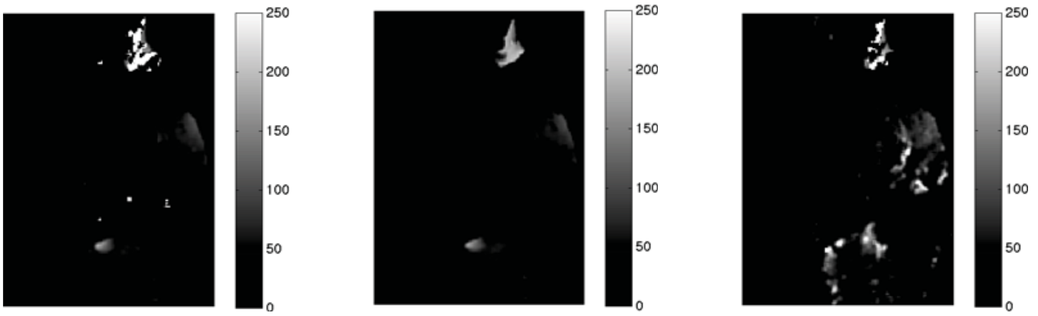

(a) 3 echoes.
(b) 6 echoes.
(c) 3 asymmetric echoes.

Figure 4.42.: Calculated field map images of a 36 week old mouse by using three (a), six (b) and three asymmetric echoes (c).

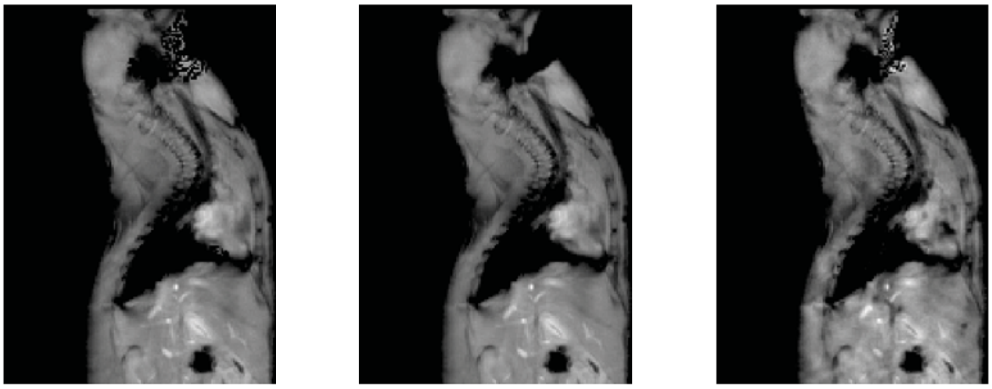

(a) 3 echoes. (b) 6 echoes. (c) 3 asymmetric echoes.

Figure 4.43.: Calculated water images of a 36 week old mouse by using three (a), six (b) and three asymmetric echoes (c).

(a) 3 echoes. (b) 6 echoes. (c) 3 asymmetric echoes.

Figure 4.44.: Calculated fat images of a 36 week old mouse by using three (a), six (b) and three asymmetric echoes (c).

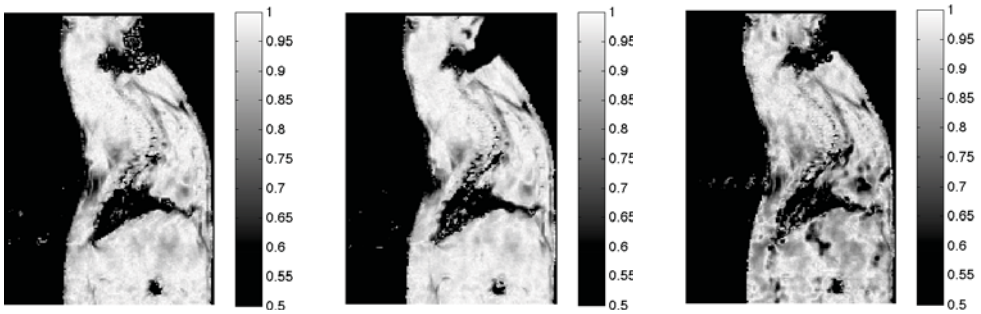

(a) 3 echoes. (b) 6 echoes. (c) 3 asymmetric echoes.

Figure 4.45.: Calculated water fractions of a 36 week old mouse by using three (a), six (b) and three asymmetric echoes (c).

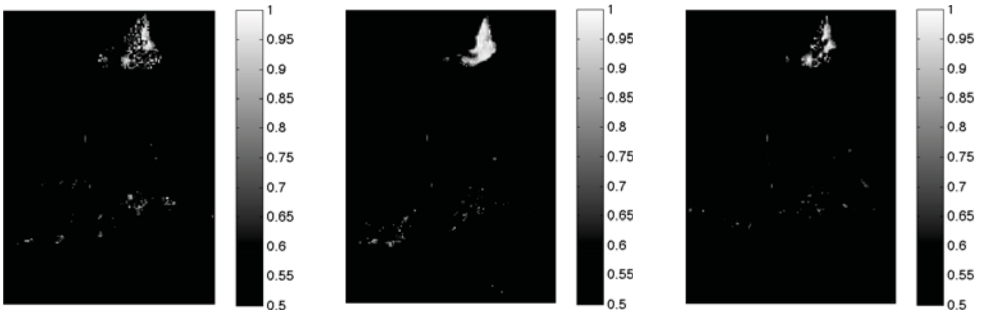

(a) 3 echoes. (b) 6 echoes. (c) 3 asymmetric echoes.

Figure 4.46.: Calculated fat fractions of a 36 week old mouse by using three (a), six (b) and three asymmetric echoes (c).

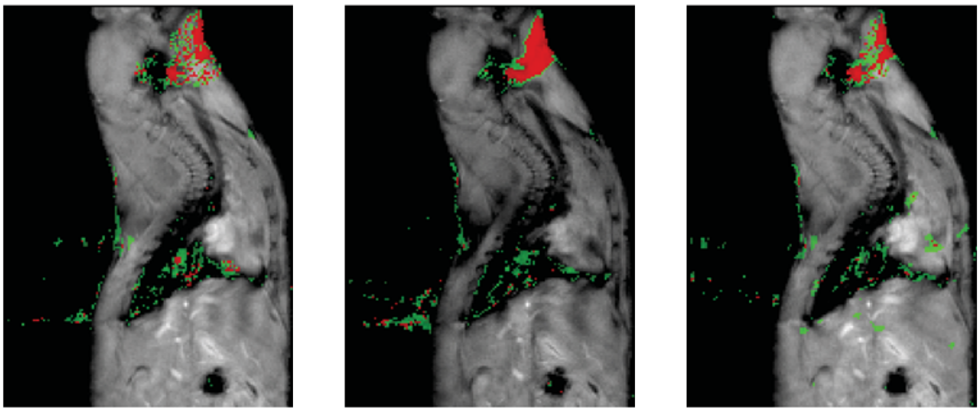

(a) 3 echoes. (b) 6 echoes. (c) 3 asymmetric echoes.

Figure 4.47.: Calculated colored fat fraction with apparent BAT (green) and WAT(red) of a 36 week old mouse by using three (a), six (b) and three asymmetric echoes (c). False values for BAT and WAT are caused by partial-volume artifacts.

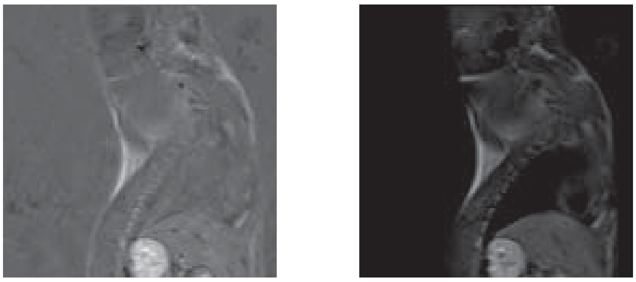

(a) TI = 400 ms. (b) TI = 700 ms.

Figure 4.48.: Images of a 36 week old mouse acquired with an inversion time of 400 ms (a) and 700 ms (b) using a STIR sequence.

4.3.3. Comparison of Three Different Mouse Types

During the examination of mice for a different study additionally sequences for the BAT-WAT separation were scanned. A GRE sequence with one axial slice in the abdomen of the mouse was used. The resulting images of three different mouse types are compared.

Mouse no. 12: female, 46 weeks, Black 6
Mouse no. 30: female, 28 weeks, Transgene (with tumor)
Mouse no. 33: male, 28 weeks, Wildtype

Table 4.9.: Significant sequence parameters for scans with different mouse types.

Slices	1
Phase enc. dir.	A >>P
FoV read	27 mm
FoV phase	71,9%
Slice thickness	2,0 mm
TR	15 ms
TE	5,54 ms |6,36 ms |4,72 ms
Averages	32
Flip angle	11 deg
Base resolution	192

(a) Mouse no. 12. (b) Mouse no. 30. (c) Mouse no. 33.

Figure 4.49.: Magnitude images of a Black 6 (a), a Transgene (b) and a Wildtype mouse (c).

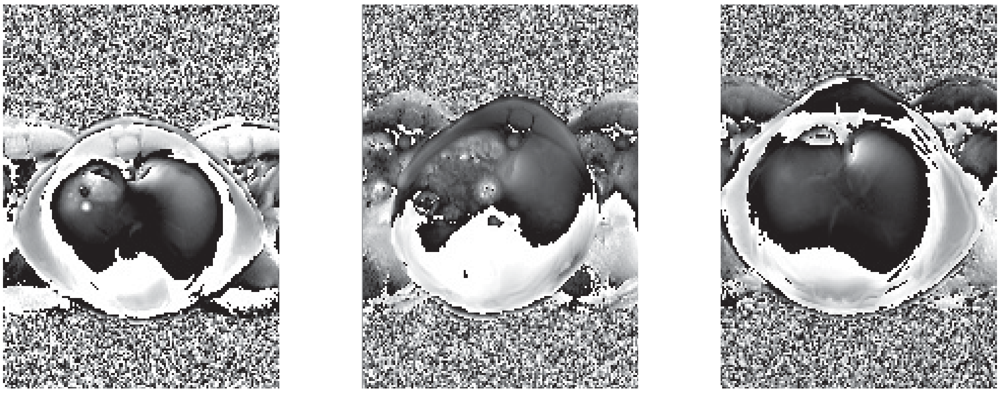

(a) Mouse no. 12.

(b) Mouse no. 30.

(c) Mouse no. 33.

Figure 4.50.: Phase images of a Black 6 (a), a Transgene (b) and a Wildtype mouse (c).

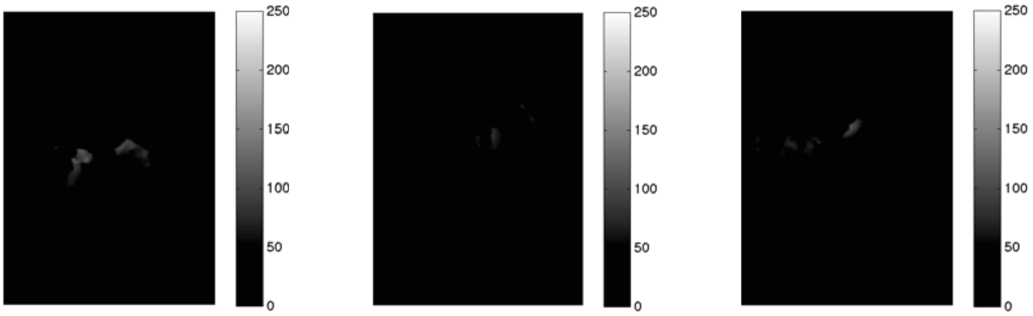

(a) Mouse no. 12.

(b) Mouse no. 30.

(c) Mouse no. 33.

Figure 4.51.: Calculated field map images of a Black 6 (a), a Transgene (b) and a Wildtype mouse (c).

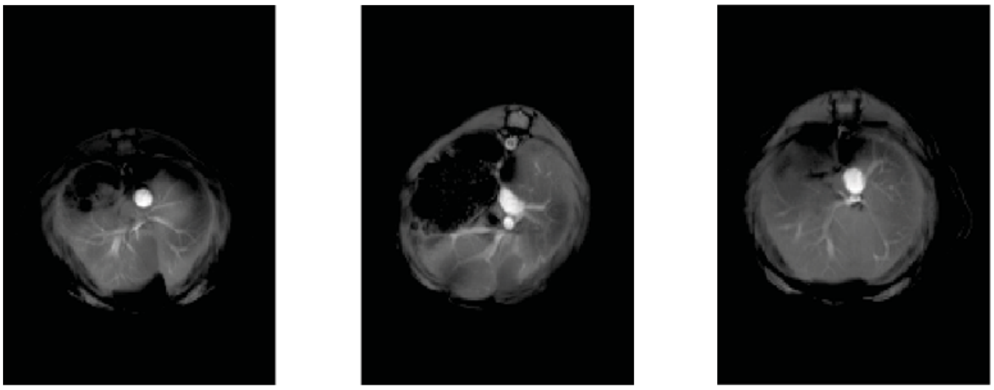

(a) Mouse no. 12.

(b) Mouse no. 30.

(c) Mouse no. 33.

Figure 4.52.: Calculated water images of a Black 6 (a), a Transgene (b) and a Wildtype mouse (c).

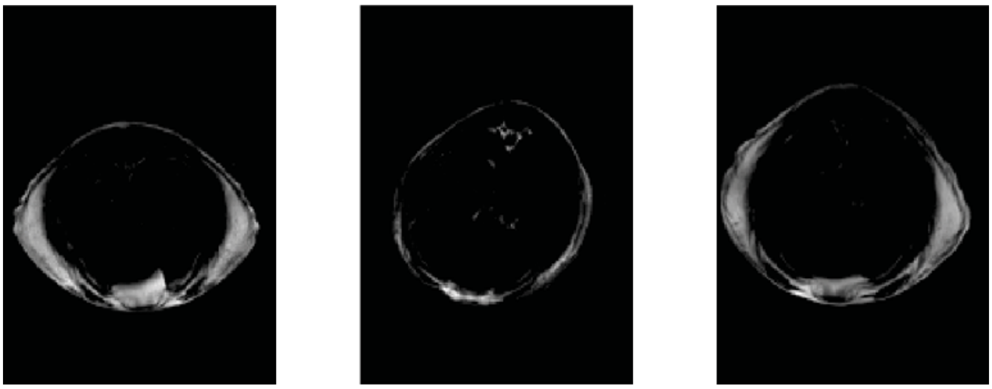

(a) Mouse no. 12. (b) Mouse no. 30. (c) Mouse no. 33.

Figure 4.53.: Calculated fat images of a Black 6 (a), a Transgene (b) and a Wildtype mouse (c).

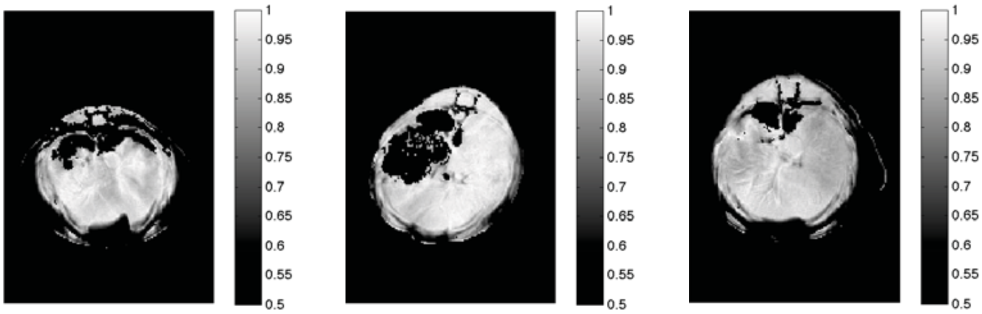

(a) Mouse no. 12. (b) Mouse no. 30. (c) Mouse no. 33.

Figure 4.54.: Calculated water fractions of a Black 6 (a), a Transgene (b) and a Wildtype mouse (c).

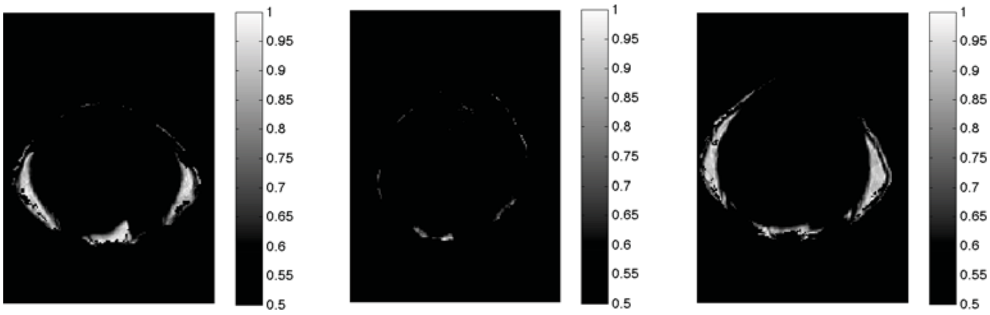

(a) Mouse no. 12. (b) Mouse no. 30. (c) Mouse no. 33.

Figure 4.55.: Calculated fat fractions of a Black 6 (a), a Transgene (b) and a Wildtype mouse (c).

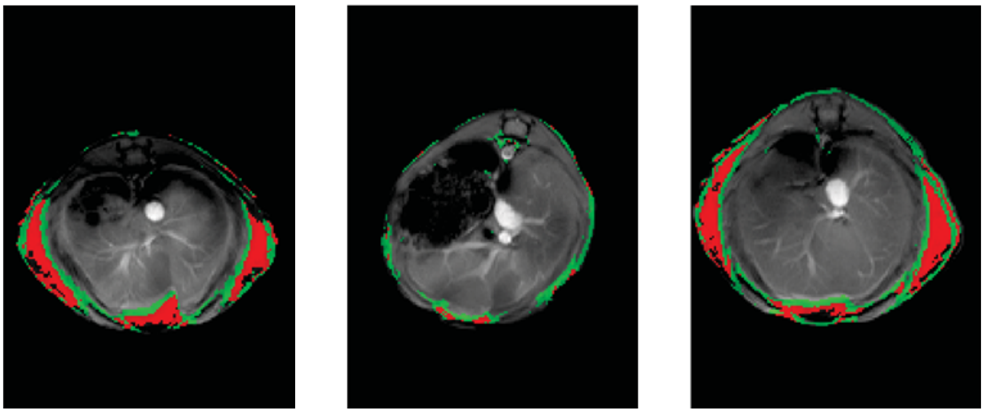

(a) Mouse no. 12.
(b) Mouse no. 30.
(c) Mouse no. 33.

Figure 4.56.: Calculated colored fat fractions of a Black 6 (a), a Transgene (b) and a Wildtype mouse (c). Some apparent BAT areas are caused by partial-volume artifacts.

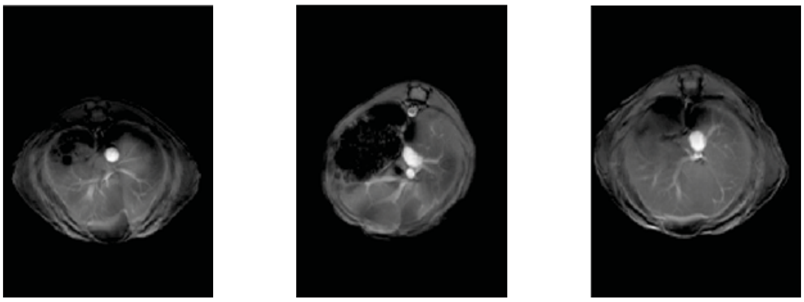

(a) Mouse no. 12.
(b) Mouse no. 30.
(c) Mouse no. 33.

Figure 4.57.: Calculated in-phase images of a Black 6 (a), a Transgene (b) and a Wildtype mouse (c).

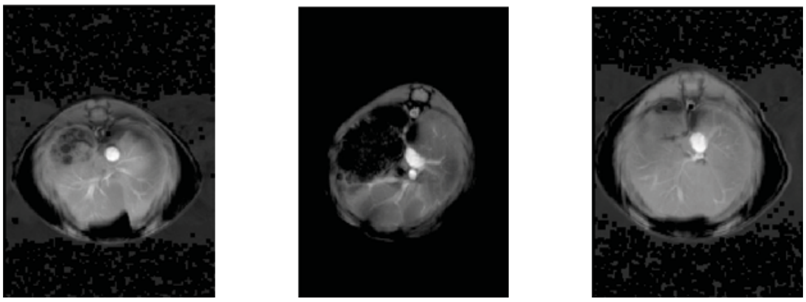

(a) Mouse no. 12.
(b) Mouse no. 30.
(c) Mouse no. 33.

Figure 4.58.: Calculated out-of-phase images of a Black 6 (a), a Transgene (b) and a Wildtype mouse (c).

4.3.4. 2 Week old Mouse with Additional TI Series

In this experiment a 2 week old mouse was scanned by using a STIR sequence with different inversion times (TI). The different longitudinal relaxation T1 of different tissues can be modelled by using this TI images.
For the BAT-WAT separation 10 slices were acquired in a axial orientation. Out of these 8 slice were used for the evaluation using the software tool. In the image series the different distribution of fat and water in the body is showed.

Table 4.10.: Significant STIR sequence parameters

Slices	10
Phase enc. dir.	A >>P
FoV read	28 mm
FoV phase	100%
Slice thickness	2,0 mm
TR	3000 ms
TE	12 ms
Averages	1
TI	50 ms |200 ms |400 ms |550 ms |700 ms |1000 ms
Flip angle	180 deg
Base resolution	128

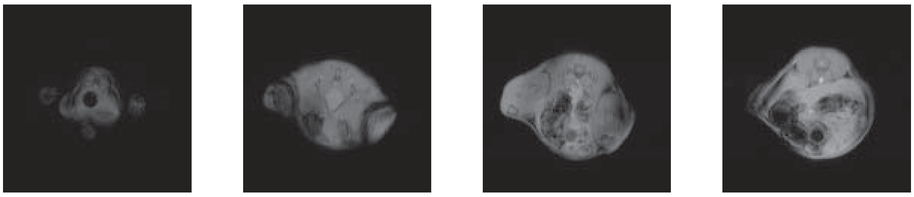

(a) Slice no. 1. (b) Slice no. 2. (c) Slice no. 3. (d) Slice no. 4.

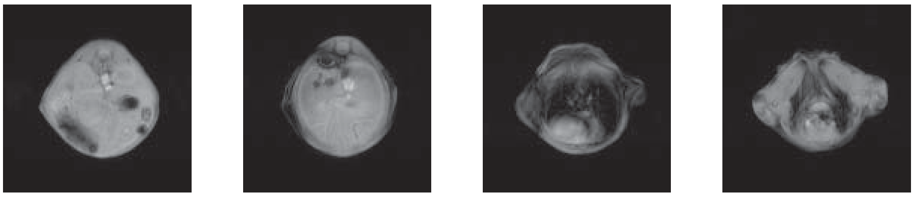

(e) Slice no. 5. (f) Slice no. 6. (g) Slice no. 7. (h) Slice no. 8.

Figure 4.59.: Magnitude images of a 2 week old mouse with 8 axial slices.

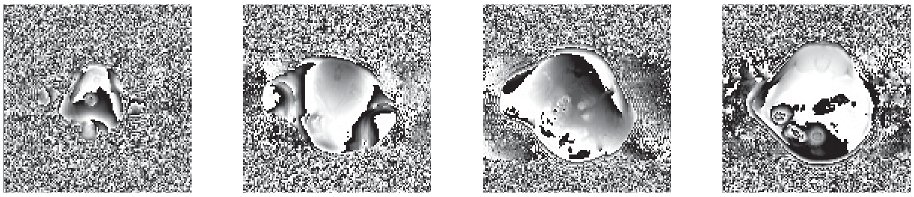

(a) Slice no. 1. (b) Slice no. 2. (c) Slice no. 3. (d) Slice no. 4.

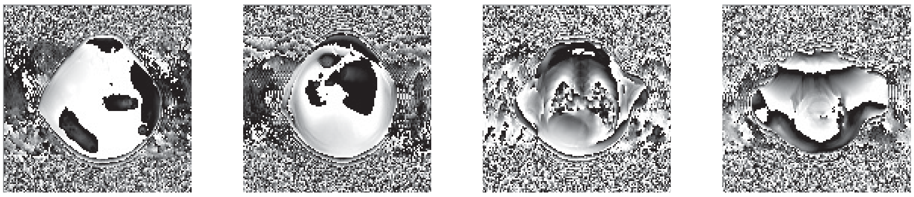

(e) Slice no. 5. (f) Slice no. 6. (g) Slice no. 7. (h) Slice no. 8.

Figure 4.60.: Phase images of a 2 week old mouse with 8 axial slices.

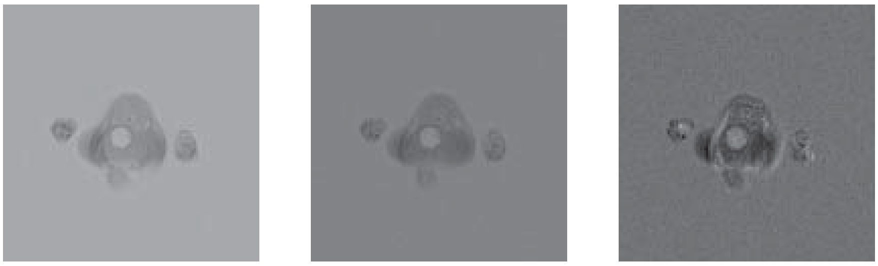

(a) TI = 50 ms. (b) TI = 200 ms. (c) TI = 400 ms.

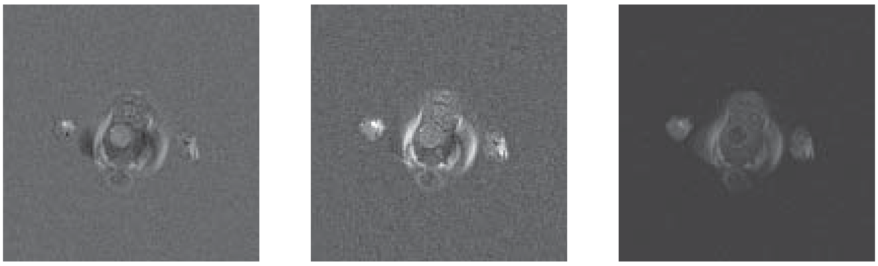

(d) TI = 550 ms. (e) TI = 700 ms. (f) TI = 1000 ms.

Figure 4.61.: TI variation images of a 2 week old mouse of slice no. 1.

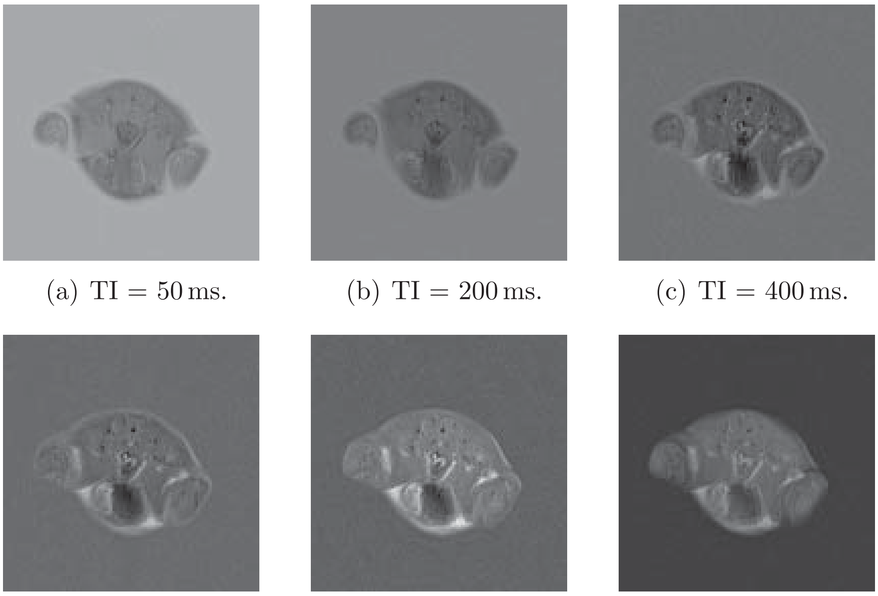

(a) TI = 50 ms. (b) TI = 200 ms. (c) TI = 400 ms.

(d) TI = 550 ms. (e) TI = 700 ms. (f) TI = 1000 ms.

Figure 4.62.: TI variation images of a 2 week old mouse of slice no. 2.

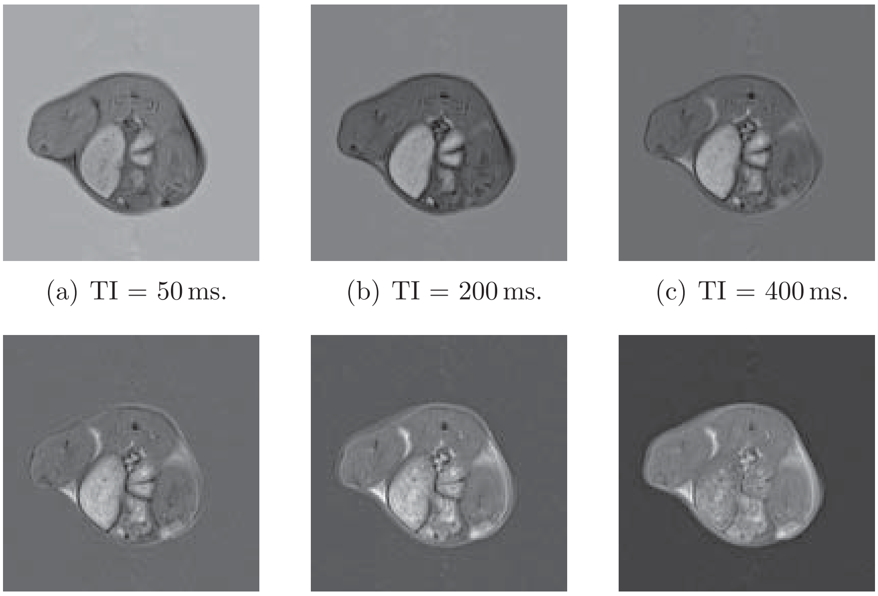

(a) TI = 50 ms. (b) TI = 200 ms. (c) TI = 400 ms.

(d) TI = 550 ms. (e) TI = 700 ms. (f) TI = 1000 ms.

Figure 4.63.: TI variation images of a 2 week old mouse of slice no. 3.

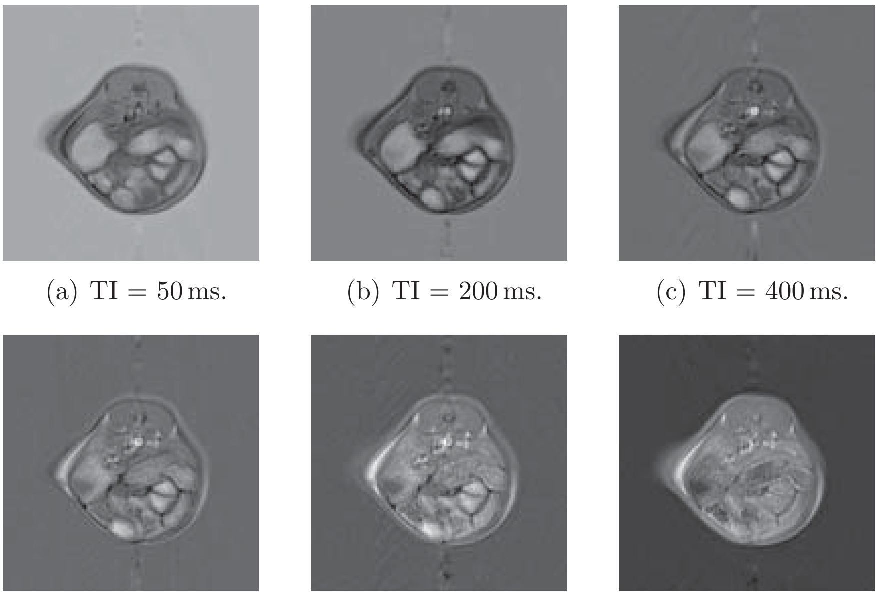

(a) TI = 50 ms. (b) TI = 200 ms. (c) TI = 400 ms.

(d) TI = 550 ms. (e) TI = 700 ms. (f) TI = 1000 ms.

Figure 4.64.: TI variation images of a 2 week old mouse of slice no. 4.

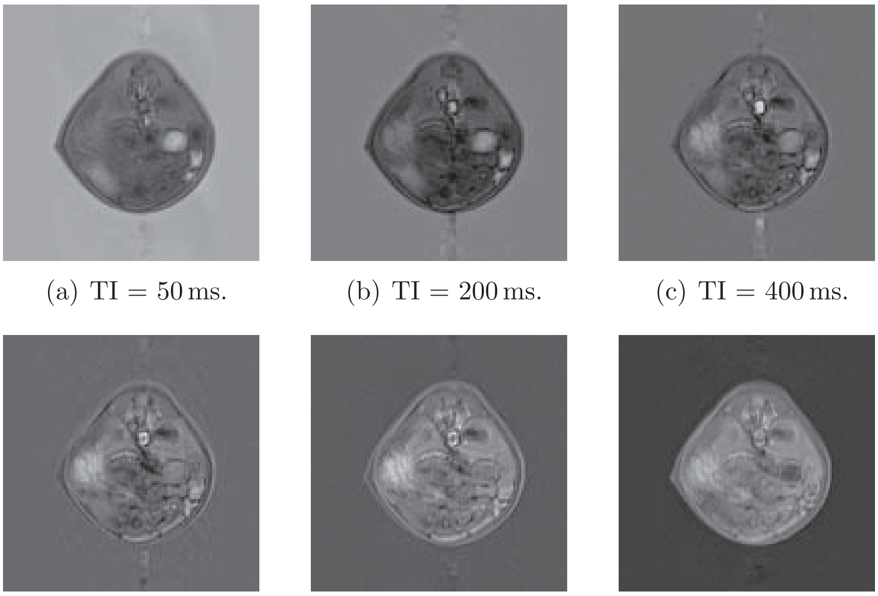

(a) TI = 50 ms. (b) TI = 200 ms. (c) TI = 400 ms.

(d) TI = 550 ms. (e) TI = 700 ms. (f) TI = 1000 ms.

Figure 4.65.: TI variation images of a 2 week old mouse of slice no. 5.

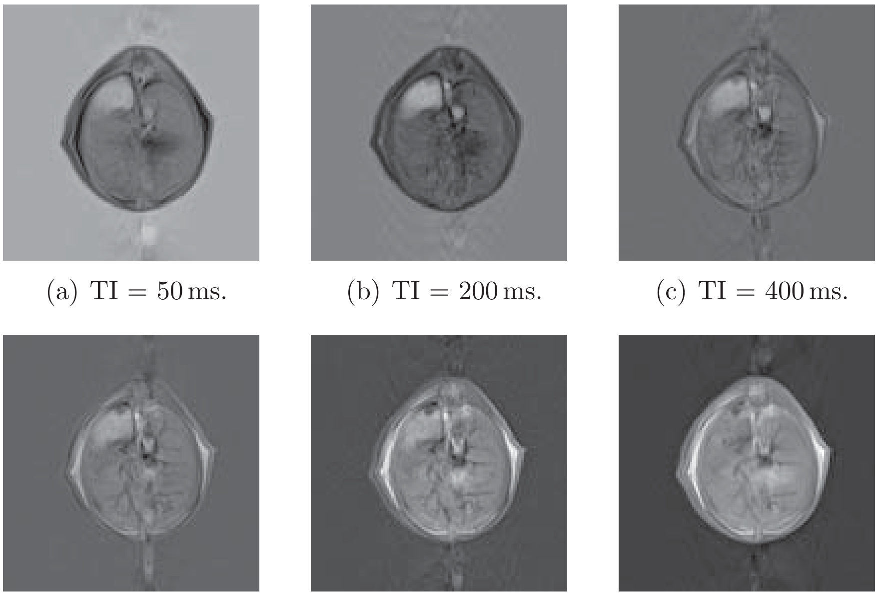

(a) TI = 50 ms. (b) TI = 200 ms. (c) TI = 400 ms.

(d) TI = 550 ms. (e) TI = 700 ms. (f) TI = 1000 ms.

Figure 4.66.: TI variation images of a 2 week old mouse of slice no. 6.

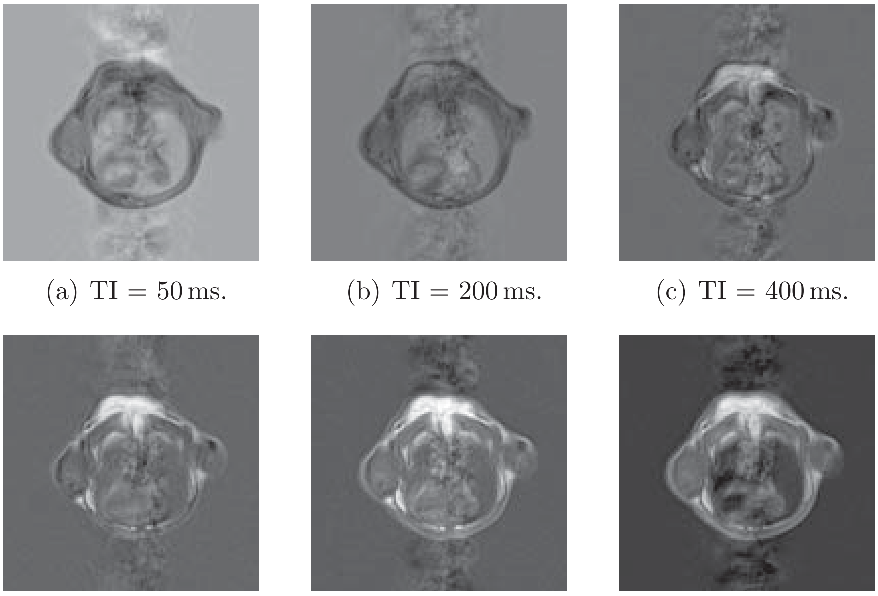

(a) TI = 50 ms. (b) TI = 200 ms. (c) TI = 400 ms.

(d) TI = 550 ms. (e) TI = 700 ms. (f) TI = 1000 ms.

Figure 4.67.: TI variation images of a 2 week old mouse of slice no. 7.

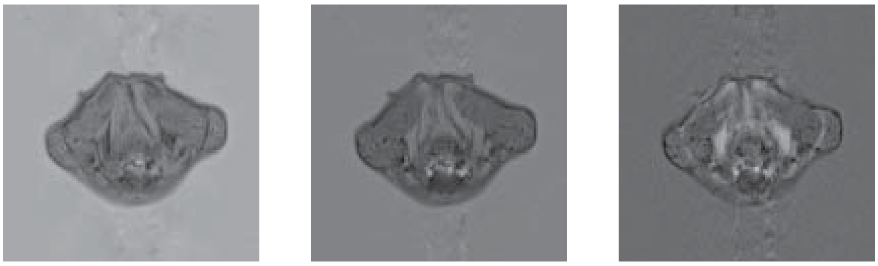

(a) TI = 50 ms. (b) TI = 200 ms. (c) TI = 400 ms.

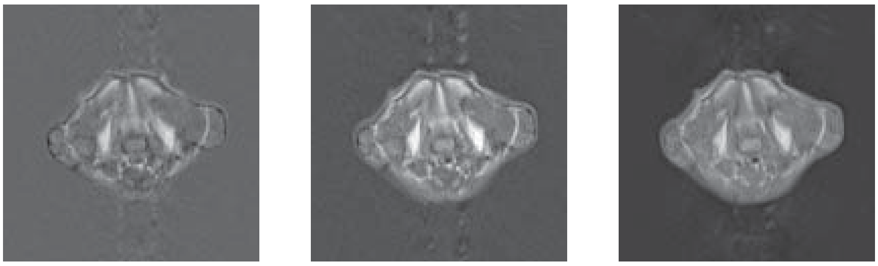

(d) TI = 550 ms. (e) TI = 700 ms. (f) TI = 1000 ms.

Figure 4.68.: TI variation images of a 2 week old mouse of slice no. 8.

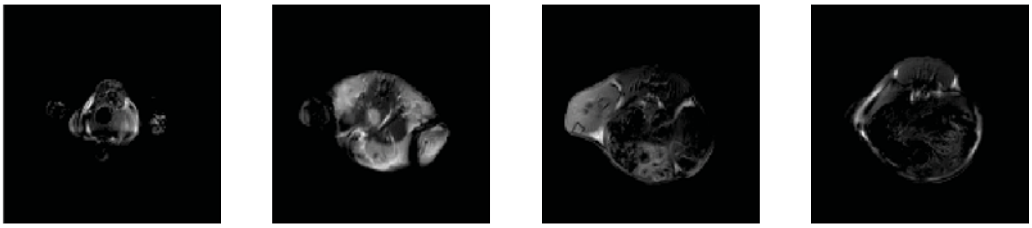

(a) Slice no. 1. (b) Slice no. 2. (c) Slice no. 3. (d) Slice no. 4.

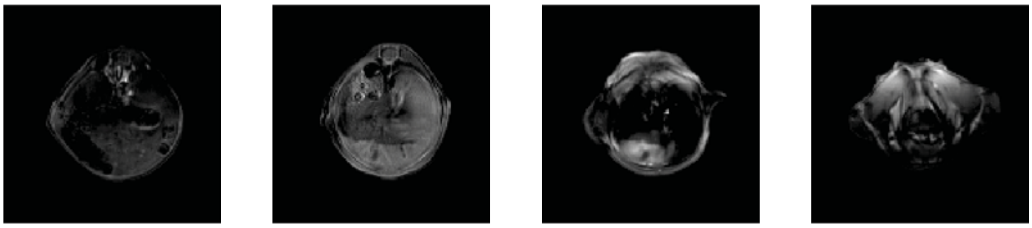

(e) Slice no. 5. (f) Slice no. 6. (g) Slice no. 7. (h) Slice no. 8.

Figure 4.69.: Fat images of a 2 week old mouse with 8 axial slices.

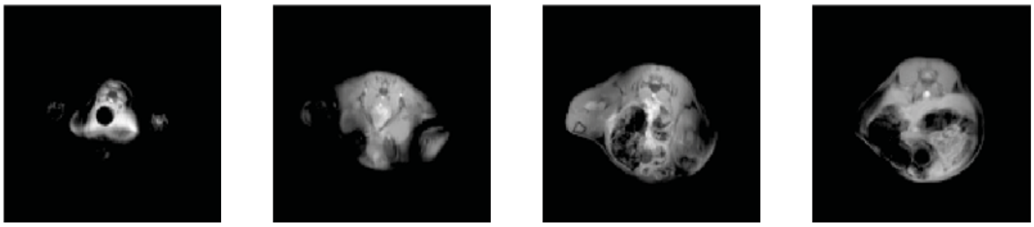

(a) Slice no. 1. (b) Slice no. 2. (c) Slice no. 3. (d) Slice no. 4.

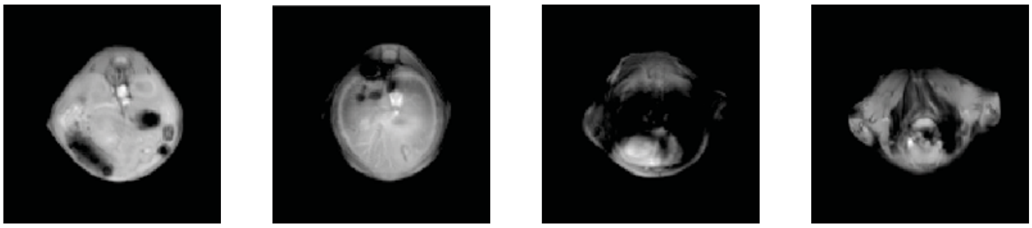

(e) Slice no. 5. (f) Slice no. 6. (g) Slice no. 7. (h) Slice no. 8.

Figure 4.70.: Water images of a 2 week old mouse with 8 axial slices.

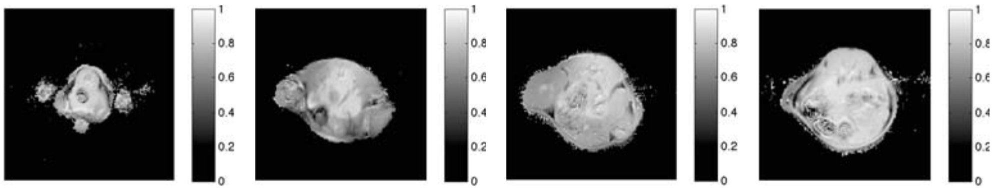

(a) Slice no. 1. (b) Slice no. 2. (c) Slice no. 3. (d) Slice no. 4.

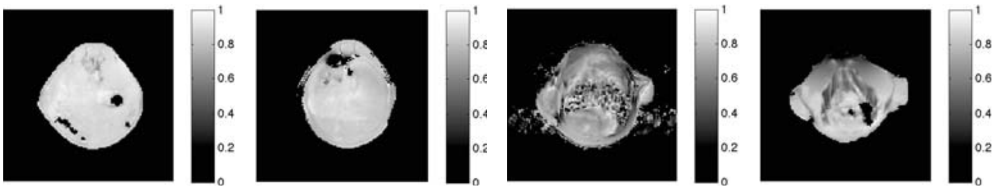

(e) Slice no. 5. (f) Slice no. 6. (g) Slice no. 7. (h) Slice no. 8.

Figure 4.71.: Water fraction of a 2 week old mouse with 8 axial slices.

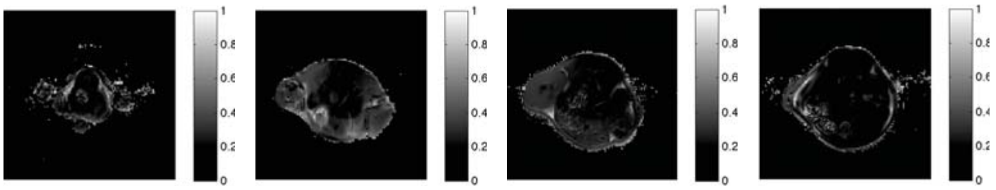

(a) Slice no. 1. (b) Slice no. 2. (c) Slice no. 3. (d) Slice no. 4.

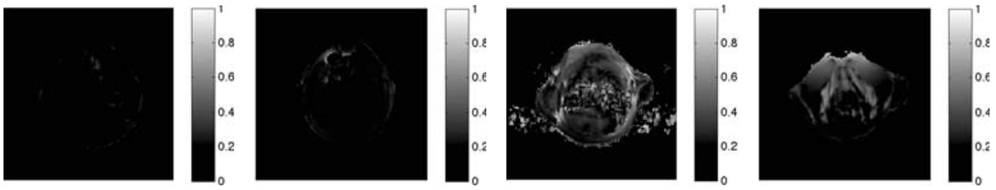

(e) Slice no. 5. (f) Slice no. 6. (g) Slice no. 7. (h) Slice no. 8.

Figure 4.72.: Fat fraction of a 2 week old mouse with 8 axial slices.

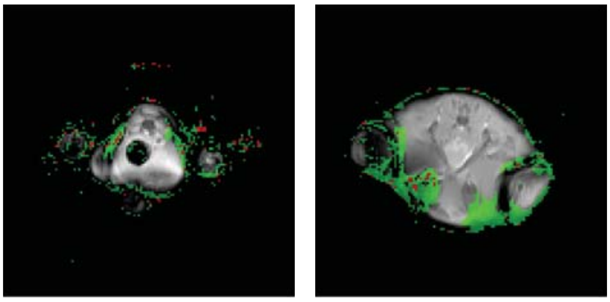

(a) Slice no. 1. (b) Slice no. 2.

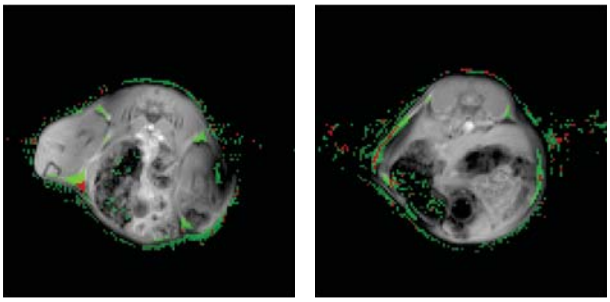

(c) Slice no. 3. (d) Slice no. 4.

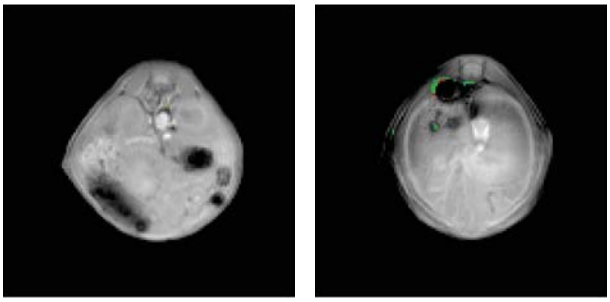

(e) Slice no. 5. (f) Slice no. 6.

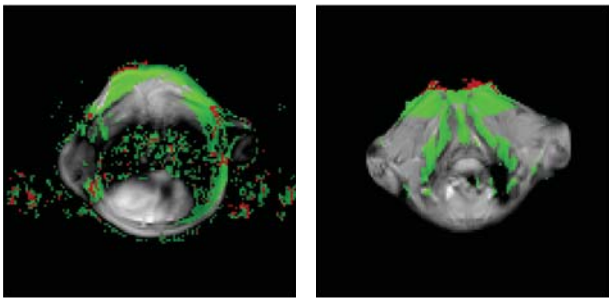

(g) Slice no. 7. (h) Slice no. 8.

Figure 4.73.: Colored fat fractions of a 2 week old mouse with 8 axial slices. In images (a) to (h) false BAT and WAT areas caused by partial-volume artifacts occurred.

5. Discussion and Conclusions

In this project we evaluated the feasibility of an MRI based method to separate brown- and white adipose tissue as described by Hu et al. [5]. The goal of this project was to design a work flow including imaging sequences to examine small animals and evaluate the adipose tissue (BAT and WAT) by using MRI. To reach this final goal a software tool was developed and different experiments using phantoms, animal and human tissue were realized.

The first step was to implement the IDEAL algorithm using a MATLAB script and to evaluate the algorithm. For the evaluation of the water-fat separation a simple water-oil phantom was used. The primary result of the IDEAL algorithm is the estimated B_0 field map image, a water image and a fat image. This first results are shown in figure 4.2. With the results of the algorithm the water fraction, the fat fraction and a colored fat fraction were calculated as shown in figure 4.3.

Further the in- and out of phase images were additionally calculated as shown in figure 4.4. These images provide additional information but are not primarily used for the BAT-WAT separation.

The whole work flow can be separated in two main tasks: image acquisition and the calculation of the separated water and fat images respectively the water and fat fraction. In the first step, the acquisition of magnitude and phase images, it is important to optimize the used sequences to get feasible images for the separation algorithm. This plays an important role in preclinical experiments because of the small volume of the animals and the limited scan time due to the anesthesia. The optimal choice of the echo spacing as described in section 3.1.1 is significant for a reliable BAT-WAT separation result.

The second task is the used method, in this case the IDEAL algorithm, to calculate a separate water and fat image as a base for the BAT-WAT separation. The right choice of the fat model (single or multifrequency) and the algorithm parameters (e.g. filter) is always a tradeoff between image quality and availability of input data. In order to obtain more input data, a higher number of scans is required. Each additional scan causes a proportional increase of the total scan time. In this project we chose a three point approach (single fat frequency) with images acquired at three different echo times.

5.1. Why using MRI to Detect BAT

One important question is, why should we use an MRI based method to detect BAT in human or animal tissue? Cypess et al. [2], van Marken Lichtenbelt et al. [4] and Virtanen et al. [22] used PET-CT in their works to detect active BAT in the human body. A major disadvantage of PET-CT is that only active BAT can be detected e.g. after cold exposure of the patient. BAT can also be found in an inactive state e.g. when there is no thermogenic activation needed. To detect active and inactive BAT a method based on MRI can be used as shown in the works of Hu et al. [5, 6]. This method is based on a water-fat separation by using an IDEAL algorithm as described in section 3.2.2. Beside the advantage of detecting active and inactive BAT there is no need for an x-ray exposure of the patients which is a huge advantage for designing different clinical trials. Another advantage of MRI compared to PET-CT are the lower costs per examination which play an essential role in large-scale trials.

As described the focus of the research group in Graz is the preclinical imaging of small animals e.g. mice or rats. To examine such small animals special MR equipment is available to acquire images with good SNR and contrast behavior. This has led to a great interest in the described MRI based method to detect BAT.

A full work flow for animal examinations and image evaluation would be a useful tool for adipose tissue research groups. This would provide additional image based informations of the BAT and WAT distribution in the examined body.

According to the first results described by Hu et al. [5, 6] and the results of the realized experiments in this project, MRI is a valid technique to evaluate adipose tissue. The described method based on the IDEAL algorithm leads to good results but still has potential for improvements. More precise informations about the different fat frequency peaks could lead to a better differentiation of BAT and WAT. This could be used for a multipoint IDEAL model. A possible solution would be the combination of a single voxel spectroscopy with the IDEAL GRE sequences. The described MR differences of BAT and WAT as provided in the work of Hamilton et al. [7] could be used for a novel approach to improve the BAT-WAT separation by using MRI. In this work the known fat fraction differences and marginal T1 and T2 differences between BAT and WAT were discussed. The described differences of the inversion recovery behavior was used to develop an approach to improve the BAT-WAT separation.

For this purpose measurements of a mouse with different inversion times were made as shown in figures 4.61, 4.62, 4.63, 4.64, 4.65, 4.66, 4.67 and 4.68. The idea was to use these additional images to weight the fat and water fraction calculated using the IDEAL algorithm. The experiments with the additional weighting did not lead to improved separation results as supposed.

The problem was, that only the water peak of BAT and WAT shows a different inversion behavior but not the whole BAT and WAT tissue as shown in the images acquired by using a STIR sequence. A second approach to improve the BAT-WAT separation is to combine the inversion time directly with the GRE sequence for the IDEAL algorithm. This would lead to a water image with suppressed water of BAT respectively WAT. The huge disadvantage of this approach is the enormous lengthening of the scan time which was the reason why we did no further experiments with this sequence. For animal or human examinations the total scan time would be far beyond a tolerable scan time.

5.2. Comparison of Different Parameter Settings

With the evaluated algorithm the phantom images were used to optimize the parameters and to evaluate a multipoint approach. For this multipoint approach images were acquired at six different echo times as described in section 4.1. With this additional image information the fat can be modeled by using more than one frequency. Starting with the three point approach, an additional fat frequency was modeled in each step. As a result we received a separate fat image for each frequency peak which in the end were combined into a single fat image. The following frequencies were used f_p = -431 Hz |-329 Hz |-483 Hz |-245 Hz in this experiment to model the fat component. The side frequencies were calculated relative to the main fat frequency (-431 Hz) of the 3 T MR system of the Department of Radiology, University Hospital LKH Graz. For the calculation of the side fat peaks, frequency shift values based on the work of Reeder et al. [12] were used.

Using this modified algorithm all previous described images (field map, water, fat, water fraction, fat fraction, colored fat fraction, in-phase and out of-phase image) were computed and compared. In the B_0 field map images (figure 4.5) and in the water images (figure 4.6) no significant differences were found by using two fat frequencies compared to the results of the basic model with only one fat frequency. The model with two fat frequencies result in a slightly poorer fat image as shown in figure 4.7.

As a consequence of the bad fat estimation all further calculations lead to false results. This can be seen in figure 4.8 for the water fraction and in figure 4.9 for the fat fraction. As shown in figures 4.10 and 4.11 the in- and out-of-phase images are affected as well due to the bad fat estimation. Using more than two frequencies to model the fat leads to unusable images in our experiments.

A possible explanation for the bad results could be that the shifts between the fat peaks are different to the values given in the work of Reeder. Another reason could be that the amplitudes of the side peaks were covered by the noise or the water peak.

Based on these results and the consideration of the scan time we chose the three point approach for all further experiments in this project.

Using these phantom images the impact of different parameter settings on the estimation result was evaluated. A good indicator for the correct parameter setting is that the number of iterations. If the algorithm minimizes the ΔB_0 error to a value lower than 1 Hz in less than 40 iterations it is a good sign that the parameters were chosen correctly. At different experiments with wrong images or parameters a ΔB_0 error lower than 1 Hz was not achieved within 200 iterations.

Not only the selected parameters affect the ΔB_0 error and the number of iterations but also a suboptimal choice of echo times can lead to a higher error value. To avoid too long computing times, computation is aborted after 40 iterations. In the preclinical and human experiments provided in this report this case was never observed and the ΔB_0 error was always lower than 1 Hz after 3-10 iterations.

Experimental images of a milk phantom were acquired without usable results. The fat content of 3,5% of the milk was too low for the detection using the IDEAL algorithm. The resulting images are not provided in this report.

With the presented experimental set-up and the implemented evaluation tool further phantom measurements can be made using different materials containing fat e.g. mayonnaise to evaluate the lowest detectable fat content. The phantom set-up can also be used to exam and evaluate excised tissue samples.

5.3. Evaluation of Human Images

Besides the main goal to establish a preclinical work flow, the usage of the IDEAL algorithm in combination with human images was evaluated. A novel work of Hu et al. [6] showed the usability of the IDEAL approach for examination of human infants. In this work post mortem scans were made using MRI and CT. Because of ethical concerns no measurements with human infants were made in this project. Such studies with human infants would require a long planning time and a reasonable research question beside the BAT-WAT localization.

Instead, images of a human knee were acquired using two different MR systems (3 T and 1,5 T). With these images the primary water-fat separation was demonstrated.

The amount of BAT in adult humans is about 0,05-0,1% of the total body weight and is only prevalent in less than 10% of human adults. [17]

These facts made it very difficult to detect BAT in adult humans because a huge group of test persons is needed to be able to obtain a significant result. This issue still remains a challenge for the future to design of clinical trials on the examination of the prevalence of BAT ind adult humans. In the work of Cypess et al. [2] images of 1972 different patients acquired by using PET-CT were evaluated to detect BAT. To exam a similar number of patients a lot of scan time is required because the three point IDEAL algorithm uses images acquired at three different echo times. With a rising number of slices and a higher FoV the scan time is increasing significantly for all three repetitions of the sequence.

The acquired human images were used to evaluate the IDEAL water-fat separation for future human experiments. Beside the detection of BAT this algorithm and software tool can be used to separate water and fat in images for different research questions. In this experiment images of a human knee with three slices were acquired in a sagittal orientation. In figure 4.13 the three different magnitude images are shown. The corresponding phase images are shown in figure 4.14. The estimated B_0 field map images of all three slices are shown in figure 4.15.
The water images and fat images as result of the IDEAL algorithm are shown in figure 4.16 and figure 4.17. In these images the different water and fat content of the tissues can be seen very clearly. The bone tissue leads to no signal in the water image and to a detectable signal in the fat image. Respectively the muscle tissue leads to a strong water signal and to very low fat signal. These differences were emphasized by calculating the water and fat fraction images as shown in figure 4.18 and figure 4.17. The additional in- and out-of-phase images are shown in figures 4.21 and 4.22.

In a second experiment images of a human abdomen, acquired in axial orientation were evaluated. In figure 4.23 the acquired magnitude and phase images of the first echo are shown. The acquired slice was located in the liver region to evaluate fat depots in the liver region. The calculated fat images provided a strong signal from the subcutaneous fat and from an intra abdominal fat depot. Comparing the fat image and the fat fraction some structures e.g. the fat capsule of the kidneys lead to a strong signal only in the fat fraction image as shown in figure 4.25. This effect is even stronger when a colormap is used (figure 4.26 and figure 4.27) This images should show the possible usage of the software tool besides the detection of BAT. Without a water and fat separation it is possible that some structures can be obscured by other tissue which will lead to a wrong clinical diagnosis.

To show the usability of the IDEAL algorithm and the software tool for evaluation of images acquired at a different field strength the same patient was scanned by using a 1,5 T MR system. The acquired magnitude and phase images of the human knee are shown in figure 4.28. The estimated B_0 filed map and the calculated water- and fat images are shown in figure 4.29. Comparing the resulting fat and water fraction images in figure 4.31 with the results of the scan at the 3 T MR system, a slightly poorer result was achieved at the 1,5 T MR system.
Another interesting issue would be the results of animal scans at 1,5 T. The conduction of this scans was not possible due to the lack of a preclinical imaging infrastructure at

the 1,5 T MR system.

For the separation of BAT and WAT the fat fraction is colored using green for BAT and red for WAT as described in section 3.3.2. A wide fat fraction range of BAT, 40-80%, was reported in different works e.g. Hu et al. [5]. Artifacts in the calculated water and fat fraction caused by different B_0 inhomogeneities or partial-volume effects lead to areas with a lower fat fraction which are colored green and detected as BAT. Figures 4.20, 4.25 and 4.31 show the colored fat fractions of the human knee and abdomen. In these images different sized areas are marked as BAT (green) e.g. at the patella in figure 4.31 which is an artifact and no correct anatomical information. It is important to know the common BAT depots in humans and rodents to evaluate the images and to identify false positive BAT areas.

5.4. Evaluation of Preclinical Images

One great challenge in preclinical imaging is to get useful images of the whole animal e.g. a mouse. For the animal examinations a $1H$ Transmit / Receive Volume Coil was used as described in section 3.1 to provide a good SNR behavior.

In the first animal experiments a 2 week old mouse was scanned with a GRE and a STIR sequence. The acquired magnitude and phase images using the GRE sequence are shown in figure 4.32. In the estimated B_0 field map image a large inhomogeneous area is found in the cervical region. This area causes errors in the calculation of the water and fat images as shown in figure 4.33.

Using the *recalculate fat fraction* function the effect of this inhomogeneous area can be minimized by choosing a new maximum fat value. The result of this recalculation is shown in figure 4.34.

In the colored fat fraction image the BAT and WAT depots located in the neck are clearly separated. In the calculated out-of-phase image (see figure 4.35) the fat depot can be separated from the surrounding tissue. A clear differentiation between BAT and WAT in these images is not possible.

In the additional acquired images using a STIR sequence with two different inversion times the cervical fat depot and the fat depot in the throat region can be detected (see figure 4.36). The throat fat depot in the IDEAL images was suppressed by the B_0 field inhomogeneity.

5.5. The Importance of Color

Comparing the same results by using different colormaps should demonstrate the importance of additional color information for the quantification of adipose tissue. The calculated B_0 field map (figure 4.37), the water image (figure 4.38), the fat image (figure

4.39), the water fraction (figure 4.40) and the fat fraction 4.41) of a 2 week old mouse were compared using the colormaps gray (standard), jet and hot. The highest improvement using a colormap (e.g. jet or hot) can be seen in the water and fat fraction images. This is a huge advantage for the separation of BAT and WAT in the images. In this experiment no fat fraction correction was made to demonstrate the difference between corrected (figure 4.34) and uncorrected (figure 4.40 and figure 4.41) images.
The idea to separate BAT and WAT using different colors led to the colored fat fraction as described in section 3.3.2. The idea was to color BAT as green and WAT as red according to the fat fraction and combine it with a magnitude image. It is important to set the BAT/WAT threshold and the maximum fat value correctly, in order to be able to get significant results in the colored fat fraction. As earlier described a critical interpretation of the result is important.

5.6. The right Choice of Echoes

A 36 week old mouse was scanned with a GRE sequence at six different echo times. For the image calculations the fat was modeled with one fat peak at -431 Hz. In the case of a water and fat separation with one fat frequency three images are required to determine the B_0 field map, the water image and the fat image. Every additional image acquired at a different echo time leads to more (additional) information. By using more than three images the IDEAL algorithm leads to a better estimation result.
At this experiment the same problem with a strong inhomogeneous area in the throat region occurred. Using the same fat model and algorithm with six images leads to smoother images compared with the images calculated using three echoes and three asymmetric echoes. This effect can be seen in the fat image in figure 4.44.
The inhomogeneous area obscures again the fat depot in the neck region as shown in figures 4.44 and 4.46. The fat depot in the neck is visible again in the STIR images acquired at different inversion times as shown in figure 4.48.

In this experiment the IDEAL algorithm failed because of the high B_0 field inhomogeneities in the throat region. A fat fraction recalculation in the GUI was providing no improvement. This inhomogeneity causes wrong pixel values in the fat fraction which lead to a wrong colored fat fraction as shown in figure 4.47.

The right choice of echoes is also connected with the noise performance as described by Reeder et al. [10]. If the echo times are chosen as described in section 3.1.1 the best possible noise performance is reached. The optimal parameters depend on the used sequence for the image acquisition. For all experiments in this project the parameters were chosen to reach the optimal echo spacing.

5.7. Different Mouse Type Different Fat Distribution?

Using images acquired in a different study the fat content of three different mouse types was evaluated. The acquired magnitude and phase images are shown in figure 4.49 and figure 4.50. In the B_0 field map images weak inhomogeneities occur in the liver area as shown in figure 4.51.

The significant lower fat in the tumor mouse is clearly shown in the fat image (figure 4.53) and in the fat fraction (figure 4.55). Mouse no. 12 and mouse no. 33 have a higher subcutaneous fat in the abdomen area compared with mouse no. 30. This loss of fat is called cancer-associated cachexia and described in the work of Das et al. [23]. As described above the out-of-phase images in figure 4.58 provide additional information about the fat depot. Compared to the water- and fat fraction images of mouse no. 30 the liver tumor is visible in the in- and out-of-phase images as shown in figure 4.57 and figure 4.58.

An interesting research question that arises from this experiment is to evaluate if there is a different amount of BAT in a mouse with a cancer-associated cachexia compared to a normal mouse of the same type.

5.8. Inversion Time Behaviour

The different inversion behavior of BAT and WAT as shown in figure 2.11 is described in the work of Hamilton et al. [7]. To evaluate the feasibility by using this reported difference to develop an approach to separate BAT and WAT an image series with different inversion times was acquired. 10 slices of a 2 week old mouse were acquired in an axial direction to cover the whole body of the mouse. The parameters of the used STIR sequence are listed in table 4.10. The acquired magnitude and phase images as used for the IDEAL algorithm are shown in figure 4.59 and figure 4.60.

The images acquired at six different echo times were compared for each slice in figures 4.61, 4.62, 4.63, 4.64, 4.65, 4.66, 4.67 and 4.68. In this image series with different inversion times the contrast difference of the tissues can be seen very clearly. This behavior can be used for the water and fat separation as described in section 2.3.3. Using this behavior a approach to improve the BAT-WAT separation was developed as discussed in section 5.1. The results of the IDEAL algorithm for three echoes are shown in figure 4.70 (water image), figure 4.69 (fat image), figure 4.71 (water fraction) and figure 4.72 (fat fraction). The colored map of the fat fraction (figure 4.73) shows the BAT depot in the neck of the mouse in slice no. 7 and no. 8. Compared to the mouse no. 12 and no. 33 no significant subcutaneous WAT depot was found. The inversion time images can be used to enhance the contrast between different tissues by selecting a specific inversion time. With a specific inversion time related to the tissue the signal of the chosen tissue can be suppressed and the signal of a second tissue can be enhanced.

5.9. Artifacts and Inhomogeneities

B_0 field inhomogeneities and partial volume artifacts can lead to false water and fat pixel values in the images. These effects often occur in areas with boundaries between different tissues. Such false pixel values lead to false positive BAT and WAT values in the calculated colored fat fraction map. In the acquired images of a human kee this partial volume effect can be seen clearly. (see figure 4.20) Because of the wide BAT range (40-80% fat fraction) this effect can lead to large areas with false BAT pixel values.
It is implausible that the green marked areas in the knee images are real BAT. The BAT and WAT separation process based on the fat fraction values can not eliminate these partial volume effects and will lead to false positive BAT or WAT maps. This partial volume effect can also occur in areas close to actual BAT depots as seen in figure 4.34.

Beside the partial volume effect, B_0 inhomogeneities can also lead to false pixel values in the images. In areas with strong inhomogeneities as seen in figure 4.42 the B0 field correction of the IDEAL algorithm failed. This high inhomogeneities lead to false fat pixel values in the areas where these inhomogeneities occur. (see figure 4.44) To avoid this it is possible to exclude this areas with a smaller FoV or to recalculate the fat fraction with a new maximal fat pixel value by using the developed software tool.

5.10. Conclusions

The conclusion of this project is that the used method based on MRI to detect BAT and separate it from WAT and other tissue is feasible and can be used for animal research. The described method is also applicable to separate water and fat in human images. The differentiation of BAT and WAT using the calculated fat fraction is currently the only feasible method based on MRI. Although it is important to combine the result of the fat fraction with the anatomical information of the examined subject (e.g. mouse or human) to evaluate the images. Sometimes artifacts (e.g. partial volume effects) or inhomogeneities lead to fat fraction values in the range of the BAT. This wide BAT range is another crucial point for the detection of BAT in the body.
The adipose tissue research is a rapidly growing field and of great potential. Image information can be used as control-tool for adipose tissue research e.g. to evaluate the effect of cold exposure. A second possible application is the evaluation of the transdifferentiation of BAT to WAT respectively WAT to BAT. This tissue transdifferentiation could play a key role in future obesity or diabetes treatment.
To improve the separation results of the MRI based method or to develop a new detection method, a precise determination of the MR properties of BAT and WAT is required. Using faster imaging sequences the multipoint IDEAL algorithm in combination with a more

accurate BAT spectrum can lead to more accurate separation results. It is important to consider the SNR behavior because the amplitudes of the side fat peaks can be very low. Another possible future use of this work including the software tool is to separate more than two different species in the images. It is possible to separate materials with a different frequency spectrum e.g. water, fat and silicon. Summarizing the findings of the project, MRI is a powerful and feasible method to detect BAT and separate it from other tissue. This MRI based method has still potential for improvements specially for preclinical experiments. An interesting goal for future research would be the detection of BAT in the adult human by using an MRI based method.

Bibliography

[1] Yu-Hua Tseng, Aaron M Cypess, and C Ronald Kahn. Cellular bioenergetics as a target for obesity therapy. *Nature reviews. Drug discovery*, 9(6):465–82, June 2010.

[2] Aaron M Cypess, Sanaz Lehman, Gethin Williams, Ilan Tal, Dean Rodman, Allison B Goldfine, Frank C Kuo, Edwin L Palmer, Yu-Hua Tseng, Alessandro Doria, Gerald M Kolodny, and C Ronald Kahn. Identification and importance of brown adipose tissue in adult humans. *The New England journal of medicine*, 360(15):1509–17, April 2009.

[3] S Cinti. Between brown and white: novel aspects of adipocyte differentiation. *Ann Med*, 43(2):104–115, Mar 2011.

[4] Wouter D van Marken Lichtenbelt, Joost W Vanhommerig, Nanda M Smulders, Jamie M a F L Drossaerts, Gerrit J Kemerink, Nicole D Bouvy, Patrick Schrauwen, and G J Jaap Teule. Cold-activated brown adipose tissue in healthy men. *The New England journal of medicine*, 360(15):1500–8, April 2009.

[5] H H Hu, D L Smith, K S Nayak, M I Goran, and T R Nagy. Identification of brown adipose tissue in mice with fat-water ideal-mri. *J Magn Reson Imaging*, 31(5):1195–1202, May 2010.

[6] Houchun H Hu, Jason P Tovar, Zdena Pavlova, Michelle L Smith, and Vicente Gilsanz. Unequivocal identification of brown adipose tissue in a human infant. *Journal of magnetic resonance imaging : JMRI*, 000:1–5, December 2011.

[7] Gavin Hamilton, Daniel L. Smith, Mark Bydder, Krishna S. Nayak, and Houchun H. Hu. MR properties of brown and white adipose tissues. *Journal of Magnetic Resonance Imaging*, 34(2):468–473, August 2011.

[8] *Wie funktioniert MRI?* Springer, 2009.

[9] Thorsten a Bley, Oliver Wieben, Christopher J François, Jean H Brittain, and Scott B Reeder. Fat and water magnetic resonance imaging. *Journal of magnetic resonance imaging : JMRI*, 31(1):4–18, January 2010.

[10] Scott B Reeder, Charles a McKenzie, Angel R Pineda, Huanzhou Yu, Ann Shimakawa, Anja C Brau, Brian a Hargreaves, Garry E Gold, and Jean H Brittain.

Water-fat separation with IDEAL gradient-echo imaging. *Journal of magnetic resonance imaging : JMRI*, 25(3):644–52, March 2007.

[11] Scott B Reeder, Zhifei Wen, Huanzhou Yu, Angel R Pineda, Garry E Gold, Michael Markl, and Norbert J Pelc. Multicoil Dixon chemical species separation with an iterative least-squares estimation method. *Magnetic Resonance in Medicine*, 51(1):35–45, 2004.

[12] Huanzhou Yu, Ann Shimakawa, Charles a McKenzie, Ethan Brodsky, Jean H Brittain, and Scott B Reeder. Multiecho water-fat separation and simultaneous R2* estimation with multifrequency fat spectrum modeling. *Magnetic resonance in medicine : official journal of the Society of Magnetic Resonance in Medicine / Society of Magnetic Resonance in Medicine*, 60(5):1122–34, November 2008.

[13] Scott B Reeder, Angel R Pineda, Zhifei Wen, Ann Shimakawa, Huanzhou Yu, Jean H Brittain, Garry E Gold, Christopher H Beaulieu, and Norbert J Pelc. Iterative decomposition of water and fat with echo asymmetry and least-squares estimation (IDEAL): application with fast spin-echo imaging. *Magnetic Resonance in Medicine*, 54(3):636–644, 2005.

[14] Stephane Gesta, Yu-Hua Tseng, and C Ronald Kahn. Developmental origin of fat: tracking obesity to its source. *Cell*, 131(2):242–56, October 2007.

[15] Sarah L Henry, Jonathan G Bensley, Ryan J Wood-Bradley, Luise a Cullen-McEwen, John F Bertram, and James a Armitage. White adipocytes: More than just fat depots. *The international journal of biochemistry & cell biology*, pages 1–6, December 2011.

[16] E Lunati, P Marzola, E Nicolato, M Fedrigo, M Villa, and a Sbarbati. In vivo quantitative lipidic map of brown adipose tissue by chemical shift imaging at 4.7 Tesla. *Journal of lipid research*, 40(8):1395–400, August 1999.

[17] Sven Enerbäck. Human brown adipose tissue. *Cell metabolism*, 11(4):248–52, April 2010.

[18] Dixon WT. Simple proton spectroscopic imaging. *Radiology*, 1984.

[19] a Sbarbati, U Guerrini, P Marzola, R Asperio, and F Osculati. Chemical shift imaging at 4.7 tesla of brown adipose tissue. *Journal of lipid research*, 38(2):343–7, February 1997.

[20] Jimin Ren, Ivan Dimitrov, a Dean Sherry, and Craig R Malloy. Composition of adipose tissue and marrow fat in humans by 1H NMR at 7 Tesla. *Journal of lipid research*, 49(9):2055–62, September 2008.

[21] *Bildgebende Verfahren in der Medizin.* Springer, 2000.

[22] K.A. Virtanen, M.E. Lidell, J. Orava, M. Heglind, R. Westergren, T. Niemi, Markku Taittonen, Jukka Laine, N.J. Savisto, S. Enerb\\"ack, and Others. Functional Brown Adipose Tissue in Healthy Adults. *New England Journal of Medicine*, 360(15):1518–1525, 2009.

[23] SK Das, S Eder, S Schauer, C Diwoky, and H Temmel. Adipose Triglyceride Lipase Contributes to Cancer-Associated Cachexia. *Science*, 233(2011), 2011.

List of Figures

List of Tables

A. Appendix

A.1. IDEAL Algorithm Equations

In this section the full equations of the IDEAL algorithm for N echoes and M species is described.
For n = 1,...,N number of echoes following equations can be written in matrix form.

$$\hat{\mathbf{S}} = A\rho \tag{A.1}$$

$$\hat{\mathbf{S}} = \begin{bmatrix} \hat{S}_1^R & \hat{S}_1^R & ... & \hat{S}_N^R & \hat{S}_1^I & \hat{S}_1^I & ... & \hat{S}_N^I \end{bmatrix}^T \tag{A.2}$$

$$\rho = \begin{bmatrix} \rho_1^R & \rho_1^I & \rho_2^R & \rho_1^I & ... & \rho_M^R & \rho_M^I \end{bmatrix}^T \tag{A.3}$$

$$A = \begin{bmatrix} c_{11} & -d_{11} & c_{21} & -d_{21} & ... & c_{M1} & -d_{M1} \\ c_{12} & -d_{12} & c_{22} & -d_{22} & ... & c_{M2} & -d_{M2} \\ ... & ... & ... & ... & ... & ... & ... \\ c_{1N} & -d_{1N} & c_{2N} & -d_{2N} & ... & c_{MN} & -d_{MN} \\ d_{11} & c_{11} & d_{21} & c_{21} & ... & d_{M1} & c_{M1} \\ d_{12} & c_{12} & d_{22} & c_{22} & ... & d_{M2} & c_{M2} \\ ... & ... & ... & ... & ... & ... & ... \\ d_{1N} & c_{1N} & d_{2N} & c_{2N} & ... & d_{MN} & c_{MN} \end{bmatrix} \tag{A.4}$$

Using a least-squares fitting approach for linear systems of equations following equation can be used to determine the initial estimates of each chemical species.

$$\hat{\rho} = (A^T A)^{-1} A^T \hat{S} \tag{A.5}$$

$$\hat{\rho} = \begin{bmatrix} \hat{\rho}_1^R & \hat{\rho}_1^I & \hat{\rho}_2^R & \hat{\rho}_2^I & ... & \hat{\rho}_M^R & \hat{\rho}_M^I \end{bmatrix}^T \tag{A.6}$$

After the calculation of the first estimation following equations can be used to calculate the errors of the field map an the chemical species.

$$\rho_j^R = \hat{\rho}_j^R + \Delta\rho_j^R \tag{A.7}$$

$$\rho_j^I = \hat{\rho}_j^I + \Delta\rho_j^I \tag{A.8}$$

With j = 1,...M and $\psi = \psi_0 + \Delta\psi$

$$s_n \approx \Big(\sum_{j=1}^{M}(\hat{\rho}_j + \Delta\rho_j)e^{i2\pi\Delta f_j t_n}e^{i2\pi\Delta\psi t_n}\Big) \tag{A.9}$$

$$\hat{S}_n^R + i\hat{S}_n^I = \Big(\sum_{j=1}^{M}(\hat{\rho}_j^R + \Delta\rho_j^R + i(\hat{\rho}_j^I + \Delta\rho_j^I))(c_{jn} + id_{jn})\Big)(1 + i2\pi\Delta\psi t_n) \tag{A.10}$$

$$\hat{\hat{S}}_n^R = \hat{S}_n^R - \sum_{j=1}^{M}(\hat{\rho}_j^R c_{jn} - \hat{\rho}_j^I d_{jn}) = 2\pi\Delta\psi t_n \sum_{j=1}^{M}(-\hat{\rho}_j^R d_{jn} - \hat{\rho}_j^I c_{jn}) + \sum_{j=1}^{M}\Delta\rho_j^R c_{jn} - \sum_{j=1}^{M}\Delta\rho_j^I d_{jn} \tag{A.11}$$

$$\hat{\hat{S}}_n^I = \hat{S}_n^I - \sum_{j=1}^{M}(\hat{\rho}_j^R d_{jn} - \hat{\rho}_j^I c_{jn}) = 2\pi\Delta\psi t_n \sum_{j=1}^{M}(\hat{\rho}_j^R c_{jn} - \hat{\rho}_j^I d_{jn}) + \sum_{j=1}^{M}\Delta\rho_j^R d_{jn} + \Delta\rho_j^I c_{jn} \tag{A.12}$$

$$\hat{\hat{S}} \approx By \tag{A.13}$$

$$\hat{\hat{S}} = \Big[\hat{\hat{S}}_1^R \quad \hat{\hat{S}}_2^R \quad ... \quad \hat{\hat{S}}_N^R \quad \hat{\hat{S}}_1^I \quad \hat{\hat{S}}_2^I \quad ... \quad \hat{\hat{S}}_N^I\Big]^T \tag{A.14}$$

$$y = \Big[\Delta\psi \quad \Delta\rho_1^R \quad \Delta\rho_1^I \quad \Delta\rho_2^R \quad \Delta\rho_2^I \quad ... \quad \Delta\rho_M^R \quad \Delta\rho_M^I\Big]^T \tag{A.15}$$

$$g_{jn}^R = 2\pi t_n \sum_{j=1}^{M}(-\hat{\rho}_j^R d_{jn} - \hat{\rho}_j^I c_{jn}) \tag{A.16}$$

$$g^I_{jn} = 2\pi t_n \sum_{j=1}^{M} (\hat{\rho}^R_j c_{jn} - \hat{\rho}^I_j d_{jn}) \tag{A.17}$$

$$B = \begin{bmatrix} g^R_{11} & c_{11} & -d_{11} & c_{21} & -d_{21} & \dots & c_{M1} & -d_{M1} \\ g^R_{12} & c_{12} & -d_{12} & c_{22} & -d_{22} & \dots & c_{M2} & -d_{M2} \\ \dots & \dots & \dots & \dots & \dots & \dots & \dots & \dots \\ g^R_{1N} & c_{1N} & -d_{1N} & c_{2N} & -d_{2N} & \dots & c_{MN} & -d_{MN} \\ g^I_{11} & d_{11} & c_{11} & d_{21} & c_{21} & \dots & d_{M1} & c_{M1} \\ g^I_{12} & d_{12} & c_{12} & d_{22} & c_{22} & \dots & d_{M2} & c_{M2} \\ \dots & \dots & \dots & \dots & \dots & \dots & \dots & \dots \\ g^I_{1N} & d_{1N} & c_{1N} & d_{2N} & c_{2N} & \dots & d_{MN} & c_{MN} \end{bmatrix} \tag{A.18}$$

This is the final equation to determine the error terms $\Delta\psi, \Delta\rho^R_j and \Delta\rho^I_j$.

$$y = (B^T B)^{-1} B^T \hat{\hat{S}} \tag{A.19}$$

A.2. MATLAB Code

A.2.1. Main Program

```
%--------------------------------------------------------------------------
%--------------------------------------------------------------------------
% BAT-WAT-Tool
%
% Christoph Birkl, 2011
%--------------------------------------------------------------------------
%--------------------------------------------------------------------------

clear all;
%close all;

clc

t=cputime;

% Auswahl und Konfiguration der Frequenzverschiebung
% ------------------------------------------
%
% deltaF fuer 1,5T
% deltaF = [0,-210];
```

```
%
% deltaF fuer multipoint bei 3T
% deltaF =[0, -431,-329,-483,-245];

reply = input('Load standard deltaF=[0,-431] for 3T or change it: s/c [s]','s')
    ;
if isempty(reply)
    reply = 's';
end
if (reply == 's')

    %standard deltaF des Scanners am LKH Graz
    %frequency offset der kompartements
    deltaF = [0, -431];

    disp(['deltaF = ',num2str(deltaF)])

else

    deltaF(1) = 0;

    numFrequ = input('Enter number of fat frequencys: [1]');
    if isempty(numFrequ)
        numFrequ = 1;
    end

    for dFcount=1:numFrequ

        dF = input('Enter fatpeak frequency:');
        deltaF(dFcount+1) = dF;

    end

    disp(['deltaF = ',num2str(deltaF)])
end


% Load Images
reply = input('Load DICOMs auto/man? a/m [a]: ', 's');
if isempty(reply)
    reply = 'a';
```

```
end
if (reply=='a')

    % Automatisches Einlesen der Dicom-files
    [A,P,GridSpace,TE,mask, numScans, filename_save, dcm_info]=fun_DicomExt();

else

    % Manuelles einlesen der Dicom Bilder (nur ein Slice)
    [A,P,GridSpace,TE,mask, numScans,filename_save,dcm_info]=fun_Dicom_load_man();

end


Amp=double(A);
Pha=double(P);

filename_start = filename_save(1:10);

% Phasenbild normieren -pi..+pi
% ------------------------------------------
Pha=(P-2^11)/2^11*pi;

%get Scan and Image parameters
X = size(Amp,1);
Y = size(Amp,2);
numEchos = size(Amp,3);
numChannels = size(Amp,4);
numSlices = size(Amp,5);

% Test Section TI 400/700 images
%---------------------------------------------------------------------------
% TI (700 und 400) Maskenbilder einlesen
[maskTI700,maskTI400,maskImage] = fun_loadDicomTI(Amp,numSlices);

maskTI400 = double(maskTI400);
maskTI700 = double(maskTI700);

if maskImage == 'j'

```

```
cutoff400 = max(max(maskTI400))*0.9;
cutoff700 = max(max(maskTI700))*0.9;
maskTI400b = abs(maskTI400).*(abs(maskTI400)>cutoff400);
maskTI700b = abs(maskTI700).*(abs(maskTI700)>cutoff700);

end

%-------------------------------------------------------------------------

Rho_res= zeros(2*length(deltaF),X*Y,numChannels,numSlices,'single');
deltaB0_res = zeros(X*Y,numChannels,numSlices,'single');

for lauf_Channels = 1: numChannels
    for lauf_Slices = 1:numSlices

    S = squeeze(Amp(:,:,:,lauf_Channels,lauf_Slices).*exp(1i*Pha(:,:,:,
        lauf_Channels,lauf_Slices)));
    S = S.*repmat(abs(mask(:,:,1))>100,[1,1,numScans]);

    %matrix size

    % X = 50;
    % Y = 50;
    %S=S(end/2-X/2+1:end/2+X/2,end/2-Y/2+1:end/2+Y/2,:);

    S = reshape(S,X*Y,numEchos).';
    S = [real(S);imag(S)] ;

    %deltaB0 = deltaB0(end/2-X/2+1:end/2+X/2,end/2-Y/2+1:end/2+Y/2,:);
    deltaB0 = zeros(X,Y);
    deltaB0 = deltaB0(:);

    A = fun_calcA(deltaF,TE);

    Rho = fun_calcRho(S,A);
    deltaY = zeros(1 + length(deltaF)*2,length(deltaB0));

    S_corr = S;
    maxDeltaB0 = 10;
    iter = 0;
    while (maxDeltaB0 > 1) && (iter < 40)
```

```
        iter = iter+1;

        [S_ccorr,deltaY] = fun_calcDeltaY(S,deltaF,TE,Rho,A,deltaY,iter,S_corr)
            ;
        deltaB0 = deltaB0 + deltaY(1,:).';
        [S_corr,Rho] = fun_calcS_corr(S,TE,deltaB0,A);

        maxDeltaB0 = mean(abs(deltaY(1,:)));
        disp(['iteration: ' num2str(iter) ', maxDeltaB0: ' num2str(maxDeltaB0)
            ]);
    end

            calctime = cputime-t; %Stop time count of algorithm speed
            calctime_min=floor(calctime/60);
            calctime_min_rest=mod(calctime, 60);
            disp(['CH' num2str(lauf_Channels) ':']);
            disp(['Calculation time : ' num2str(calctime_min) 'minutes, '
                num2str(calctime_min_rest) 'seconds.']);
            disp(['Nr. of Iterations: ' num2str(iter) ]);

    deltaB0_res(:,lauf_Channels,lauf_Slices) = deltaB0;
    Rho_res(:,:,lauf_Channels,lauf_Slices) = Rho;
    clear S_ccorr S_corr S P deltaY deltaB0 iter
    end
end
clear lauf_Channels lauf_Slices calctime calctime_min calctime_min_rest
    maxDeltaB0 t


disp('Combine fieldmaps')

S_firstEcho = Amp(:,:,1,:,:);
S_absSq = abs(reshape(S_firstEcho,X*Y,numChannels,numSlices)).^2;
denom = zeros(X*Y,numChannels,numSlices,'single');
for lauf_Channels = 1: numChannels
    denom = denom + deltaB0_res(:,lauf_Channels,:).*S_absSq(:,lauf_Channels,:);
end
deltaB0_combined = denom./sum(S_absSq,2);



%%
```

```
deltaB0 = reshape(deltaB0_combined,X,Y,numSlices);

%-----------------------------------------------------------------------------
%filter Gaussscher TP Filter

G = fspecial('gaussian',[3 3],1);

deltaB0_lp = imfilter(deltaB0,G,'same');

Rho_resFinal = zeros(2*length(deltaF),X*Y,numChannels,numSlices,'single');
Rho_cFinal = zeros(length(deltaF),X*Y,numSlices,'single');
Rho_sumSq = zeros(length(deltaF),X*Y,numSlices,'single');

deltaB0_lp = reshape(deltaB0_lp,X*Y,1,numSlices);

%-----------------------------------------------------------------------------

for lauf_Channels = 1: numChannels
    for lauf_Slices=1:numSlices
        S = squeeze(Amp(:,:,:,lauf_Channels,lauf_Slices).*exp(1i*Pha(:,:,:,
            lauf_Channels,lauf_Slices)));
        S = reshape(S,X*Y,numEchos).';
        S = [real(S);imag(S)] ;
        [S_corr,Rho_resFinal(:,:,lauf_Channels,lauf_Slices)] = fun_calcS_corr(S
            ,TE,deltaB0_lp(:,:,lauf_Slices),A);
        Rho_cFinal(:,:,lauf_Channels,lauf_Slices) = Rho_resFinal(1:2:end,:,
            lauf_Channels,lauf_Slices) + 1i*Rho_resFinal(2:2:end,:,lauf_Channels
            ,lauf_Slices);
    end
    Rho_sumSq = Rho_sumSq + squeeze(abs(Rho_cFinal(:,:,lauf_Channels,:)).^2);
end

Rho_sos = sqrt(Rho_sumSq);
deltaB0_lp = reshape(deltaB0_lp,X,Y, numSlices);

%get the water image
Water=reshape(Rho_sos(1,:),X,Y,numSlices);

%get the fat image
switch(length(deltaF))

```

```
    case 2

    Fat=reshape(Rho_sos(2,:),X,Y,numSlices);

    case 3

    Fat1=reshape(Rho_sos(2,:),X,Y,numSlices);
    Fat2=reshape(Rho_sos(3,:),X,Y,numSlices);

    Fat = abs(Fat1)+abs(Fat2);

    case 4

    Fat1=reshape(Rho_sos(2,:),X,Y,numSlices);
    Fat2=reshape(Rho_sos(3,:),X,Y,numSlices);
    Fat3=reshape(Rho_sos(4,:),X,Y,numSlices);

    Fat = abs(Fat1)+abs(Fat2)+abs(Fat3);

    case 5

    Fat1=reshape(Rho_sos(2,:),X,Y,numSlices);
    Fat2=reshape(Rho_sos(3,:),X,Y,numSlices);
    Fat3=reshape(Rho_sos(4,:),X,Y,numSlices);
    Fat4=reshape(Rho_sos(5,:),X,Y,numSlices);

    Fat = abs(Fat1)+abs(Fat2)+abs(Fat3)+abs(Fat4);

end


%Calculate threshold
%th =th_intermodes(mask)%
th=th_minerror(mask);%%


%calculate the fatfraction and waterfraction
fatfraction = abs(Fat)./(abs(Water)+abs(Fat)).*(abs(mask)>th);
waterfraction = abs(Water)./(abs(Water)+abs(Fat)).*(abs(mask)>th);


```

```
%-------------------------------------------------------------------------
%Starting GUI
disp('Starting GUI ...')
GUI_IDEAL(Water,Fat,deltaB0_lp,mask,Amp,Pha,numSlices,maskImage,maskTI400,
    maskTI700,numEchos,filename_save,dcm_info);
```

MATLAB code of the main file

A.2.2. Function Files

```
function [S,P,GridSpace,TE,mask, numScans,filename_save,dcm_info]=fun_DicomExt
    ()



numScans = input('How many scans (Echos) [3]: ');
if isempty(numScans)
    numScans = 3;
end

reply = input('MultiEcho/SingleEcho scans? m/s [s]: ', 's');
if isempty(reply)
    reply = 's';
end
if (reply=='m')
    isMultiEcho = 1;
else
    isMultiEcho = 0;
end


numSlices = input('How many slices [1]: ');
if isempty(numSlices)
    numSlices = 1;
end

%numChannels = input('How many channels [1]: ');
%if isempty(numChannels)
    numChannels = 1;
%end

[filename,pathname]=uigetfile('*.DCM','Pick first magnitude image');
```

```
info = dicominfo([pathname filename]);

dcm_info = info;

GridSpace=[info.PixelSpacing(2) info.PixelSpacing(1) ];

filename_save = filename;

S = zeros( info.Height,info.Width,numScans, numChannels, numSlices);
P = zeros( info.Height,info.Width,numScans, numChannels, numSlices);
mask = zeros(info.Height,info.Width,numSlices,'single');

%einlesen Betragsbild
%-----------------------------------------
for lauf_ch=1:numChannels
    if lauf_ch > 9
        channel = num2str(lauf_ch);
    else
        channel = ['0' num2str(lauf_ch)];
    end

    for lauf_sl=1:numSlices
        if lauf_sl > 9
            slice = num2str(numSlices);
            slice_nr = num2str(lauf_sl);
        else
            slice = ['0' num2str(numSlices)];
            slice_nr = ['0' num2str(lauf_sl)];
        end

        start_scan = str2double(filename(11:12));
        start_slice = str2double(filename(19:20));



        TE= zeros(1,3);
        disp('files:')
    % load magnitude scans
        for lauf_scan = 1:numScans

            if isMultiEcho
```

```

            path = [pathname filename(1:15) num2str(3) filename(17:23) num2str(lauf_scan) filename((end-11):(end-6)) channel filename(end-3:end) ];
        else
            if numChannels >1
                scan_nr = start_scan + (lauf_scan-1)*4 ;
            else
                scan_nr = start_scan + (lauf_scan-1)*2 ;
            end

            if scan_nr > 9
                scan_nr = num2str(scan_nr);
            else
                scan_nr = ['0' num2str(scan_nr)];
            end
            path = [pathname filename(1:10) num2str(scan_nr) filename(13:15) num2str(3) filename(17:18) slice_nr filename((end-15):(end-6)) channel filename(end-3:end)];
        end

        S(:,:,lauf_scan,lauf_ch,lauf_sl) = dicomread(path);

        if (numChannels>1)
            if ((lauf_ch == 1) && (lauf_scan == 1))
                scan_nr = str2double(scan_nr) +1;
                if scan_nr > 9
                    scan_nr = num2str(scan_nr);
                else
                    scan_nr = ['0' num2str(scan_nr)];
                end
                path = [pathname filename(1:10) num2str(scan_nr) filename(13:15) num2str(3) filename(17:18) slice filename((end-15):(end-6)) channel filename(end-3:end)];
                mask(:,:,lauf_sl) = dicomread(path);
            end
        else
            mask(:,:,lauf_sl) = dicomread(path);
        end
        info = dicominfo(path);
        disp(path);
```

```matlab
            TE(lauf_scan) = info.EchoTime*1e-3;

        end

    % load phase scans
        for lauf_scan = 1:numScans

            if isMultiEcho

                scan_nr = start_scan + 1;
                if scan_nr > 9
                    scan_nr = num2str(scan_nr);
                else
                    scan_nr = [’0’ num2str(scan_nr)];
                end

                path = [pathname filename(1:10) num2str(scan_nr) filename(13:15) num2str(4) filename(17:18) slice_nr filename(21:23) num2str(lauf_scan) filename((end-11):(end-6)) channel filename(end-3:end) ];
            else
                if numChannels >1
                    scan_nr = start_scan + 2 + (lauf_scan-1)*4 ;
                else
                    scan_nr = start_scan + 1 + (lauf_scan-1)*2 ;
                end

                if scan_nr > 9
                    scan_nr = num2str(scan_nr);
                else
                    scan_nr = [’0’ num2str(scan_nr)];
                end
                path = [pathname filename(1:10) num2str(scan_nr) filename(13:15) num2str(4) filename(17:18) slice_nr filename((end-15):(end-6)) channel filename(end-3:end)];
            end
            P(:,:,lauf_scan,lauf_ch,lauf_sl) = dicomread(path);
            disp(path);
        end
    end
end
```

```
disp('succesfully loaded')
```

MATLAB code of the image load routine.

```
function [S_ccorr, deltaY] =fun_calcDeltaY(S,deltaF,TE,Rho,A,deltaY,iter,S_corr)

S_ccorr = zeros(length(TE)*2,size(Rho,2));

for n = 1:length(TE)
    for j = 1:length(deltaF)
       c = cos(2*pi*deltaF(j)*TE(n));
       d = sin(2*pi*deltaF(j)*TE(n));

       S_ccorr(n,:) = S_ccorr(n,:)+ 2*pi*deltaY(1,:).*( -Rho(j*2-1,:)*d - Rho(j*2,:)*c )...
                                 + deltaY(j*2-1,:)*c - deltaY(j*2,:)*d;
       S_ccorr(n+length(TE),:) = S_ccorr(n+length(TE),:)+ 2*pi*deltaY(1,:).*( Rho(j*2-1,:)*c - Rho(j*2,:)*d )...
                                 + deltaY(j*2-1,:)*d + deltaY(j*2,:)*c;

    end
end


g = zeros(length(TE)*2,size(Rho,2));

for n = 1:length(TE)
    for j = 1:length(deltaF)

          c = cos(2*pi*deltaF(j)*TE(n));
          d = sin(2*pi*deltaF(j)*TE(n));

          g(n,:) = g(n,:) + 2*pi*TE(n)*( -Rho(j*2-1,:)*d - Rho(j*2,:)*c );
          g(n+length(TE),:) = g(n+length(TE),:) + 2*pi*TE(n)*( Rho(j*2-1,:)*c - Rho(j*2,:)*d );

    end
end

B = A(:)*ones(1,size(Rho,2));
B = [g; B];
B = reshape(B(:), size(A,1), size(A,2)+1, size(Rho,2));
```

```

if (iter==1)
    S_ccorr=S;
else
    S_ccorr=S_corr;
end


for lauf_pixel = 1:size(Rho,2)


    B_inv = pinv(B(:,:,lauf_pixel));
    deltaY(:,lauf_pixel) = B_inv*S_ccorr(:,lauf_pixel);

end

return
```

Calculate delta y.

```
function Rho=fun_calcRho(S,A)

A_inv = pinv(A);
Rho = A_inv*S;

return
```

Calculate rho function.

```
function [S_corr,Rho]=fun_calcS_corr(S,TE,deltaB0,A)

delta_phi = (deltaB0*TE).';
S=S(1:end/2,:)+1i*S(end/2+1:end,:);
s_corr = S.*exp(-1i*2*pi*(delta_phi));
S_corr = [real(s_corr);imag(s_corr)] ;

Rho = fun_calcRho(S_corr,A);



return
```

Calculate S corr.